NOVEL METHODS IN IMAGE HALFTONING

A THESIS
SUBMITTED TO THE DEPARTMENT OF ELECTRICAL AND
ELECTRONICS ENGINEERING
AND THE INSTITUTE OF ENGINEERING AND SCIENCES
OF BILKENT UNIVERSITY
IN PARTIAL FULFILLMENT OF THE REQUIREMENTS
FOR THE DEGREE OF
MASTER OF SCIENCE

By
Gözde Bozkurt
July 1998

NOVEL METHODS IN IMAGE HALFTONING

A THESIS

SUBMITTED TO THE DEPARTMENT OF ELECTRICAL AND

ELECTRONICS ENGINEERING

AND THE INSTITUTE OF ENGINEERING AND SCIENCES

OF BILKENT UNIVERSITY

IN PARTIAL FULFILLMENT OF THE REQUIREMENTS

FOR THE DEGREE OF

MASTER OF SCIENCE

By

Gözde Bozkurt

July 1998

I certify that I have read this thesis and that in my opinion it is fully adequate, in scope and in quality, as a thesis for the degree of Master of Science.

A. E. Çetin

Prof. Dr. Ahmet Enis Çetin(Supervisor)

I certify that I have read this thesis and that in my opinion it is fully adequate, in scope and in quality, as a thesis for the degree of Master of Science.

O. Arıkan

Assist. Prof. Dr. Orhan Arıkan

I certify that I have read this thesis and that in my opinion it is fully adequate, in scope and in quality, as a thesis for the degree of Master of Science.

B. Barshan

Assoc. Prof. Dr. Billur Barshan

Approved for the Institute of Engineering and Sciences:

Prof. Dr. Mehmet Baray

Director of Institute of Engineering and Sciences

ABSTRACT

NOVEL METHODS IN IMAGE HALFTONING

Gözde Bozkurt
M.S. in Electrical and Electronics Engineering
Supervisor: Prof. Dr. Ahmet Enis Çetin
July 1998

Halftoning refers to the problem of rendering continuous-tone (contone) images on display and printing devices which are capable of reproducing only a limited number of colors. A new adaptive halftoning method using the adaptive QR-RLS algorithm is developed for error diffusion which is one of the halftoning techniques. Also, a diagonal scanning strategy to exploit the human visual system properties in processing the image is proposed. Simulation results on color images demonstrate the superior quality of the new method compared to the existing methods. Another problem studied in this thesis is inverse halftoning which is the problem of recovering a contone image from a given halftoned image. A novel inverse halftoning method is developed for restoring a contone image from the halftoned image. A set theoretic formulation is used where sets are defined using the prior information about the problem. A new space domain projection is introduced assuming the halftoning is performed with error diffusion, and the error diffusion filter kernel is known. The space domain, frequency domain, and space-scale domain projections are used alternately to obtain a feasible solution for the inverse halftoning problem which does not have a unique solution. Simulation results for both grayscale and color images give good results, and demonstrate the effectiveness of the proposed inverse halftoning method.

Keywords: Color image halftoning, error diffusion, adaptive error diffusion, image restoration, inverse halftoning, inverse error diffusion, projection onto convex sets (POCS).

ÖZET

YENİ İMGE YARITONLAMA YÖNTEMLERİ

Gözde Bozkurt
Elektrik ve Elektronik Mühendisliği Bölümü Yüksek Lisans

Tez Yöneticisi: Prof. Dr. Ahmet Enis Çetin
Temmuz 1998

Yarıtonlama, sürekli tonlu imgelerin sınırlı sayıda renk üreten basma ve gösterim cihazlarında üretilmesi problemidir. Bir yarıtonlama tekniği olan hata dağıtılmasında, uyarlanır QR-RLS algoritması kullanılarak yeni bir uyarlanır yarıtonlama yöntemi geliştirilmiştir. Ayrıca, imgeyi işlemede insan görme sistemi özelliklerini kullanan bir köşegen tarama stratejisi önerilmiştir. Renkli resimler üzerindeki benzetim sonuçları, önerilen yöntemin diğer yöntemlere göre yüksek kalitesini göstermiştir. Bu tezde çalışılan diğer bir problem, sürekli tonlu imgenin verilen yarıtonlu imgeden geri elde edilmesi problemi olan ters yarıtonlamadır. Yarıtonlu imgeden sürekli tonlu imge elde etmek için yeni bir ters yarıtonlama yöntemi geliştirilmiştir. Problem hakkında önceden bilinen bilgileri kullanarak tanımlanan kümelerle, küme teorisine dayalı bir formülasyon kullanılmıştır. Yarıtonlamanın hata dağıtılması ile yapıldığı, ve hata dağıtma süzgecinin bilindiği varsayılarak, yeni bir uzay tanım kümesi izdüşümü geliştirilmiştir. Uzay, sıklık, ve uzay-ölçek tanım kümeleri izdüşümleri kullanılarak tek bir çözümü olmayan ters yarıtonlama problemine bir olurlu çözüm elde edilmektedir. Gri ölçekli ve renkli imgelere önerilen yöntemin uygulanması, iyi sonuçlar vermiş, ve geçerliliğini göstermiştir.

Anahtar Kelimeler: Renkli imge yarıtonlama, hata dağıtma, uyarlanır hata dağıtma, imge geri getirme, ters yarıtonlama, ters hata dağıtma, dış bükey kümelere izdüşüm.

ACKNOWLEDGEMENT

I gratefully thank my supervisor Prof. Dr. Enis Çetin for his supervision, guidance, and suggestions throughout the development of this thesis.

I would like to thank Assist. Prof. Dr. Orhan Arıkan for his suggestions, encouragement, and valuable discussions, and Assoc. Prof. Dr. Billur Barshan, the members of my jury, for reading and commenting on the thesis.

It is a pleasure to express my special thanks to my mother, and father for their sincere love, support and encouragement.

Many thanks to all of my close friends for their help and friendship.

Contents

List of Figures

List of Tables

To my parents, and Alper . . .

Chapter 1

INTRODUCTION

Halftoning refers to the problem of rendering continuous-tone (contone) images on display and printing devices which are capable of reproducing only a limited number of colors. This reduction in the number of colors causes a highly visible degradation in the quality of the image that naturally contains thousands or millions of colors. As a common solution to this problem, halftoning techniques are used.

In this thesis, a new adaptive signal processing algorithm is employed in the method of error diffusion which is a widely used halftoning technique. Various space filling curves to define the order of processing in error diffusion exist in literature. In this thesis, a diagonal space filling curve to exploit the human visual system properties in processing the image is proposed. Simulation results on color images are presented to demonstrate the superior quality of the proposed method compared to the other methods.

Inverse halftoning is the problem of recovering a contone image from a given halftoned image. In this area, less research has been performed than halftoning. In this thesis, a novel inverse halftoning method is proposed to restore a contone image close to the original contone image. A set theoretic formulation is used where three sets are defined using the prior information about the problem. A new space domain projection is introduced assuming the halftoning is performed with error diffusion, and the error diffusion filter kernel is known. The space domain, frequency domain, and space-scale domain projections are used alternately to obtain a feasible solution for the inverse halftoning problem which does not have a unique solution. Simulation results for both grayscale and color images are presented.

In this Chapter, a survey on halftoning and inverse halftoning literature is given. Finally, the contribution and scope of this thesis is presented.

1.1 Motivation

Increasing demand for digital display of images on any of a wide variety of devices, and the increasing use of halftone printers to make hard copy outputs are given as the motivation for the research that resulted in part of this thesis.

In most computer color displays, the images are stored in a video memory. There, usually they are first recorded as full color images, where each color pixel is represented by 8 or 12 bits for each of the three channels. However, supporting storage of these full color images requires a high cost for high speed video memory. Many color display devices therefore reduce memory requirements by allocating 8,12, or 16 bits of video memory for each color pixel, thus allowing $2^8, 2^{12}$, or 2^{16} number of colors to be displayed simultaneously. Then, a palletized image which contains only colors from a limited palette, is stored in video memory and rapidly displayed using look-up tables [1]. However, direct quantization from a very large set of colors to a very limited set of colors produces contouring effects in the output image. To prevent this problem, halftoning methods are used.

Printing devices are classified as contone and halftone printers [1]. Photography is the best known process that produces contone images. Using photochemical methods which mimic photography, contone printing can be realized [1]. However, since they are rather expensive, most printers used are based on the halftoning technique. The reproduction of images in all newspapers, magazines, books, other mass printed media are printed with digital halftoning technologies. This technology creates an extremely large number of pictorial images daily [2].

Color output devices such as halftone color printers and palette-based displays are capable of producing only a limited number of colors, whereas the human eye can distinguish around ten million colors under optimal viewing conditions [1]. Therefore, today, digital halftoning plays a key role in almost every discipline that involves printing and displaying.

Halftoning has enormous practical value, and a considerable amount of research has been performed in this area. The inverse problem of reconstructing a contone image from its halftone version has also a large number of applications but much less research has been performed. This fact is the motivation for the research that resulted in the second part of this thesis. Contone images are needed instead of halftone in order to perform typical image processing tasks such as scaling, enhancement, tone correction, sharpening, decimation, interpolation, extrapolation, rehalftoning, compression, edge detection, recognition, linear or nonlinear filtering.

1.2 Halftoning

The eye perceives only a local spatial average of the color spots produced by a printing device, and is relatively insensitive to errors made in high frequencies in an image [1]. Halftoning algorithms, therefore aim to preserve these local averages while forcing the errors between the contone image and the halftone image to high frequency regions. The existing halftoning techniques can be broadly classified as dithering techniques, error diffusion techniques, optimization-based halftoning techniques and hybrid techniques. An overview of literature in each of these classes is given next.

1.2.1 Dithering Techniques

Random dither, or white noise dithering is historically the first attempt to reduce the visible artifacts of direct quantization. The basic idea in dithering methods is thresholding each pixel value after adding noise to each pixel. It is also known as Roberts' pseudo-noise technique, and it works by adding white noise to each pixel before quantization [3]. Roberts pointed out that dither does not increase the noise energy but simply redistributes the quantization noise to make it less visible. In frequency domain, the error in coarse quantizing a contone level is low in frequency and highly visible, whereas halftoning produces errors that are higher in frequency and therefore less visible.

The second class of dithering techniques employ dither matrices that quantize the image by pixelwise thresholding. In conventional digital color halftoning for printers, the image is decomposed into cyan, magenta, yellow, and black separations which are halftoned independently [1]. Black colorant is introduced to produce denser blacks, reduce ink usage, and to conserve more expensive colorants. The halftoning for each separation is done by comparing each pixel value with a deterministic, spatially periodic dither array. Pixels for which the image exceeds the value in the corresponding dither matrix are turned on. Overlaying screens of color components with the same orientation causes the problem of registration. Some variation in the alignment of these color screens caused by the mechanical systems used in movement of the reproduction medium produces an artifact called moire patterns [1]. The effect is manifested as color shifts. Therefore, rotated screens are used where the rotation angle is chosen so as to minimize the occurrence and visibility of low frequency interference moire patterns. The most visible black screen is oriented along a 45° angle, along which the eye is least sensitive. The yellow, magenta, and cyan screens are located along $0°, 15°$, and $75°$, respectively [4].

Ordered dither algorithms are generally classified as two types: clustered-dot dither, and dispersed dot dither [5]. In clustered dot dither, the lower threshold values are centered in the pattern, causing a central dot that increases in size as the pixel value increases. In the dither matrix, the thresholds that are close in value are near each other so that for a uniform image, the halftoning scheme generates a grid of halftone dots consisting of clusters of on pixels. As the image value increases, the size of the clustered dots increases. In dispersed dot dither, the lower threshold values are scattered throughout the pattern, causing small dispersed dots that increase in number as the signal value increases [6].

Clustered dot patterns are insensitive to most printing distortions such as dot overlap, ink spreading, and reproduce well on printers that are incapable of reproducing isolated pixels. Therefore rotated clustered dot dithering is widely used for color printing. However, when the image is to be produced on a device that can successfully display every isolated pixel, the preferred choice is dispersed dot dither halftoning which maximizes the use of resolution [5]. For displays, alternate dither matrices that produce dispersed dots with greater spatial resolution are applied.

The ordered dithering techniques are attractive in the sense that they are very simple to implement, and computationally inexpensive because they require pixelwise operations. However, the major disadvantage of dithering is that it gives rise to regular error patterns due to the regular pattern of the noise introduced at different pixel locations.

1.2.2 Error Diffusion Techniques

The problems of moire patterns and color shifts created by misregistration of color screens in ordered dither is relatively eliminated by the error diffusion algorithm, that is first introduced by Floyd and Steinberg [7], which requires neighborhood operations. They proposed an algorithm which works by distributing the quantization error of the current pixel to neighboring pixels. Typically, at each pixel, the weighted sum of previous quantization errors is added to the current pixel, and the corrected sum is quantized to produce the output pixel. These weights form an error diffusion filter. The error diffusion aims to preserve the local average value of the image, therefore a unity gain lowpass finite impulse response (FIR) filter is used for distributing the error.

Error diffusion was first developed for grayscale images. For color images, error diffusion can be applied to each color component independently, which is called scalar error diffusion, or as in [8], a color pixel can be error diffused in a vectorized manner.

Error diffusion works by shaping the error spectrum. In this method, the error is concentrated in high frequencies. This is suitable to the human eye which is less sensitive to high frequencies. Ulichney [5] proposed an error diffusion filter with randomized weighting coefficients to shape the display error spectrum to have mostly high frequency content, named as Blue Noise. He examined the spectral characteristics of the output error, and demonstrated that blue noise is less noticeable to the human eye than errors compared to the white power spectrum.

Error diffusion technique is still an active area of research. Variations on this technique are employed by many researchers.

Some directional artifacts seen in error diffusion are due largely to the traditional raster of processing [5]. Previous approaches for improving error diffusion employed various choices of space filling curves to define the order of processing, such as serpentine curves [5], Peano curves [9], random space filling curves [10]. In [10], purpose of randomness is to erase regular patterns arising usually in uniform intensity image regions. A disadvantage of this method is large memory consumption which is overcome by performing the halftoning for blocks of the image separately. Witten and Neal [9] used an error filter with one deterministic weight, and processed the image on a Peano curve.

In [11], error diffusion is modified by incorporating a color printer model that accounts for dot overlap distortion in printers. A human visual system model in the form of its Modulation Transfer Function (MTF) is incorporated into error diffusion in [12].

In contrast to deterministic error filter kernels, some recent research employed dynamically adjusting the error filter kernel using adaptive signal processing techniques. Akarun, Yardımcı, and Çetin [8] have used a vectorized error diffusion approach, and updated the error diffusion filter coefficients adaptively. Wong [13] minimizes a local frequency-weighted error criterion to adjust the error diffusion kernel dynamically using the well known least-mean-square(LMS) algorithm [14]. He also proposed an embedded multilevel error diffusion algorithm to enable rendition at several resolutions which can be useful for progressive transmission.

Sequential nature of the error diffusion technique means that the errors get propagated in the direction the image is scanned, which can result in subtle artifacts. An algorithm in which the errors are diffused isotropically in all directions would be preferred.

For single pass processing of the image, error diffusion filter kernel is causal which implies that the filter is asymmetric. This asymmetry causes visible low frequency wormlike artifacts in binary error diffusion. Symmetric error diffusion neural networks have been proposed for gray scale images [15]. An all optical implementation of the symmetric error diffusion algorithm is given in [16]. One of the advantages of this implementation is its reduced computational complexity, and storage requirements, and high speed.

To allow usage of a non-causal error filter, a multi-pass error diffusion is proposed in [17], where the quantization error of one iteration(pass) is collected and used during the next iteration as quantization error of the future pixels. The error filter in this case is preferably chosen as a zero-phase filter so that feedback is added to the input image without affecting the phase to retain sharp edges. The disadvantage of this algorithm is its iterative nature.

Kolpatzik and Bouman [18] developed an optimization criterion for the design of an error diffusion filter, based on a model for the human visual system to include the effects of the monitor modulation function and human visual modulation transfer function combining the models in [6]. They also developed a locally dithered error diffusion algorithm combining the idea in random dither and error diffusion.

A fuzzy error diffusion method for color images is presented in [19] which makes use of membership functions indicating the location of a pixel with respect to each quantization color. This information is used to control the amount of error to be spread thus preventing the accumulation of errors.

Another modification to error diffusion of grayscale images proposed in [20] is introducing an input dependent threshold into the process to decrease or increase edge enhancement in the algorithm.

Most of the error diffusion methods existing in the literature are developed for halftoning of grayscale images. Only a few of the methods mentioned are proposed for color images where most are not efficient in producing a high quality color image output. Another disadvantage of these color error diffusion methods is their substantially high computational complexity.

1.2.3 Optimization-based Halftoning Techniques

The problem of halftoning can be formulated as an optimization problem that minimizes an error metric between the continuous tone original image and its halftone version. These techniques can be referred as optimization-based halftoning techniques which are iterative, and requires significantly more computation than error diffusion based techniques, and ordered dither techniques. In this approach, the halftoning problem is posed as an optimization problem which maximizes the visual similarity between the original image and its halftone version.

In these methods, a distortion measure is defined, and some methods employ visual models or printer models in the definition of these measures. Therefore, they are also referred as model-based halftoning techniques. Pappas [21] included both a printer model and a visual model. The simple eye model in [22] includes a memoryless nonlinearity followed by a filter which is chosen as the MTF referring to the spatial frequency sensitivity of the eye [23]. An optimal halftone image is found by minimizing the squared error between the output of the cascade of the printer and visual models in response to the halftone image and the output of the visual models in response to the original contone image. Two dimensional least-squares solution is obtained by iterative optimization techniques. A distortion measure in the frequency-domain, frequency weighted mean-squared-error criterion between the continuous-amplitude input image and discrete-amplitude version, is proposed, and an equivalent approach based on neural networks is suggested in [15]. Both a space-domain distortion measure and a frequency-domain distortion measure are proposed in [24], where the minimization procedure is performed blockwise in the image. In frequency-domain optimization, the weighting function is the MTF proposed in [23].

Similarly, an error metric related to the total generated error between the contone and halftone images is defined in [25]. The total error is filtered with contrast sensitivity function describing the visibility of signals as a function of the spatial frequency because the errors which are not visible are of no interest. A descent-type algorithm, and a simulated annealing algorithm are used for the optimization problem in [25]. Usage of genetic algorithms is proposed in [26] for optimization-based halftoning in a similar way.

Disadvantages of optimization-based methods for halftoning is that there are many local optima, the methods are iterative, and they require substantially high computational power. For color images, processing requirements further increase.

1.2.4 Hybrid Schemes

Hybrid schemes that combine different aspects of halftoning methods are proposed in the literature.

Blue noise halftoning that combines the speed of dithering techniques with the quality of error diffusion techniques is the application of large dither matrices produced for obtaining blue noise characteristics [27]. For color images, independent blue noise masks are used for each color component.

A number of researchers considered the problem of selecting an optimal color palette and the optimal mapping of each pixel of the image to a color from the palette in a unified manner. Orchard and Bouman [28] proposed a new error diffusion algorithm using an image specific color palette having a binary tree structure for efficient implementation. Similarly, in [29, 30], dithering process is embedded in the quantization process. In [29], the cluster splitting strategy of [28] is modified at the leaves so that a pair of leaves after the split are displaced in opposite directions to span a wider color space. In [30], palette colors in color space and color pixels in the color image are alternately updated. At each pixel, the palette color to which the pixel belongs is updated according to the competitive learning rule. Afterwards, error diffusion step is performed.

Halftoning algorithms based on multiresolution, pyramidal structure, for grayscale halftoning are proposed in [31, 32]. In [31], at each pyramid level, the output binarized image is compared with the original grayscale image over a successively larger window of pixels, and some binary pixels are modified in order to reduce a weighted averaged error. Similarly, a multiscale error diffusion is proposed in [32] where the algorithm begins with the lowest resolution image at the top of the image pyramid, and proceeds by always selecting the quadrant with the highest average intensity.

1.3 Inverse Halftoning

Inverse halftoning is the problem of recovering a contone image from a given halftone image. This inverse problem can be thought as a restoration problem or a denoising problem since halftoning can be considered as a process that degrades the original image by introducing noise into it. Halftoning is a many-to-one mapping, therefore inverse halftoning problem does not a have a unique solution. Research in this area is considerably less than that is done for forward halftoning.

The existing inverse halftoning methods employ space-domain operations, frequency-domain operations, or both, or only space-scale domain operations. Literature on inverse halftoning contains research only for recovering a gray-scale image from its binary halftone version. We give an overview of these methods next.

The simplest approach is lowpass filtering the halftone image to remove the high-frequency components. Since in error-diffused images, the errors are generally concentrated in the high frequencies, this approach seems reasonable. Different lowpass filters have been used such as halfband lowpass in [33], Gaussian lowpass and lowpass filtering based on singular value decomposition (SVD) [36]. However, lowpass filtering alone does not work well since this also destroys high-frequency information of the original image. This approach corresponds to ignoring the spatial constraints, and enforcing only frequency constraints.

A projection algorithm, which is essentially an error diffusion with an additional inverse quantization step is proposed in [33]. Error diffusion is performed at each pixel starting with an approximation of the contone image, e.g., lowpass filtered version of the halftone image. The input pixel is adjusted so that the corrected pixel value at the input of the quantizer is quantized to the desired halftone value at the output. This projection in inverse quantization process is performed by maximum a posteriori probability (MAP) projection. A similar method [34], based on a MAP estimator is proposed where a constrained optimization is solved using iterative techniques.

The method of Projection Onto Convex Sets (POCS) is used in [35, 36] where information known about the problem is expressed in the form of two constraint sets. Space-domain projection using the first constraint set, then frequency-domain projection using the second constraint set, are performed alternately, to find an image invariant under both. The first set is the set of all contone images which when halftoned give the desired halftone image, the second is the set of all images bandlimited to a certain band. The method in [35] is designed for recovering a contone image from an image halftoned with ordered dithering method. The frequency-domain projection is performed with lowpass filtering, and the space-domain projection is performed with making the minimum change necessary to each image pixel after comparison with the screen function.

Another method using the idea of POCS to reconstruct images from a $\sum\Delta$-based error diffused image, is proposed in [36]. A linear SVD based transform or a linear Gaussian filtering are used for frequency-domain projection. For the space-domain projection, they define a computational procedure for error diffusion by slightly modifying the error diffusion to reduce the complexity of their reconstruction algorithm. Using this, they propose a matrix space-domain description of the error diffusion encoder. However, the computational cost of the projection is very high because the algorithm turns out to be a linearly constrained Quadratic Programming (QP) problem that tries to solve 512×512 matrix equations for an image of this size. They suggested solving this problem by solving a number of QP subproblems of size L_{QP}, i.e., size of the blocks, rather than solving one QP problem of size N^2.

In these techniques, the halftoning process is assumed to be known a priori. In case of ordered dither halftone images, an algorithm to estimate the screen function is proposed in [35]. Similarly, for error-diffused images, Wong [33] suggested a method to estimate the error diffusion kernel posing the problem as a system identification problem encountered in adaptive signal processing.

Xiong, Orchard, and Ramchandran [37] proposed an inverse halftoning scheme using wavelets. The idea behind the wavelet decomposition of a halftone image is to selectively choose useful information from each subband. This approach can be considered as a space-scale domain method. An explicit edge detection based on cross-scale correlation of the highpass wavelet images is done to perform spatially varying filtering of the halftone image. In this way, background halftoning noise is removed while important edge information is preserved in the bandpass bands. Furthermore, no a priori knowledge about the halftoning process is assumed.

Another wavelet-based inverse halftoning method is proposed in [38], where after subband decomposition of the halftone image, halftone noise in the subbands is eliminated by spatial and frequency selective processing. Frequency selective processing corresponds to interband operations, and comparison of the magnitudes of the coefficients at different resolution levels but the same spatial location, then clipping some coefficient values accordingly. Spatial processing corresponds to intraband filtering, i.e., oriented filtering tailored for each subband to preserve edges along its orientation.

In [39], a simple table-lookup method referred as a nonlinear decoder to convert error-diffused images back to the grayscale domain is implemented. Blocks of size 3×3 are used as an index into a table consisting of 512 distinct binary patterns. This look-up table is built by calculating an output gray value for each index (3×3) in the training sequence. Then each halftoned pixel is decoded based on its 3×3 neighborhood which gives the grayscale output from the table. This method is simple, however it needs a training phase to obtain the look-up table. Furthermore, the reconstructed image quality is relatively lower.

1.4 Contribution and Scope

The first contribution of the thesis is the introduction of a new adaptive error diffusion method for color images. A rotation based Recursive Least Squares algorithm is used in the prediction where the error diffusion filter coefficients are updated adaptively. Both scalar and vector implementations of the proposed method is developed. The scalar implementation processes each color component of the color image separately whereas the vector implementation uses all three color components in the prediction of each color component. Also a diagonal scan is used in processing the image to exploit the relative insensitivity of the human visual system to diagonal orientations. The proposed method produces high quality halftone images with a very limited number of colors.

The second contribution of the thesis is the introduction of a set theoretic inverse halftoning method which restores the continuous tone image back from its halftone version. A new space-domain projection is proposed which defines a set for each pixel, and the projection is performed at each pixel using the a priori information that the halftoning is performed with the error diffusion method, and the error diffusion filter kernel is known. In addition, frequency and space-scale domain projections are used alternately with the proposed space-domain projection to find a feasible solution for the inverse halftoning problem that has no unique solution. Furthermore, the space-domain projection is extended for the case of multilevel error diffusion encoding. This extension is in turn used for restoration of color images from their halftoned versions. The proposed inverse halftoning for color images may be viewed as a first attempt in this area.

Chapter 2 introduces the new adaptive error diffusion method that results into higher quality output images than that of Floyd-Steinberg's method and the error diffusion with Least Mean Square adaptation. Extensive simulation results are given to show the performance of the proposed method.

Chapter 3 introduces the proposed inverse halftoning method with a new space-domain projection. The simulation results of the proposed method is compared with those of the state-of-the-art inverse halftoning methods existing in the literature, based on their Peak Signal-to-Noise-Ratio's.

Chapter 4 gives the conclusions and future work.

Chapter 2

AN ADAPTIVE ERROR DIFFUSION METHOD

In this chapter, a new error diffusion method is presented in which the adaptive Recursive Least Squares (RLS) algorithm is used for prediction. Also, a diagonal scan is used in processing the image to take advantage of the human visual system. The simulation results of the proposed method is compared with that of the Floyd-Steinberg's method, and the adaptive error diffusion with LMS algorithm both with raster scan and diagonal scan of the image. The simulation studies show the superiority of the proposed adaptive error diffusion method.

2.1 Diagonal Error Diffusion

Block diagram of the standard error diffusion technique is given in Figure 2.1. Usually, the image is processed in a raster scan fashion, and each input color pixel $\boldsymbol{x}(s_1, s_2)$ is a 3×1 vector, where the index (s_1, s_2) denotes the pixel location in the image. Let us first introduce new notation to simplify the discussion. In the usual raster scan, the index s is given by $s = s_1 M + s_2$, where M is the number of horizontal pixels in the image. The current pixel $\boldsymbol{x}(s)$ together with the diffused error is quantized. The resultant image $\boldsymbol{y}(s)$ is the dithered image.

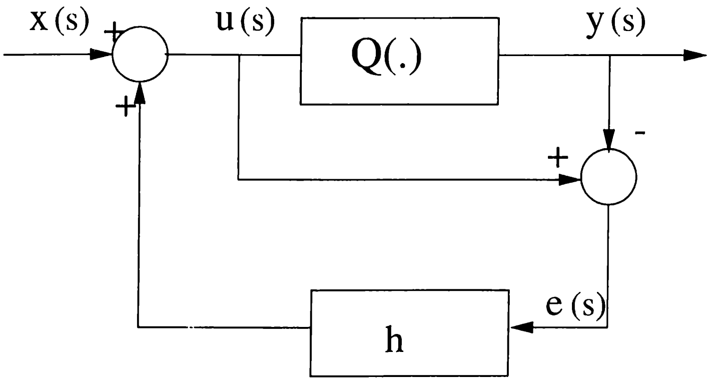

Figure 2.1: Block diagram of error diffusion method.

Here, $\boldsymbol{Q}$ is the quantizer, and $\boldsymbol{h}$ is the error diffusion filter. Some well-known error diffusion filter masks [7,40] are shown in Figure 2.2 where • denotes the origin. These masks determine the support of the error diffusion filter. A common characteristic of these filters is that they are causal, i.e. their region of support is wedge-like to ensure that these filters can be applied in a sequential manner [41]. The filter coefficients are deterministic, lowpass in nature, and add up to 1 so that errors are neither amplified nor reduced.

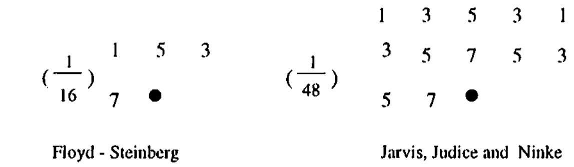

Figure 2.2: Error Diffusion Filter Masks: (a) Floyd-Steinberg, (b) Jarvis, Judice and Ninke.

A weighted sum of the previous quantization errors in the window, and the current pixel $\boldsymbol{x}(s)$ are added to form $\boldsymbol{u}(s)$, and this value is quantized to obtain the dithered pixel value as follows:

$$\boldsymbol{u}(s) = \boldsymbol{x}(s) + \sum_{k<s} \boldsymbol{h}(s-k)\boldsymbol{e}(k) \tag{2.1}$$

$$\boldsymbol{e}(s) = \boldsymbol{u}(s) - \boldsymbol{y}(s) \tag{2.2}$$

$$\boldsymbol{y}(s) = Q(\boldsymbol{u}(s)) \tag{2.3}$$

where $k < s$ corresponds to a causal error diffusion mask, and $\boldsymbol{e}(s)$ is the quantization error. The error between the original input pixel and the output pixel is defined as the output error, $\boldsymbol{e}_{out}(s) = \boldsymbol{x}(s) - \boldsymbol{y}(s)$ which can be expressed as

$$\boldsymbol{e}_{out}(s) = \boldsymbol{e}(s) - \sum_{k<s} \boldsymbol{h}(s-k)\boldsymbol{e}(k) \tag{2.4}$$

Let the 2-D Discrete-Time Fourier Transform of $\boldsymbol{e}_{out}(s)$ to be

$$\boldsymbol{E}_{out}(w) = \sum_{s \in Z^2} \boldsymbol{e}_{out}(s) e^{-js\ w^T} \tag{2.5}$$

where w is the 1-D index for $\boldsymbol{w} = (w_1, w_2)$ for simplicity, and Z is the set of all integers. From (2.4), the output error spectrum becomes

$$\boldsymbol{E}_{out}(w) = \boldsymbol{E}(w)[\boldsymbol{I} - \boldsymbol{H}(w)] \tag{2.6}$$

where $\boldsymbol{H}(w)$ is the frequency response of the error diffusion filter. If the quantization error spectrum is white, the output error spectrum can be shaped by the $(\boldsymbol{I} - \boldsymbol{H}(w))$ filter. Since $\boldsymbol{H}(w)$ is lowpass, $(\boldsymbol{I} - \boldsymbol{H}(w))$ is a highpass filter. This is a favorable feature of the error diffusion algorithm because the human visual system is less sensitive to high frequency components in an image. Furthermore, the error diffusion filter coefficients sum to 1, i.e., $\boldsymbol{H}(0) = 1$. This leads to $\boldsymbol{E}_{out}(0) = 0$, and implies that the mean value of the quantized image is matched to the original image mean.

The raster scan used in error diffusion causes vertical or horizontal artifacts, and regular patterns that arise especially in uniform intensity regions. It is well-known that human visual system is less sensitive to diagonal errors compared to the vertical or horizontal errors. To take advantage of this fact we scanned the image diagonally. In this way, the error is diagonally diffused, and the resulting artifacts are less bothersome. Causal prediction windows shown in Figure 2.3 are used in the error diffusion algorithm. Here, we aim to break up the horizontal and vertical directionality of the possible error patterns, and force the accumulation of the error to be in diagonal orientation to which the human eye is less sensitive.

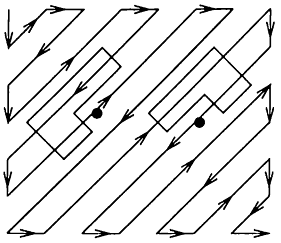

Figure 2.3: Diagonal Scanning: dots correspond to the current pixel, and the L-shaped window contains the previous pixels.

2.2 A New Adaptive Error Diffusion

The error diffusion filter plays an important role in shaping the output error spectrum. The error filter should be designed so that the output error, $\boldsymbol{e}_{out}(s)$, is the least noticeable to a human observer [18]. In contrast to deterministic error diffusion filters, recent algorithms use the optimum filter coefficients for a given image, or update the coefficients adaptively using Least Mean Square (LMS) type adaptive algorithms [8,13].

As in standard dithering, in error diffusion, the aim is decorrelate the quantization noise, the difference between the input and output of the quantizer, from the input signal. This results into a whiter error spectrum, so the errors are less visible and less disturbing for the observers. This requires the prediction of the quantization error of the current pixel from the previous quantization errors. The prediction aims to minimize the energy of the output error $\boldsymbol{e}_{out}(s)$, as shown in Figure 2.4, as follows:

$$E[||\boldsymbol{e}_{out}(s)||^2] = E[||\boldsymbol{x}(s) - \boldsymbol{y}(s)||^2]. \tag{2.7}$$

This is equivalent to minimizing

$$E[||\boldsymbol{e}(s) - \sum_{k<s} \boldsymbol{h}(s-k)\boldsymbol{e}(k)||^2]. \tag{2.8}$$

Then the optimal filter coefficients are chosen as the minimizer of (2.8). Differentiating (2.8) with respect to $\boldsymbol{h}(i)$, and setting the results to zero, the following set of linear equations are obtained:

$$E[\boldsymbol{e}(s)\boldsymbol{e}^T(s-i)] = \sum_{k<s} \boldsymbol{h}(s-k)E[\boldsymbol{e}(s)\boldsymbol{e}^T(s-i)], \qquad i < s \tag{2.9}$$

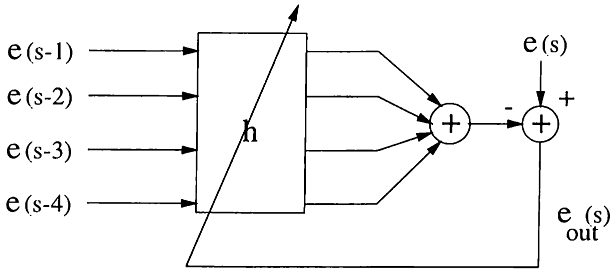

Figure 2.4: Prediction of the quantization error.

The error diffusion coefficients $\boldsymbol{h}$ can be obtained by solving the system of equations in (2.9). An estimate of the covariance matrix $E[\boldsymbol{e}\,(s)\boldsymbol{e}^T(s-i)]$ can be obtained from the quantization error statistics of the image. However, since a typical image does not have stationary characteristics, this approach does not yield satisfactory results.

Considering the fact that the image signal characteristics are generally non-stationary, that is significant difference exists in the statistics of different regions of the image, an adaptive algorithm is used in the minimization of the output error sequence. In this thesis, in order to achieve better prediction than the LMS algorithm which was used in some earlier work, we considered using an RLS-type adaptive algorithm. The LMS provides an approximate solution to the Least Squares(LS) problem that arise in many applications of signal processing. Two different classes of methods have been developed for solving these problems: the LMS is based on the gradient descent technique, and the RLS algorithm uses exponentially weighted LS criterion.

The RLS algorithm provides an exact solution of the LS problem at each time step. There are various RLS algorithms, where most widely used are the Fast RLS algorithms such as Fast Transversal filters(FTF) [42]. These RLS algorithms were preferred because they provide optimal weights at every sample, are faster than LMS-based techniques in convergence, and can be numerically more stable. However in the fast RLS algorithm, the input data vector is updated by a shift at each time step, and in the case of error diffusion, the L-shaped window contains the pixels used in the prediction where the data vector is altered by a 2-D shift. Therefore, fast RLS algorithms are not exactly suitable for a linear combiner implementation which is the prediction problem of the current quantization error. Recently, LS problems are solved using rotation-based methods, based on updating the QR-decomposition of the input data matrix. These rotation-based algorithms are more robust to low precision arithmetic that reduce the implementation costs whereas non-rotation-based RLS algorithms may break down [43]. QR algorithms offer fast convergence behavior and better tracking ability. The QR-linear combiner is well suited for the prediction problem in error diffusion. The complexity of the QR-RLS adaptation is Order(N^2), where LMS adaptation has a complexity of Order(N). N is the number of pixels in the prediction window, which is chosen as $N = 4$ as in Floyd-Steinberg's method. Therefore, the complexity of the QR-RLS algorithm does not increase much.

The basic linear LS estimator is the linear combiner. The problem of prediction of the quantization error in error diffusion can be implemented as QR-linear combiner. Using a linear combination of the previous quantization error signals, we want to estimate the desired signal $\boldsymbol{e}(s)$. The previous quantization errors $\boldsymbol{e}(s-i)$ are represented as $\boldsymbol{e}_i(s)$. The estimate is $\boldsymbol{e}(s) = \boldsymbol{h}^T(s)\boldsymbol{e}_p(s)$, where $\boldsymbol{e}_p(s) = [\boldsymbol{e}_1(s), ..., \boldsymbol{e}_N(s)]^T$ denotes the $N \times 1$ data vector and $\boldsymbol{h}(s)$ denotes the weight vector. The purpose of recursive LS estimation is to choose $\boldsymbol{h}(s)$ so as to minimize the sum of exponentially weighted squared errors,

$$\sum_{m=1}^{s} \lambda^{s-m}[\boldsymbol{e}(m) - \boldsymbol{h}^T(s)\boldsymbol{e}_p(m)]^2 \tag{2.10}$$

The factor $0 \ll \lambda \leq 1$ is called the forgetting factor. Its aim is to forget the data in the distant past to have a better tracking capability in a nonstationary environment.

The summary of the QR-RLS algorithm is given as follows:

$$\boldsymbol{R}(0) = \sqrt{\delta}\boldsymbol{I}_N, \boldsymbol{\Gamma}(0) = \boldsymbol{0}$$

$$\text{for} \quad s = 1, 2, \ldots$$

$$\boldsymbol{Q}(s) \begin{bmatrix} \sqrt{\lambda}\boldsymbol{R}(s-1) & \sqrt{\lambda}\boldsymbol{\Gamma}(s-1) & \boldsymbol{R}^{-T}(s-1)/\sqrt{\lambda} \\ \boldsymbol{e}_p^T(s) & \boldsymbol{e}(s) & \boldsymbol{0}^T \end{bmatrix} = \begin{bmatrix} \boldsymbol{R}(s) & \boldsymbol{\Gamma}(s) & \boldsymbol{R}^{-T}(s) \\ \boldsymbol{0}^T(s) & \tilde{f}(s) & \tilde{\boldsymbol{g}}^T(s) \end{bmatrix}$$

$$\begin{aligned} \tilde{\gamma}(s) &= \prod_{i=1}^{N} \cos\theta_i(s) \\ f(s) &= \tilde{f}(s)\tilde{\gamma}(s) \end{aligned}$$

$$h(s) = h(s-1) - \tilde{g}(s)\tilde{f}(s)$$

A detailed discussion of the QR-RLS algorithm can be found in [43].

In the implementation of the QR-Linear combiner, the previous quantization errors in the causal so-called half plane window are used as inputs, and the current quantization error is used as the desired signal. In the scalar implementation of the algorithm, the red, green and blue components of each pixel are processed separately by running three QR-RLS algorithms in parallel, each giving the output for each one of the color components red, green, blue, as shown in Figure 2.5. The number of pixels in the prediction window of each color component is chosen as $N = 4$ in our implementations.

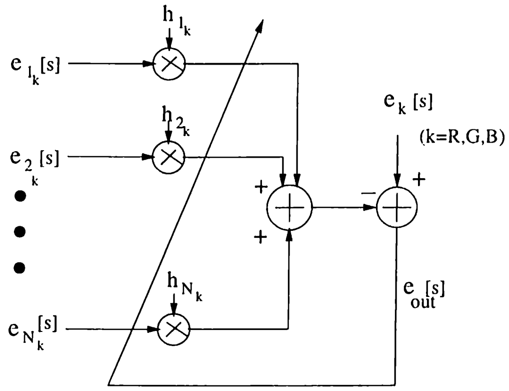

Figure 2.5: QR Linear Combiner, Scalar Implementation.

In the vector implementation, all three color components of the previous quantization errors are used in the prediction of the each component of the current quantization error, as in Figure 2.6. Again, three parallel QR-RLS algorithms are run for each of the color components. Here, the aim is to use the correlation among the color components. The number of pixels in the prediction window, is chosen as $N = 12$ in the vector implementation for each color component.

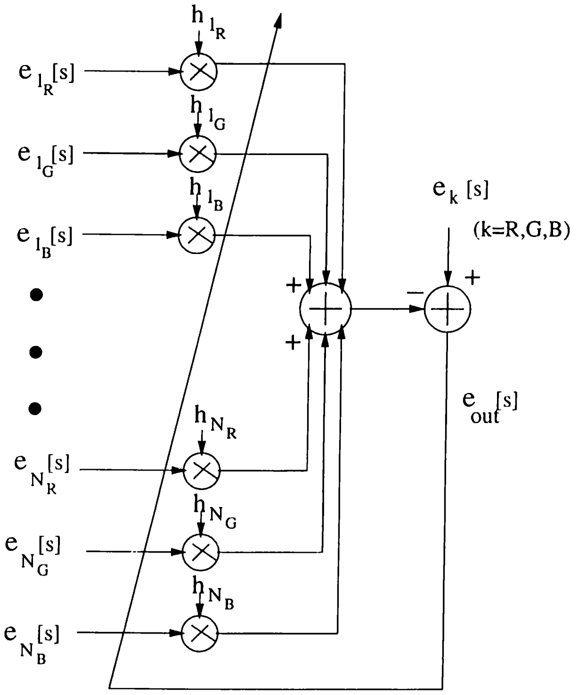

Figure 2.6: QR Linear Combiner, Vector Implementation.

2.3 Simulation Results

In this section, we demonstrate the effectiveness of our error diffusion algorithm using three specially selected color images. To render the illusion of a color ramp, two photographs Sunset image, and Minnesota image are used. These images are good test images with slowly varying color regions. Third test image is the well-known Peppers image, which has both slowly varying regions, and sharp edges.

We implemented both the scalar and vector versions of the RLS-based adaptive error diffusion algorithm. We give the results of the scalar implementation. The results of the new algorithm is compared with that of the Floyd-Steinberg's method, and the adaptive error diffusion with LMS algorithm both with raster scanning and diagonal scanning of the image. The quality measure for the resulting images are the observer's evaluations and whiteness comparison of the power spectrum of the quantization noise images.

The step size parameter μ used in the implementation of the error diffusion with LMS is set to 0.95. A scaling coefficient of 0.9 is used which scales the error diffusion filter coefficients after each update. This means that all the errors are not fed back through this filter but only 90% of them are fed back to the input pixel before quantization. The forgetting factor parameter λ in error diffusion with QR-RLS adaptation is chosen as 0.95 so that errors in the past are deemphasized, and the algorithm adapts to the local variations in the image.

We first give the simulation results for the Sunset image. The original image is shown in Figure 2.7, and the quantized image with median cut algorithm [44] to 16 colors is given in Figure 2.8, respectively. The quantized image shows the contouring effect very clearly in sea and sky regions, and false contours appearing because of the small number of available colors to represent these slowly varying color changing regions. The error diffused image with Floyd-Steinberg filter is shown in Figure 2.9 where contouring is a little improved, but the performance is poor in edge regions, i.e. the region where the sky and sea merge. The color impulses in the form of dots of a color emerging on a different colored background are visible. The error diffused images by adaptive algorithms LMS and QR-RLS adaptation using raster scan are shown in Figure 2.10 and Figure 2.11 respectively. The LMS-based adaptive error diffusion shows improvement when compared to that of the Floyd-Steinberg's method in reducing the color impulses and the behavior in edge regions. However, as can be observed in Figure 2.11, nearly all of the problems of quantization and dithering are removed in QR-RLS based adaptive error diffusion. The sky and sea merge naturally, and the smooth transitions from one color to the next are successfully reproduced as in the original image. The error diffused image by LMS adaptation with diagonal scan is shown in Figure 2.12. There's slight improvement in removing the color impulses. The error diffused image by QR-RLS adaptation with diagonal scan is shown in Figure 2.13. These figures show that QR-RLS based adaptive error diffusion with both raster and diagonal processing are the most successful methods.

The areas of slowly varying regions, or areas of uniform intensity in an image are the most problematic regions for a halftoning algorithm. Therefore, a good measure for the quality of a halftoning technique is the ability to render these areas. In this context, the proposed method gives the best result.

As a performance measure, we use the power spectra of the quantization error as pointed out in [18]. We estimate the power spectrum of the quantization error for the resulting images by Welch's periodogram averaging method [45]. We compare estimates for LMS with raster scan, and with diagonal scan, QR-RLS with raster scan and diagonal scan, and Floyd-Steinberg's method.

In Figure 2.14, the spectrum of the quantization errors in a horizontal line of the Sunset image is shown. Since it is difficult to plot 2-D spectrum, the spectrum of a line of the image is shown here. As can be observed from these plots, the power spectrum of the image error diffused by the QR-RLS adaptation method has not only the lowest energy but also the flattest response whereas the error diffusion with Floyd-Steinberg has the highest energy. The LMS-based method lies between the two curves. This experiment verifies the fact that QR-RLS based method produces the best results. Similar results are obtained for other lines of the image.

All three algorithms are compared also for diagonal scanning scheme in Figure 2.14. Floyd-Steinberg's method always produces an error spectrum with the largest energy. The adaptive algorithms both reduce the energy with best performance corresponding to the QR-RLS based error diffusion method.

We also compare the power spectrum estimates for both types of order of processing the Sunset image, namely the raster and diagonal processing, as shown in Figure 2.15. In the first plot, we can see that the error spectrum for the error diffusion using LMS with diagonal scanning of the image is flatter than the one with raster processing, and has reduced energy.

The average error spectra over all lines of the image is shown in Figure 2.16. It is observed that the proposed method with QR-RLS adaptation shows the flattest response also for an average of the lines image. This verifies our observation that similar results are obtained for all lines of the image.

The simulation results for the well-known Peppers image are given next. The original Peppers image is shown in Figure 2.17, and the quantized image to 16 colors with median cut algorithm is shown in Figure 2.18. False contours are clearly visible particularly on the green pepper in the middle because it has slowly varying color regions on its body from green to red and again to green and so on. This is again one of the problematic regions of the Peppers image. Figure 2.19 shows the image error diffused by Floyd-Steinberg's method. White color impulses on the upper red pepper are observed. Actually, we can see that Floyd-Steinberg's method produces very poor results in the edge regions which are smeared to each other. The color impulses are highly visible, and color shifts especially in the top region of the pepper in the middle is very disturbing. The Peppers image error diffused with LMS adaptation shown in Figure 2.20 shows better performance, and improves the behavior in edge regions. The color impulses are eliminated. However, the contouring effects in the mentioned problematic region are disturbing because the transition is not smooth. The resulting image error diffused with QR-RLS adaptation is shown in Figure 2.21. It is observed that this image shows the most superior performance among the error diffusion methods discussed so far. It is sharper and brighter, and the problematic region shows smooth transition for the slowly varying colors. The images for the adaptive error diffusion methods with diagonal scanning are given in Figure 2.22, and Figure 2.23. The image error diffused with QR-RLS adaptation gives the highest quality output.

For the Peppers image, we also plot the error power spectra for the three algorithms in Figure 2.24. The performance of the adaptive methods for the raster scan is such that the method with QR-RLS gives the lowest energy and flattest response. The one with LMS gives the second lowest energy response. The Floyd-Steinberg's method has the highest energy. For the diagonal scan, LMS shows improvement and has a lower energy error spectrum than that of the raster scan.

The error spectra for raster and diagonal scanning of both adaptive error diffusion methods are shown in Figure 2.25. The average of the error spectra over all lines of the image for the three methods is shown in Figure 2.26. Therefore, on the overall response, the error spectra of the adaptive error diffusion method QR-RLS adaptation shows the flattest response.

The simulation results for the Minnesota image are given in the following. The original image in Figure 2.27 is quantized to 16 colors with the median cut algorithm as shown in Figure 2.28. False contours and edges are visible in the quantized image particularly in the sky region. The image error diffused with Floyd-Steinberg's method shown in Figure 2.29 creates color impulses, and the edges are smeared to each other. These artifacts, color impulses and false edges, are reduced in adaptive error diffusion algorithms. The one with LMS adaptation is shown in Figure 2.30. Although the color impulses are eliminated, there are still false contours in slowly varying regions, and edges are converted into jagged edges. The error diffusion with QR-RLS adaptation results in the image in Figure 2.31 which shows the best performance. The sky has almost nearly smooth transition from one color to the next. The edge regions are sharper. The images in Figure 2.32 and Figure 2.33 are obtained by diagonal scan which shows some improvement when compared to those of raster scan. Diagonal scanning of the image produces better performance in removing the false contours in the sky.

Simulations for a smaller number of colors in the resulting image are carried out for the Minnesota image. The original Minnesota image in Figure 2.27 is quantized to 8 colors as shown in Figure 2.34. The false contours in the sky region are farther emphasized in this case because the number of colors is very small to represent the smooth transition in the sky region. The image in Figure 2.35 is error diffused with Floyd-Steinberg's method. The same problems are visible with more emphasis on the contouring effect. Figure 2.36 shows the image error diffused with LMS adaptation, and Figure 2.37 shows the same case with diagonal scanning. Here, we compare the raster scan and diagonal scan. As can be observed, the image with diagonal scanning eliminates a larger number of color impulses, and shows better performance. The images error diffused with QR-RLS adaptation both with raster scan and diagonal scan are shown in Figure 2.38, and Figure 2.39, respectively. The one with diagonal scanning has less number of color impulses, and it is somewhat brighter. We asked five people to evaluate the resulting error diffused images both with raster scan and diagonal scan in these four figures. All of them evaluated the images processed with diagonal scanning to have better quality in this case where the number of bits/pixel is low.

The power spectrum estimates of the three methods for the Minnesota image is shown in Figure 2.40. The same observations for the error spectra of this image are made. The error spectra for the error diffusion with QR-RLS adaptation shows the flattest response with the least energy where the Floyd-Steinberg's method has the highest energy, and the error diffusion with LMS adaptation lies in between. As can be observed from Figure 2.41, the diagonal scanning of the image improves the quality of the image since it flattens the error spectrum. The difference between the error spectra for the error diffusion with QR-RLS adaptation with raster scan and diagonal scan shown in Figure 2.41 is negligible. The average of the error spectra over all lines of the image for the three methods is shown in Figure 2.42.

Similar results can be obtained for other images as well. Our simulation studies show that QR-RLS algorithm in error diffusion outperforms deterministic and LMS type error diffusion algorithms. Since QR-RLS algorithm is much more successful in tracking the nonstationary image characteristics than the LMS algorithm, the resulting image quality is better.

The improvement is due to higher quality prediction in the error diffusion process. This is achieved by employing the QR-RLS method which is computationally more complex than the LMS algorithm.

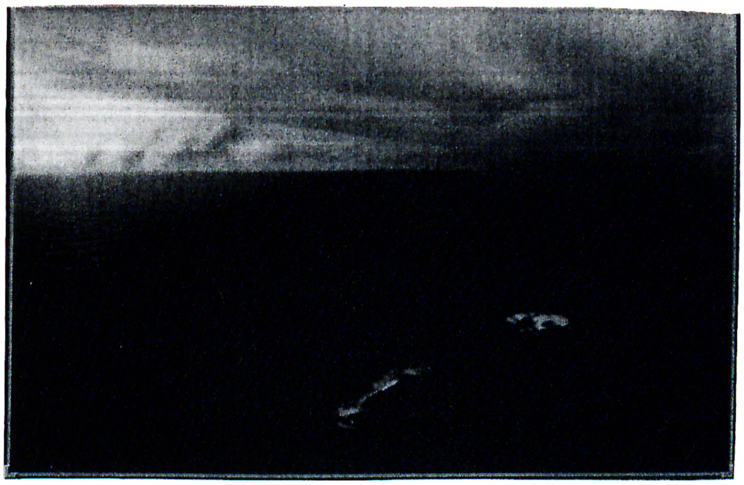

Figure 2.7: Original Sunset Image

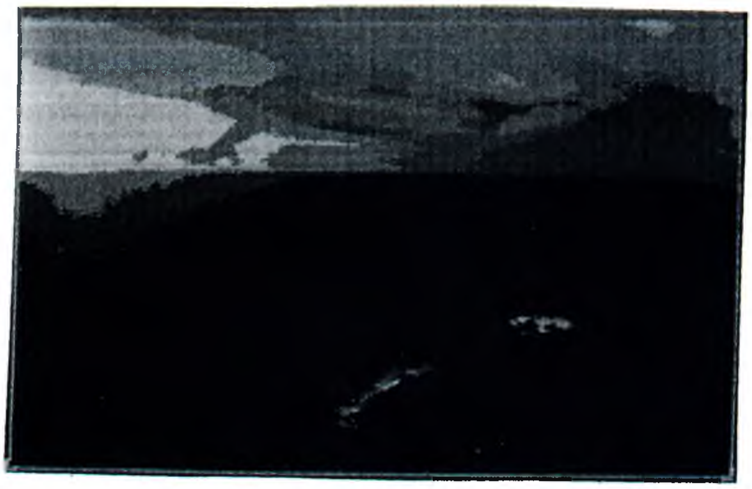

Figure 2.8: Quantized Sunset Image (16 colors)

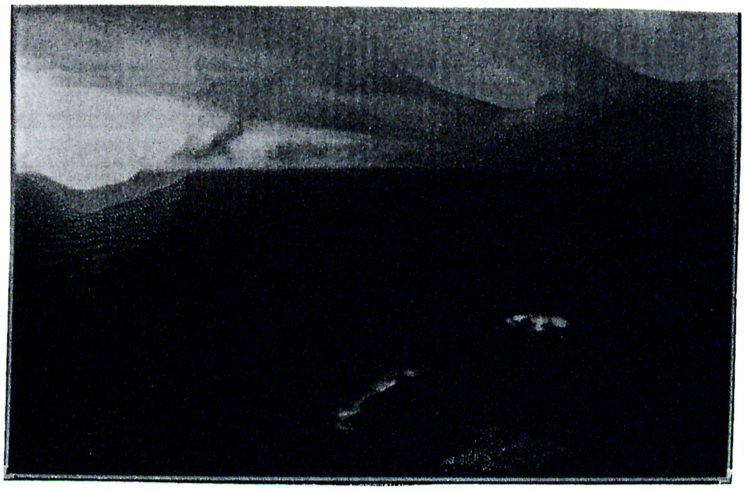

Figure 2.9: Error-diffused Sunset Image with Floyd-Steinberg's Method

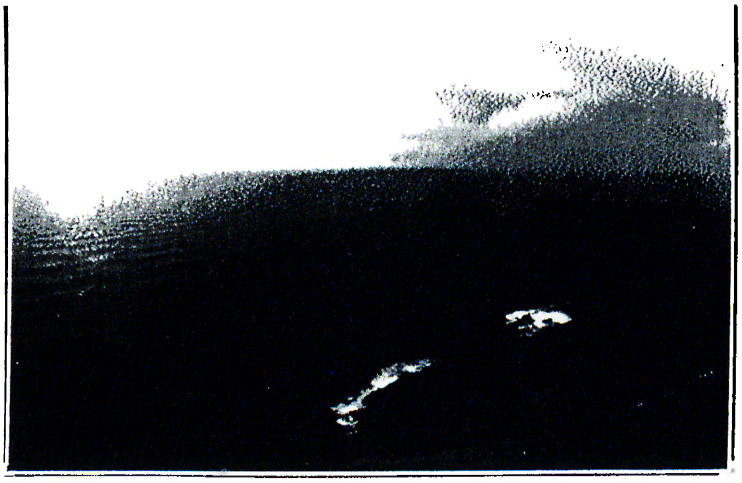

Figure 2.10: Error-diffused Sunset Image with LMS adaptation

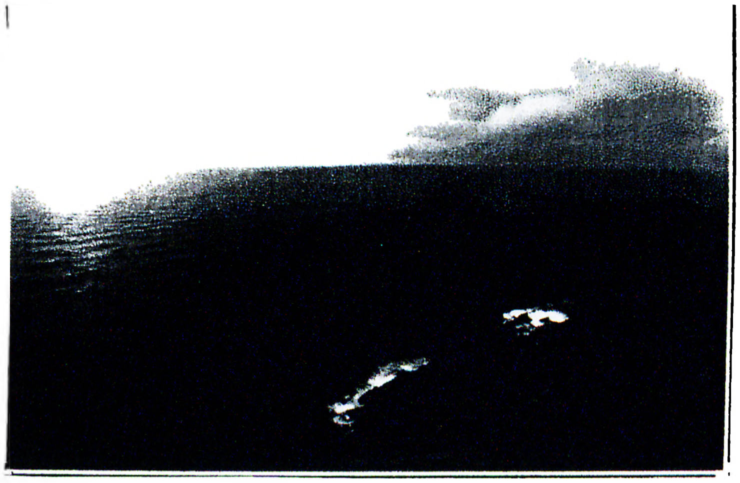

Figure 2.11: Error-diffused Sunset Image with QR-RLS adaptation

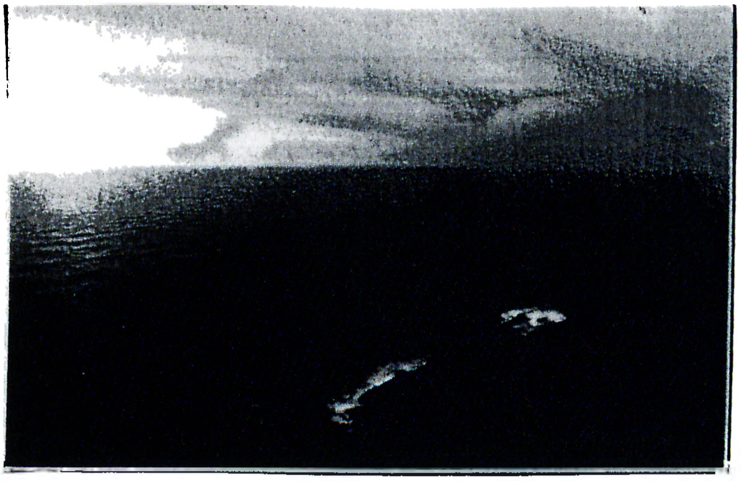

Figure 2.12: Error-diffused Sunset Image with LMS adaptation (diagonal scan)

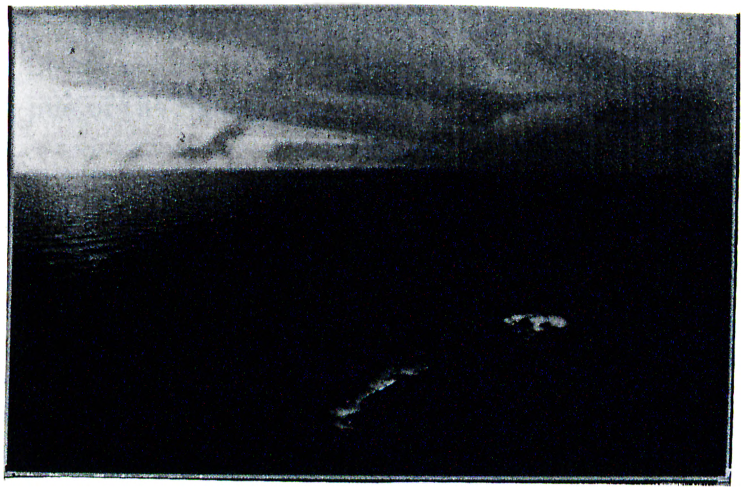

Figure 2.13: Error-diffused Sunset Image with QR-RLS adaptation (diagonal scan)

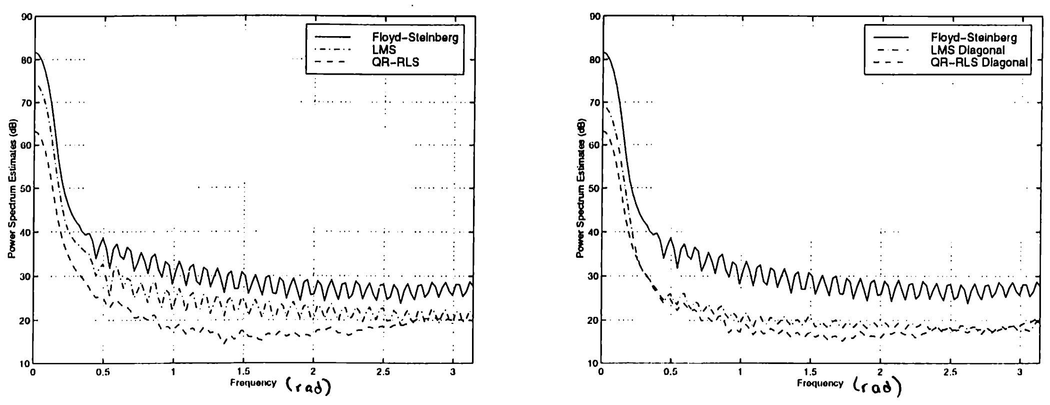

Figure 2.14: Comparison of the error spectra of a line of the Sunset image.

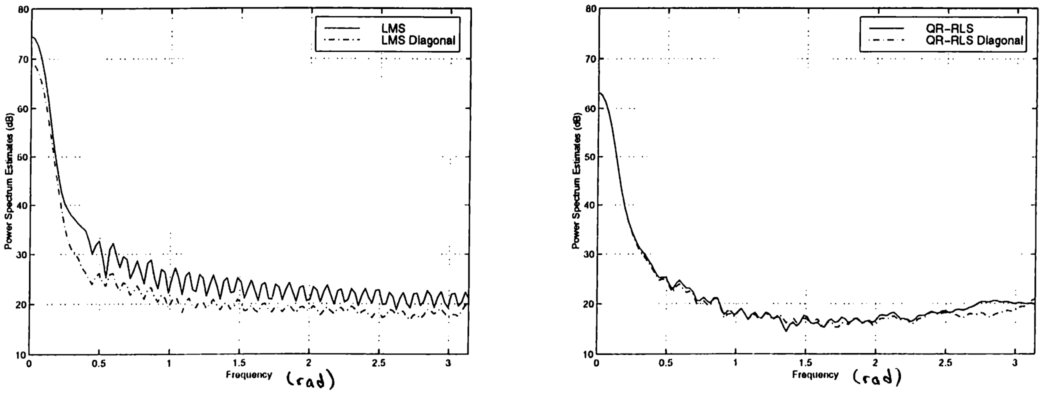

Figure 2.15: Comparison of the error spectra with raster scan and diagonal scan of a line of the Sunset image.

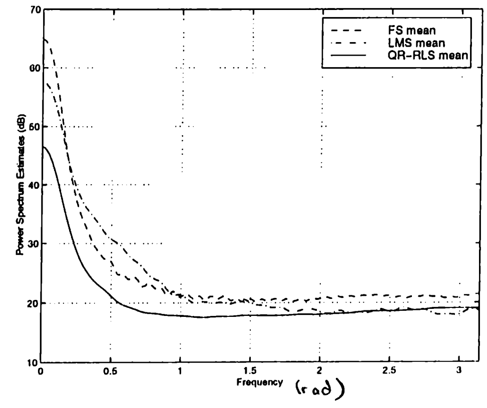

Figure 2.16: Comparison of the average error spectra over all lines of the Sunset image.

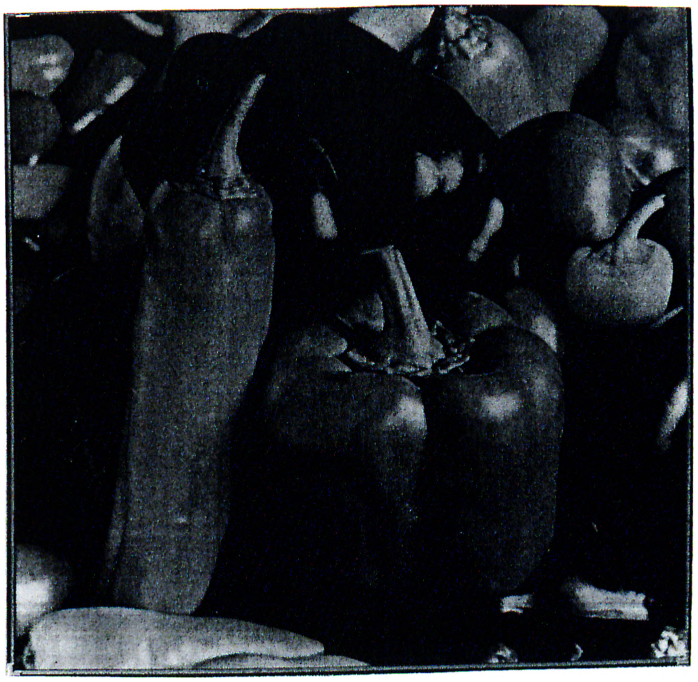

Figure 2.17: Original Peppers Image

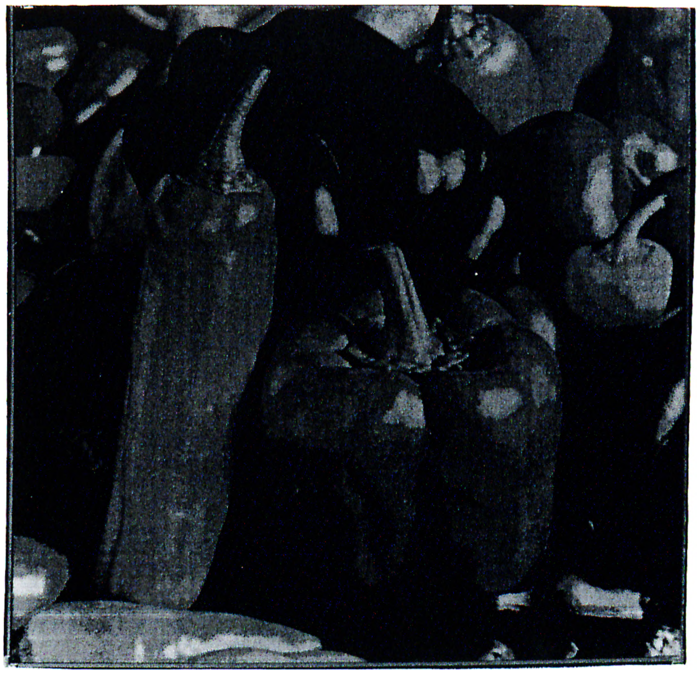

Figure 2.18: Quantized Peppers Image (16 colors).

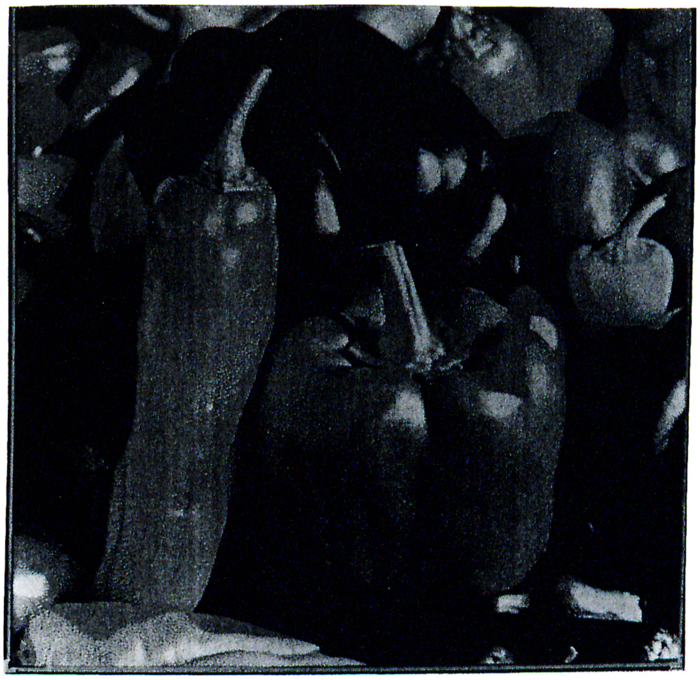

Figure 2.19: Error-diffused Peppers Image with Floyd-Steinberg's Method

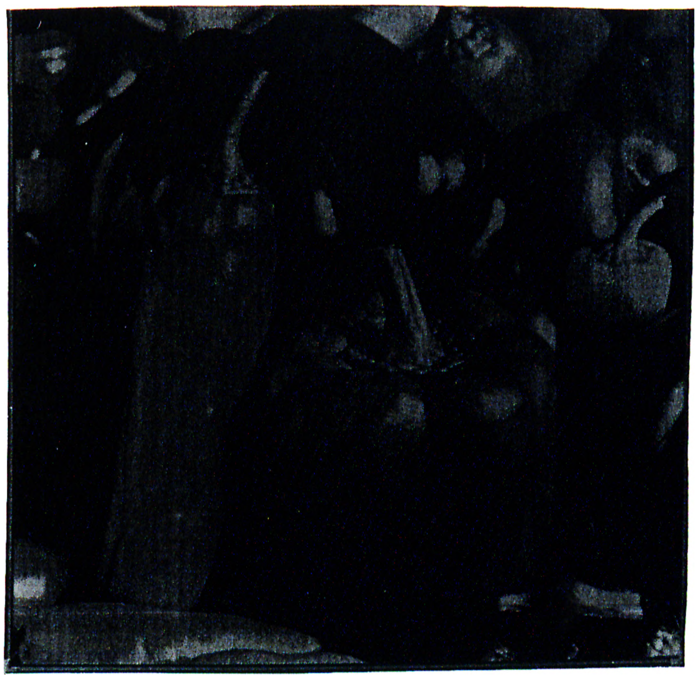

Figure 2.20: Error-diffused Peppers Image with LMS adaptation

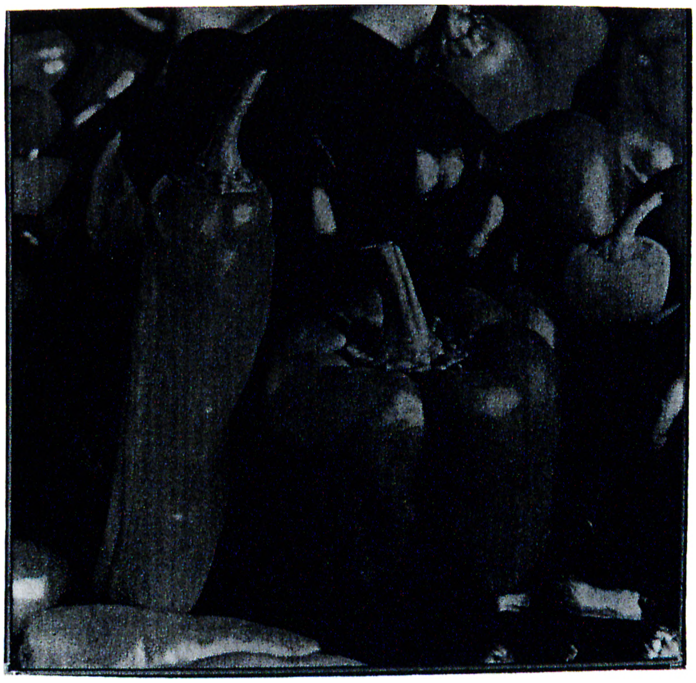

Figure 2.21: Error-diffused Peppers Image with QR-RLS adaptation

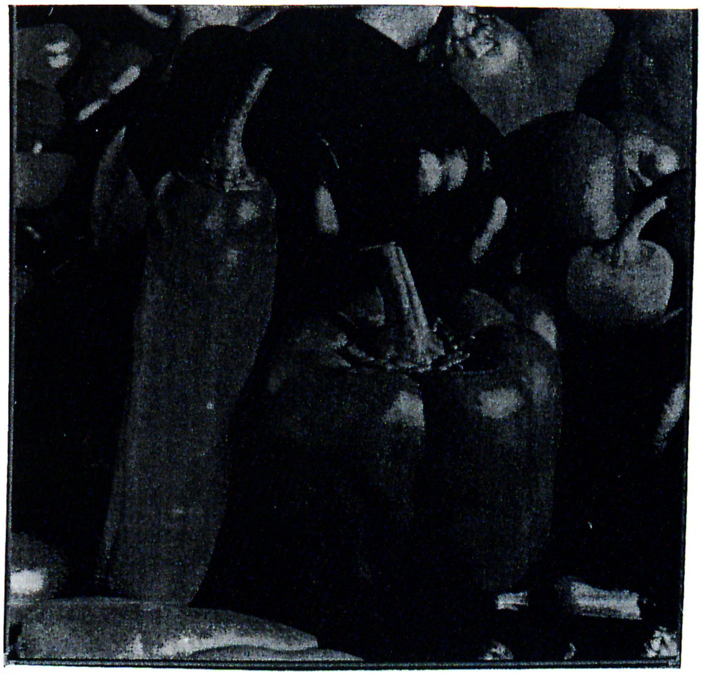

Figure 2.22: Error-diffused Peppers Image with LMS adaptation (diagonal scan)

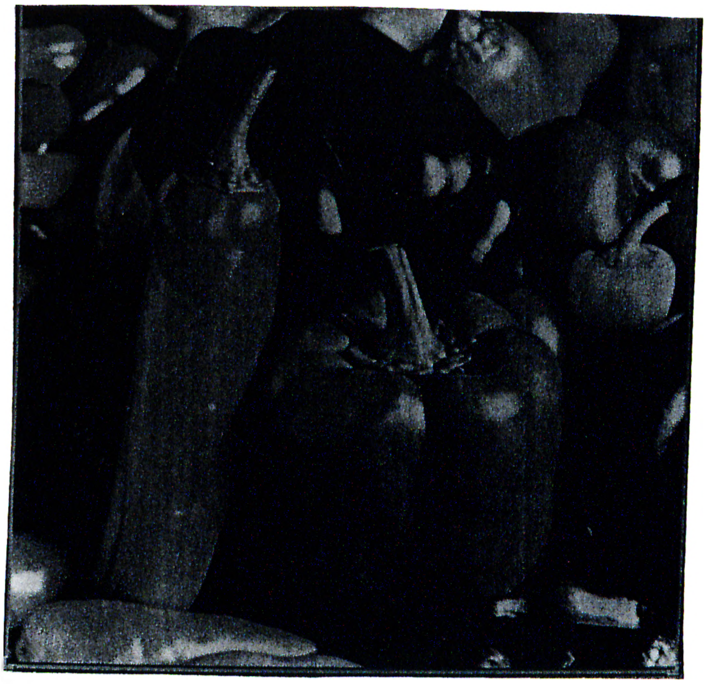

Figure 2.23: Error-diffused Peppers Image with QR-RLS adaptation(diagonal scan)

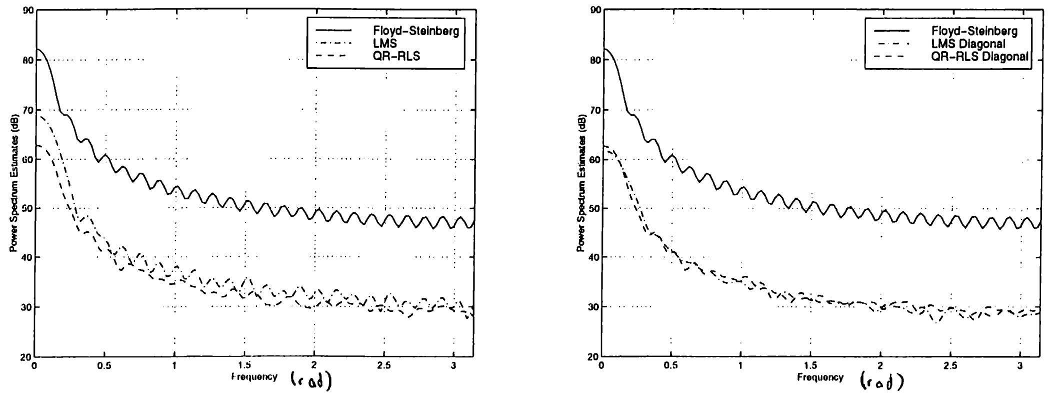

Figure 2.24: Comparison of the error spectra of a line of the Peppers image.

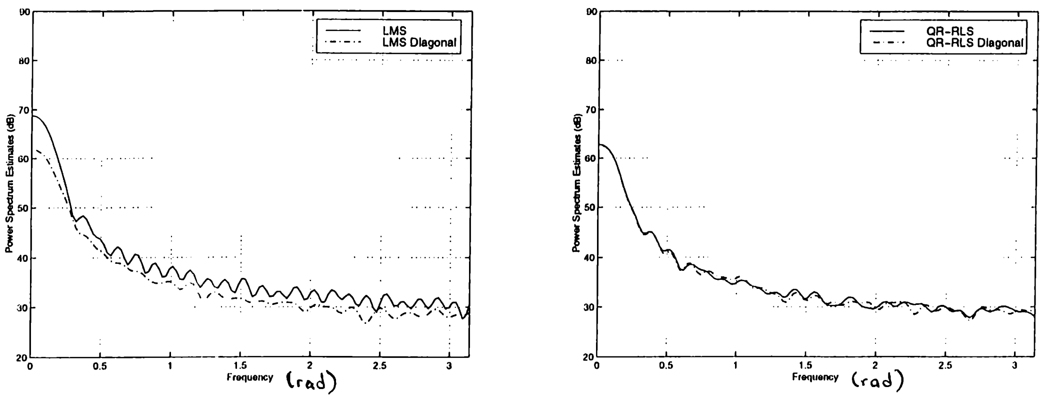

Figure 2.25: Comparison of the error spectra with raster scan and diagonal scan of a line of the Peppers image.

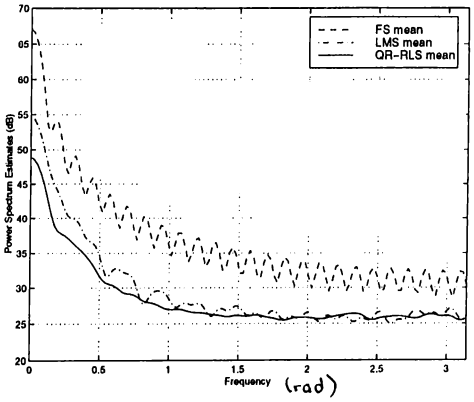

Figure 2.26: Comparison of the average error spectra over all lines of the Peppers image.

Figure 2.27: Original Minnesota Image

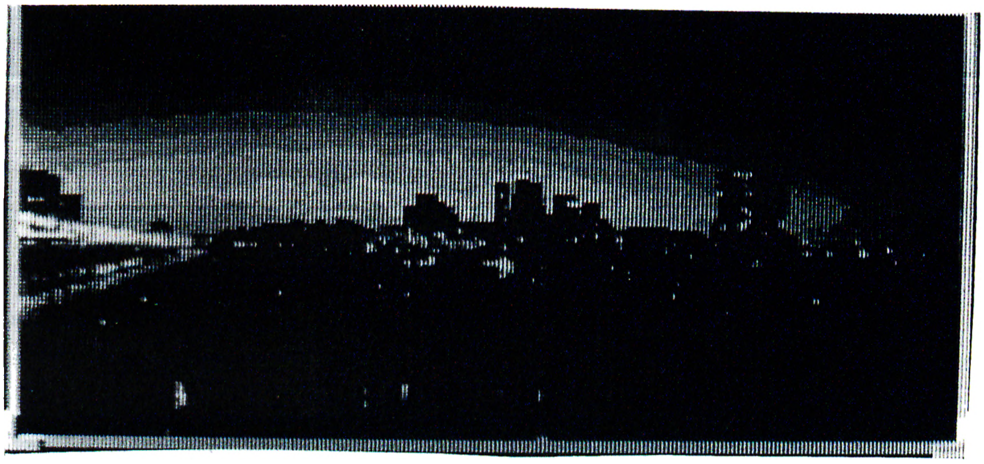

Figure 2.28: Quantized Minnesota Image (16 colors)

Figure 2.29: Error-diffused Minnesota Image with Floyd-Steinberg's method (16 colors)

Figure 2.30: Error-diffused Minnesota Image with LMS adaptation (16 colors)

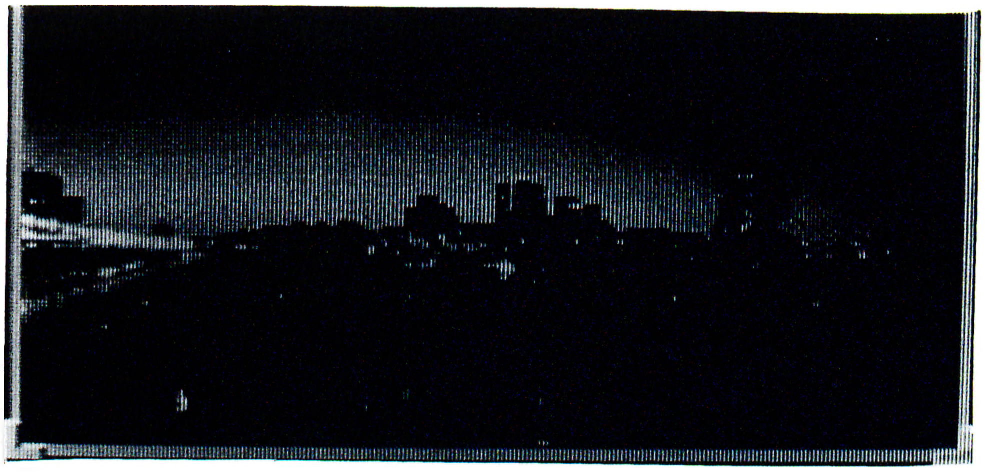

Figure 2.31: Error-diffused Minnesota Image with QR-RLS adaptation (16 colors)

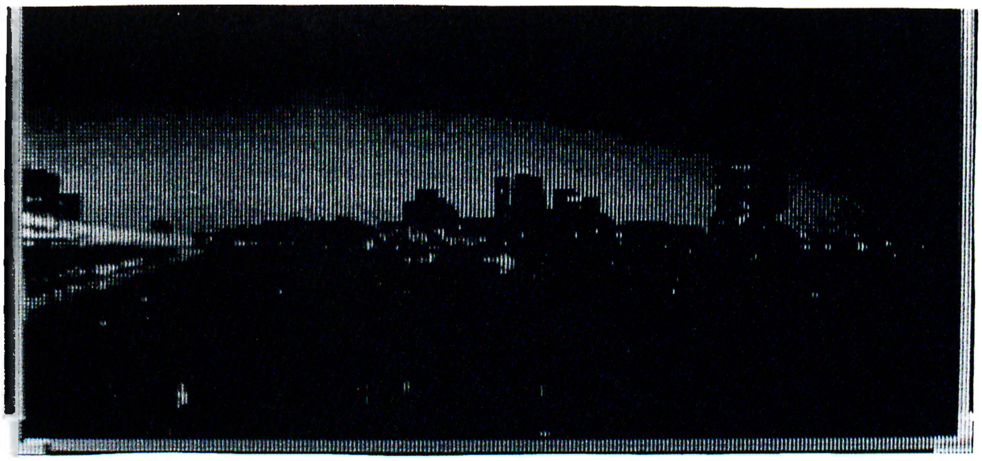

Figure 2.32: Error-diffused Minnesota Image with LMS adaptation (diagonal scan, 16 colors)

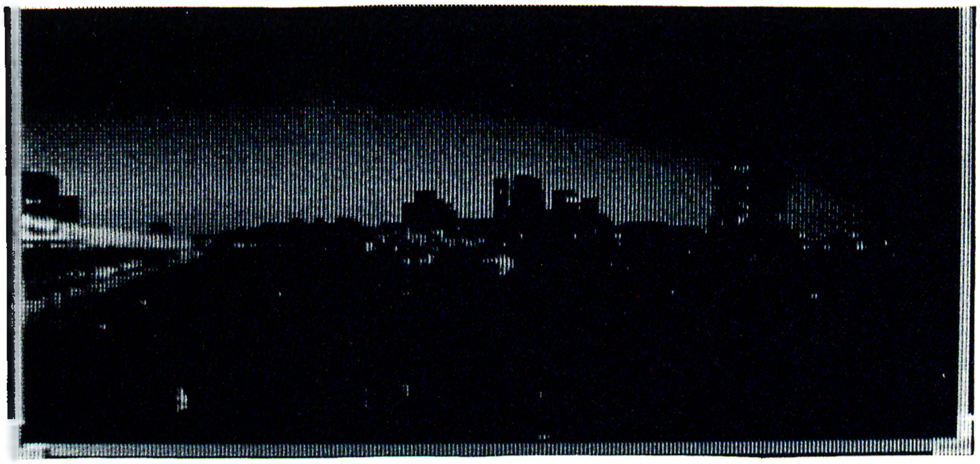

Figure 2.33: Error-diffused Minnesota Image with QR-RLS adaptation (diagonal scan, 16 colors)

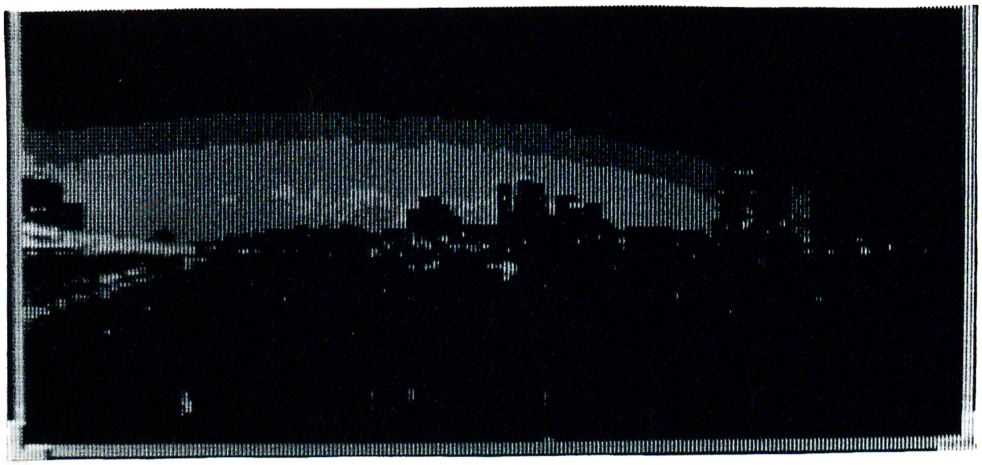

Figure 2.34: Quantized Minnesota Image (8 colors)

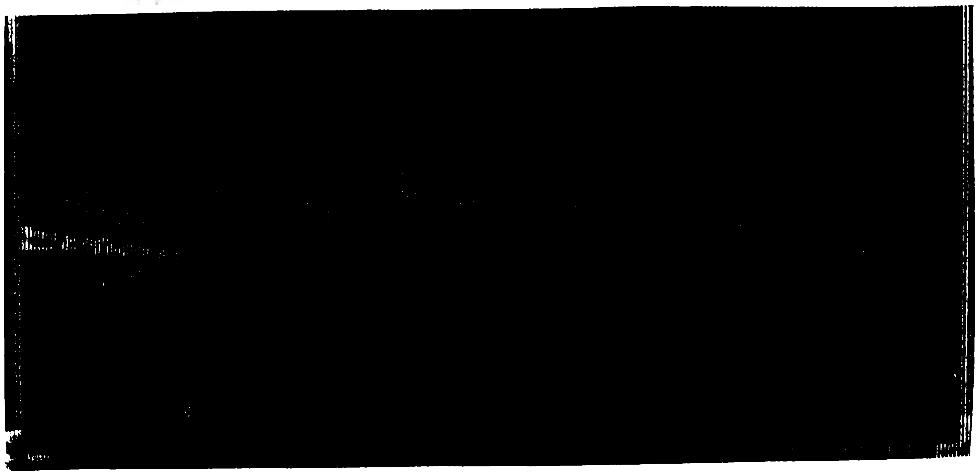

Figure 2.35: Error-diffused Minnesota Image with Floyd-Steinberg's method (8 colors)

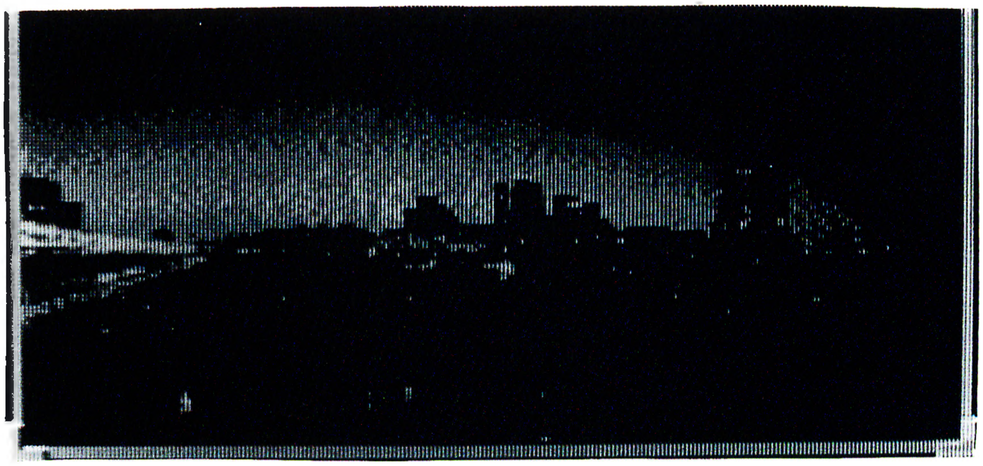

Figure 2.36: Error-diffused Minnesota Image with LMS adaptation (8 colors)

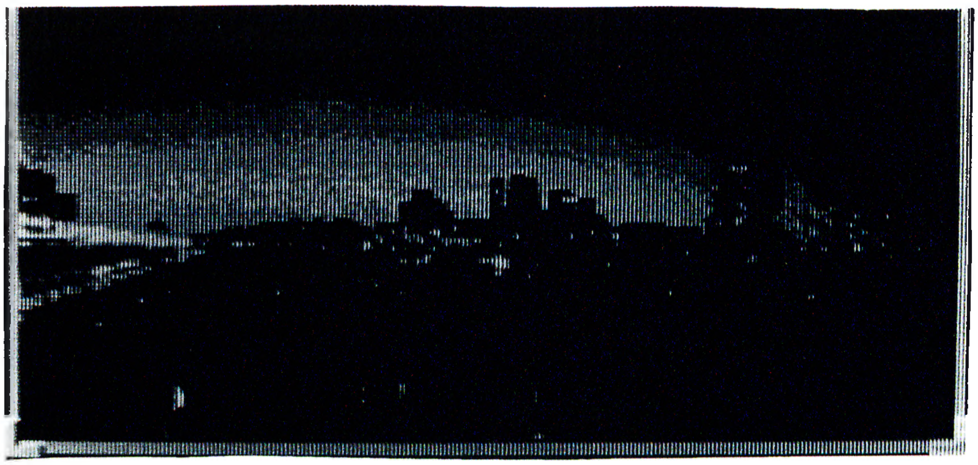

Figure 2.37: Error-diffused Minnesota Image with LMS adaptation (diagonal scan, 8 colors)

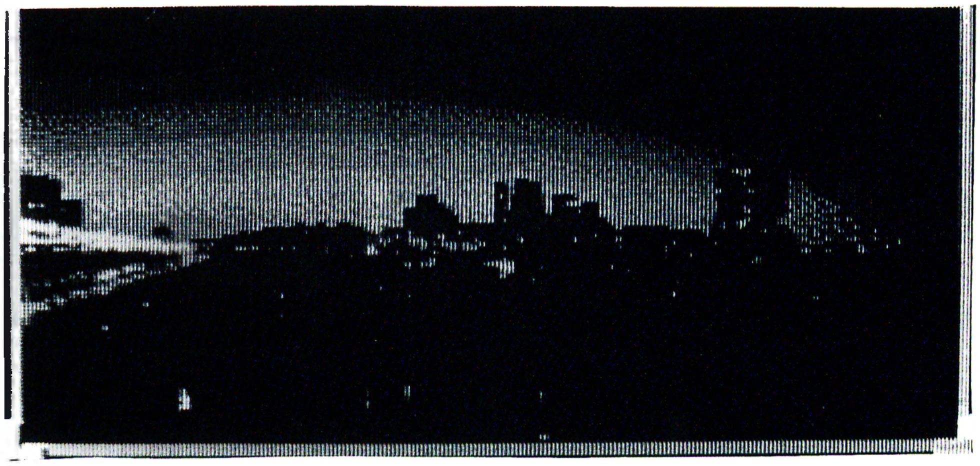

Figure 2.38: Error-diffused Minnesota Image with QR-RLS adaptation (8 colors)

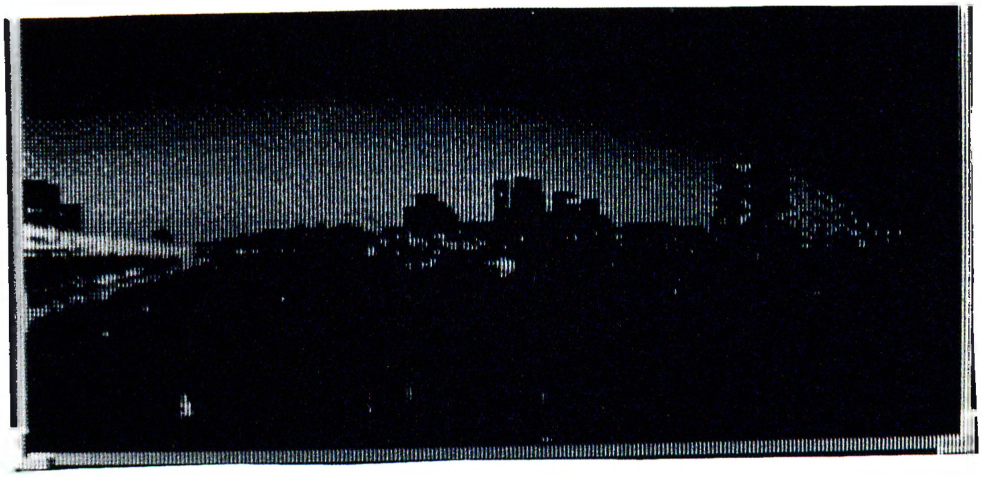

Figure 2.39: Error-diffused Minnesota Image with QR-RLS adaptation (diagonal scan, 8 colors)

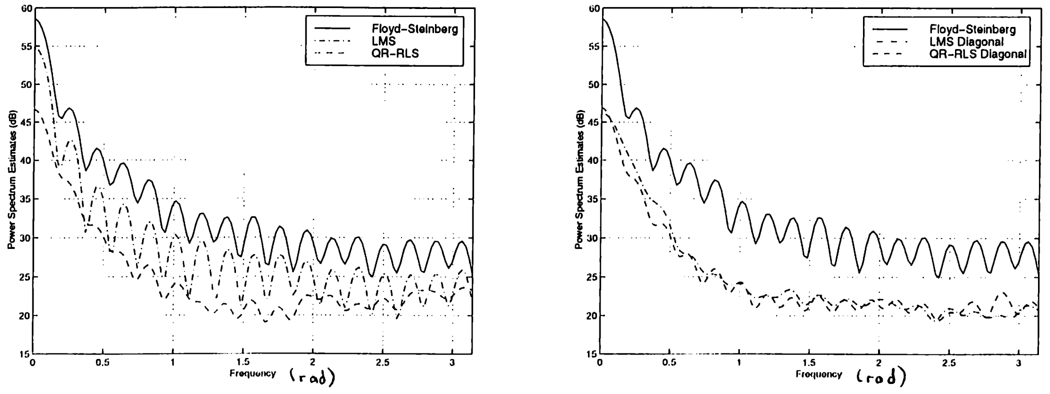

Figure 2.40: Comparison of the error spectra of a line of the Minnesota image.

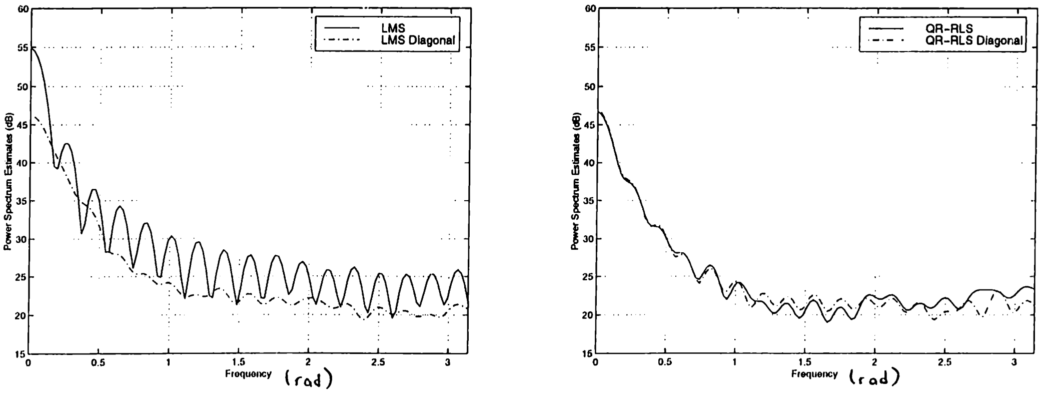

Figure 2.41: Comparison of the error spectra with raster scan and diagonal scan of a line of the Minnesota image.

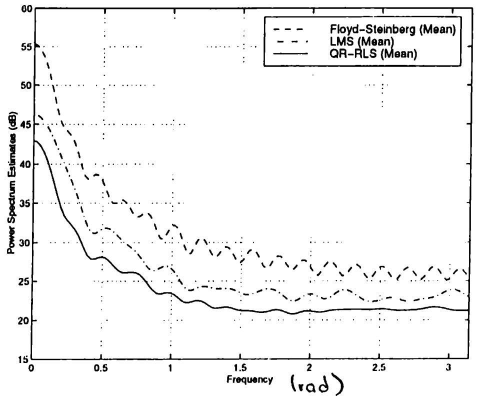

Figure 2.42: Comparison of the average error spectra over all lines of the Minnesota image.

Chapter 3

A SET THEORETIC INVERSE HALFTONING METHOD

In this chapter, a new inverse halftoning method based on the method Projection onto Convex Sets is proposed. Space, frequency, and space-scale domain projections are used which take advantage of the prior knowledge about the error diffusion filter kernel, and the relatively smooth character of the natural images. The simulation results are presented, and compared with some other inverse halftoning methods existing in the literature [33, 36, 37].

3.1 Background

As discussed in Chapter 1, halftoning is a process that deliberately injects noise into the original image in order to obtain visually pleasing output images for displaying or printing purposes. Therefore, inverse halftoning can be considered as a restoration problem. The aim is to reconstruct a high quality image from the observed image, which is a quantized and corrupted version of the original image. Conventionally, this type of estimation problems have been solved by optimizing an objective function with or without constraints [46]. However, the solution to the restoration problem of a continuous tone (contone) image from a given binary halftone image is not unique. This fact can be explained by a simple argument given by [33]. For images of size $N \times N$ at 8 bits per pixel, there are 256^{N^2} possible gray scale images. On the other hand, there is only a total of 2^{N^2} possible binary images of size $N \times N$. Therefore, there are many gray-scale images that can be halftoned into the same binary image, and the estimation problem can be considered as an ill-posed inverse problem. For ill-posed signal recovery problems of this type, incorporation of all available information significantly improves the quality of the solution. Our research is motivated by the fact that set theoretic formulation is ideally suitable for the inverse halftoning problem that has many feasible solutions.

3.1.1 Set Theoretic Formulation

The first basic component of a set theoretic formulation is the solution space Ξ that can take many forms, e.g., a space of matrices, functions or distributions [46]. The solution space is chosen such that all available information is modeled easily and accurately. Let us call the proposed solution $\boldsymbol{a}$ which belongs to the space Ξ for the image restoration problem. Let the property set $\boldsymbol{C}_k$ be the set representing information arising from the data and a priori knowledge about the problem. The pair $(\Xi, (\boldsymbol{C}_k)_{k\in I})$ is called a set theoretic formulation of the problem [46]. In the method of Projection onto Convex Sets (POCS), each piece of information is associated with a convex set, if possible, in the solution space, and the intersection of these sets, the feasibility set, represents the acceptable solutions [46]. Then the solution set $\boldsymbol{C}$ is given by

$$\boldsymbol{C} = \bigcap_{k\in I} \boldsymbol{C}_k \tag{3.1}$$

where any point in $\boldsymbol{C}$ is called a set theoretic estimate.

All available information usually does not describe the solution in the same domain. For instance, the available information may describe the signal in both time and frequency domains.

The structure of the solution space can be the Hilbert space of square-integrable functions where the metric is given by

$$d(\boldsymbol{a}, \boldsymbol{b}) = (\int_\Omega |\boldsymbol{a} - \boldsymbol{b}|^2 \mathrm{d}\mu)^{1/2}. \tag{3.2}$$

Another widely used Hilbert space is the k-dimensional Euclidean space $\mathcal{E}^k$ whose metric is given by $d(\boldsymbol{a}, \boldsymbol{b}) = (\sum_{i=1}^{k} |\boldsymbol{a}_i - \boldsymbol{b}_i|^2)^{1/2}$. Another example is the space $\mathcal{L}_n^2$ of Lebesgue square-integrable functions on $\mathcal{R}^n$ commonly used in n-dimensional signal recovery [1] [46].

$$\Xi = \mathcal{L}_n^2 = \{\boldsymbol{a} : \mathcal{R}^n \to \mathcal{R}, \quad | \quad \int_{\mathcal{R}^n} |\boldsymbol{a}(x_1, \ldots, x_n)|^2 dx_1 \ldots dx_n < +\infty\}. \tag{3.3}$$

Generating a set theoretic estimate is solving the feasibility problem

$$\text{Find} \quad \boldsymbol{a} \in \boldsymbol{C} = \bigcap_{k \in I} \boldsymbol{C}_k. \tag{3.4}$$

This problem can be usually solved not in one step but iteratively, and a sequence $(\boldsymbol{a}_n)_{n \geq 0}$ converges in some sense to a point in $\boldsymbol{C}$ [46]. The method of POCS is a widely used iterative method to develop an algorithm for finding a solution in the set $\boldsymbol{C}$. The key idea is to make successive orthogonal or relaxed projections onto the sets $\boldsymbol{C}_k$.

The distance from a point $\boldsymbol{a}$ to a nonempty subset $\boldsymbol{C}_k$ in a metric space (Ξ, d), is defined as

$$d(\boldsymbol{a}, \boldsymbol{C}_k) = \min \ d(\boldsymbol{a}, \boldsymbol{b}) \ \text{ subject to } \ \boldsymbol{b} \in \boldsymbol{C}_k. \tag{3.5}$$

A projection of $\boldsymbol{a}$ onto $\boldsymbol{C}_k$ is any point $\boldsymbol{b}$ in $\boldsymbol{C}_k$ such that $d(\boldsymbol{a}, \boldsymbol{C}_k) = d(\boldsymbol{a}, \boldsymbol{b})$. If Ξ is a Hilbert space and if $\boldsymbol{C}_k$ is closed and convex [2], every point $\boldsymbol{a}$ has a unique projection denoted as $P_k(\boldsymbol{a})$, onto $\boldsymbol{C}_k$.

Relaxed projection onto $\boldsymbol{C}$ is shown in Figure 3.1. The case $\lambda = 1$ corresponds to a projection (unrelaxed iteration), $0 < \lambda < 1$ to an underprojection, $1 < \lambda < 2$ to an overprojection, and $\lambda = 2$ to a reflection [46].

[1] $\mathcal{R}$ is the set of real numbers, $\mathcal{N}$ is the set of nonnegative integers.

[2] A set C is convex if for all $\boldsymbol{a}, \boldsymbol{b} \in C$, $\alpha\boldsymbol{a} + (1-\alpha)\boldsymbol{b} \in C$ for any $0 < \alpha < 1$.

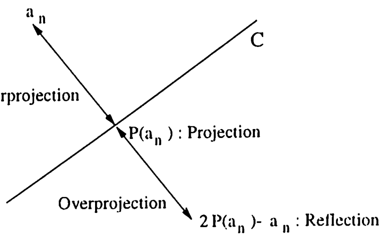

Figure 3.1: Relaxed projection onto $\boldsymbol{C}$.

A general serial [3] projection method is obtained by introducing variable relaxation parameters

$$(\forall n \in \mathcal{N}) \quad \boldsymbol{a}_{n+1} = \boldsymbol{a}_n + \lambda_n(P_{k_n}(\boldsymbol{a}_n) - \boldsymbol{a}_n) \tag{3.6}$$

where the sequence $(\lambda_n)_{n \geq 0}$ lies in [0,2]. The cyclic version of (3.6) is referred as POCS in literature [46].

Some widely used convex sets include the set of nonnegative signals,

$$\boldsymbol{C}_n = \{\boldsymbol{a} \in \mathcal{L}_1^2 \mid (\forall x \in \mathcal{R}) \ \boldsymbol{a}(x) \geq 0\}, \tag{3.7}$$

in the space $\mathcal{L}_1^2$, and the set of bandlimited signals,

$$\boldsymbol{C}_f = \{\boldsymbol{a} \in \mathcal{L}_1^2 \mid (\forall \nu \in \mathcal{R}) \ \mathcal{F}[\boldsymbol{a}](\nu) = 0 \quad \text{if} \quad |\nu| > D\} \tag{3.8}$$

where $\mathcal{F}[\boldsymbol{a}]$ denotes the Fourier transform of $\boldsymbol{a}$.

The property sets can be hyperplanes in $\mathcal{E}^k$, that is

$$\boldsymbol{C}_k = \{\boldsymbol{a} \in \mathcal{R}^k \mid <\boldsymbol{a}, \boldsymbol{b}_k> \ = \ \delta_k\} \tag{3.9}$$

where $\boldsymbol{b}_k$ is a nonzero vector in $\mathcal{R}^k$, δ_k is a real number, and the operator $<\boldsymbol{a}, \boldsymbol{b}>$ is a scalar product.

Closed half-spaces are also convex sets:

$$\boldsymbol{C}_k = \{\boldsymbol{a} \in \mathcal{R}^k \mid <\boldsymbol{a}, \boldsymbol{b}_k> \ \leq \ \delta_k\}. \tag{3.10}$$

Another widely used convex set model include hyperslabs:

$$\boldsymbol{C}_k = \{\boldsymbol{a} \in \mathcal{R}^k \mid \gamma_k \ \leq \ <\boldsymbol{a}, \boldsymbol{b}_k> \ \leq \ \delta_k\}, \tag{3.11}$$

[3] Projection is serial if only one set is activated at each iteration, and cyclic if $k_n = n(\text{modulo } m) + 1$, ($m$ is the number of property sets).

which can be written as the intersection of two half-spaces, so the previous projections apply for this case.

The solution to the constrained minimization problem in (3.5) may be tedious for some cases, and in turn, the computation of the projection at each iteration may be numerically costly. However, in the case of hyperplanes the solution can be found using the method of Lagrange multipliers [46], and the projection operator onto the hyperplane (3.9) is given by [46]

$$(\forall \boldsymbol{a} \in \mathcal{R}^k) \quad P_k(\boldsymbol{a}) = \boldsymbol{a} + \frac{\delta_k - < \boldsymbol{a}, \boldsymbol{b}_k >}{< \boldsymbol{b}_k, \boldsymbol{b}_k >} \boldsymbol{b}_k. \tag{3.12}$$

The projection onto hyperslabs and closed half-spaces are also based on Equation (3.12).

In the case of inverse halftoning, we exploit the information that is available to describe the solution in space, frequency, and space-scale domains. We model the space-domain information about the original image using hyperslabs. We also assume that the original image is band-limited in the frequency domain and use the set $\boldsymbol{C}_f$, and in space-scale domain, the Wavelet Transform (WT) extrema information is modeled as a convex set.

In our work, we assume that the halftoning process is performed with error diffusion technique, and the error diffusion filter kernel is known. For recovering the contone image from the halftone image, we alternate between space-domain projections, a space-scale domain projection, and a frequency-domain projection.

In [36], the method of POCS is also used for restoration of the original image from error diffused images, however exploiting only the space and frequency-domain projections. Furthermore, their space-domain projection is different from ours. In this thesis, we introduce a new space-domain projection for inverse halftoning based on projection onto hyperplanes. Our space-domain projections are computationally much simpler than that of [36].

A POCS method, based on projections onto hyperplanes, is developed in [47], for signal recovery from Discrete Wavelet Transform (DWT) extrema. It is shown that WT extrema information in space-scale domain of a signal or an image can be modeled as a hyperplane and by performing successive projections onto these hyperplanes, the original signal can be recovered for some cases. In [37], an inverse halftoning method using WT extrema information is developed. This noniterative method is based on estimating the edges of the original image from the halftoned image. In this method, the edges are represented using the WT extrema. Therefore, this method can be considered as a step of our iterative algorithm.

3.2 Method

In our inverse halftoning algorithm, we define three kinds of sets describing the prior information that we have. The set $\boldsymbol{C}_{1,s}$ contains all contone images that result in an observed error diffused pixel at the index s. The set $\boldsymbol{C}_1 = \bigcap_s \boldsymbol{C}_{1,s}$ is the set of all contone images $\boldsymbol{x}$ producing the observed error diffused image $\boldsymbol{y}$. The set $\boldsymbol{C}_2$ contains all band-limited contone images. Finally, the set $\boldsymbol{C}_3$ contains all the images having the same significant WT local extrema as the original image. These sets are shown to be convex in Appendix A.

The POCS based iterative algorithm starts with an initial estimate $\boldsymbol{x}_0$, which is successively projected onto the sets $\boldsymbol{C}_{1,s}$, $\boldsymbol{C}_2$ and $\boldsymbol{C}_3$, as follows

$$\boldsymbol{x}_{\ell+1} = (P_{1,0} \circ \ \ldots \ \circ P_{1,L} \circ P_2 \circ P_3)\boldsymbol{x}_{\ell}, \qquad \ell = 0, 1, 2, \ldots \tag{3.13}$$

where $P_{1,s}$ represents the spatial projection which will be described in the next subsection, (L is the total number of pixels in the image), P_2 represents lowpass filtering which is the frequency-domain projection, and P_3 represents the wavelet-domain method by Xiong, Orchard, and Ramchandran [37] which is the space-scale domain projection. All three projections, or any two can be used alternately. The order of the projections is immaterial [46]. The iterations are stopped when the difference between the signals at successive iterations become insignificant.

3.2.1 Space-Domain Projection

The block diagram of error diffusion encoder is given in Figure 3.2 for convenience. The inverse halftoning problem can be stated as follows: Given the halftoned image $\boldsymbol{y}$ and the 2-D FIR error diffusion filter kernel $\boldsymbol{h}$, we want to estimate the original image $\boldsymbol{x}$. The variable $\boldsymbol{u}$, which is the input to the quantizer plays a significant role because the hard quantizer operator $\boldsymbol{Q}$ determines the bounds on $\boldsymbol{u}$ for each output pixel $\boldsymbol{y}(s)$.

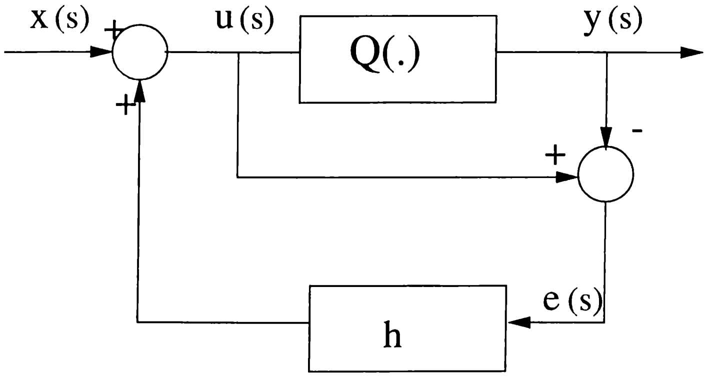

Figure 3.2: Block diagram of error diffusion method.

Rewriting the equations for the error diffusion system in Figure 3.2, we get,

$$\boldsymbol{e} = \boldsymbol{u} - \boldsymbol{y} \tag{3.14}$$

$$\boldsymbol{u} = \boldsymbol{x} + \boldsymbol{h} * \boldsymbol{e} \tag{3.15}$$

$$\boldsymbol{u} = \boldsymbol{x} + \boldsymbol{h} * (\boldsymbol{u} - \boldsymbol{y}) \tag{3.16}$$

$$(\boldsymbol{I} - \boldsymbol{h}) * \boldsymbol{u} = \boldsymbol{x} - \boldsymbol{h} * \boldsymbol{y}. \tag{3.17}$$

The image $\boldsymbol{u}$ can be expressed in terms of images $\boldsymbol{x}$ and $\boldsymbol{y}$ as

$$\boldsymbol{u} = (\boldsymbol{I} - \boldsymbol{h})^{-1} * [\boldsymbol{x} - \boldsymbol{h} * \boldsymbol{y}]. \tag{3.18}$$

Here $*$ denotes the convolution operation, and $\boldsymbol{x}$ is the estimate obtained at each iteration. The kernels for the FIR filters $\boldsymbol{h}$ and $\boldsymbol{I} - \boldsymbol{h}$ are given in Figure 3.3.

For convenience, we define

$$\bar{\boldsymbol{x}} = \boldsymbol{x} - \boldsymbol{h} * \boldsymbol{y}. \tag{3.19}$$

0	0	7/16
3/16	5/16	1/16

h

0	1	-7/16
-3/16	-5/16	-1/16

I-h

Figure 3.3: Kernels for the filters $\boldsymbol{h}$ and $\boldsymbol{I} - \boldsymbol{h}$.

The 2-D IIR inverse filter $\boldsymbol{w} = (\boldsymbol{I} - \boldsymbol{h})^{-1}$ can be approximated by a 2-D FIR filter using a method described in [41] for inverse filtering for image restoration. The size of the filter $\boldsymbol{w}$ is chosen as $m_1 \times m_2$.

The pixel $\boldsymbol{u}(s) = (\boldsymbol{w} * \bar{\boldsymbol{x}})(s)$ can be represented as $\boldsymbol{u}(s) = \sum_{k \in F_v} \boldsymbol{v}(k,s)\, \bar{\boldsymbol{x}}(k)$, where $\boldsymbol{v}$ is the mask corresponding to the filter $\boldsymbol{w}$, and F_v is the support of the mask $\boldsymbol{v}$. For convenience, 1-D indexing is used, although the blocks $\bar{\boldsymbol{x}}$ in F_v, and the mask $\boldsymbol{v}$ are 2-D signals. If the output sample $\boldsymbol{y}(s)$ is 0 then it means that $\boldsymbol{u}(s)$ is between 0 and 127 for 8 bits/sample contone images. Otherwise, $\boldsymbol{u}(s)$ is between 128 and 255. We use this information to form a constraint on the image $\bar{\boldsymbol{x}}$. In other words,

$$\begin{aligned}
&\text{if} \quad (\boldsymbol{y}(s) = 0 \;\text{ and }\; \boldsymbol{u}(s) \geq \delta_q) \text{ or } (\boldsymbol{y}(s) = 255 \;\text{ and }\; \boldsymbol{u}(s) < \delta_q) \\
&\text{then} \\
&\sum_{k \in F_v} \boldsymbol{v}(k,s)\, \bar{\boldsymbol{x}}(k) = \delta_q \qquad (3.20)
\end{aligned}$$

where δ_q is 128 in the case of the binary quantizer. Equation (3.20) is a hyperplane, therefore it is a convex set.

The projection onto the set $\boldsymbol{C}_{1,s}$ can be carried out as follows. Let $\bar{\boldsymbol{x}}_p$ be the current iterate. The next iterate $\bar{\boldsymbol{x}}_{p+1}$ is obtained by solving the optimization problem:

$$\min \quad \| \bar{\boldsymbol{x}}_{p+1} - \bar{\boldsymbol{x}}_p \|^2 \quad \text{subject to} \quad (3.20). \qquad (3.21)$$

Using Lagrange multipliers method for this constrained minimization problem, we obtain

$$\begin{aligned}
\mathcal{L} &= \| \bar{\boldsymbol{x}}_{p+1} - \bar{\boldsymbol{x}}_p \|^2 + \mu\Big(\sum_{k \in F_v} \boldsymbol{v}(k,s)\bar{\boldsymbol{x}}_{p+1}(k) - \delta_q\Big) \qquad (3.22) \\
\frac{\partial \mathcal{L}}{\partial \bar{\boldsymbol{x}}_{p+1}(j)} &= 2(\bar{\boldsymbol{x}}_{p+1}(j) - \bar{\boldsymbol{x}}_p(j)) + \mu \boldsymbol{v}(j,s) \qquad j = 1, 2, \ldots, M \quad (3.23)
\end{aligned}$$

$$\frac{\partial \mathcal{L}}{\partial \mu} = \sum_{k\in F_v} \boldsymbol{v}\,(k,s)\bar{\boldsymbol{x}}_{p+1}(k) - \delta_q \tag{3.24}$$

($M = m_1 \times m_2$, the size of the inverse filter $\boldsymbol{w}$). Equating (3.23) and (3.24) to 0, and rewriting them gives:

$$\begin{aligned} \bar{\boldsymbol{x}}_{p+1}(\jmath) &= \bar{\boldsymbol{x}}_{p}(\jmath) + \frac{\mu}{2}\,\boldsymbol{v}\,(\jmath,s) && (3.25) \\ \sum_{k=1}^{M} \boldsymbol{v}\,(k,s)(\bar{\boldsymbol{x}}_{p}(k) + \frac{\mu}{2}\,\boldsymbol{v}\,(k,s)) &= \delta_q && (3.26) \end{aligned}$$

From (3.26)

$$\frac{\mu}{2} = \frac{\delta_q - \sum_k \boldsymbol{v}\,(k,s)\bar{\boldsymbol{x}}_{p}(k)}{\sum_k \boldsymbol{v}\,(k,s)^2} \tag{3.27}$$

Putting μ into (3.25),

$$\bar{\boldsymbol{x}}_{p+1} = \bar{\boldsymbol{x}}_{p} + \lambda\left(\frac{\delta_q - \sum_k \boldsymbol{v}\,(k,s)\bar{\boldsymbol{x}}_{p}(k)}{\sum_k \boldsymbol{v}\,(k,s)^2}\right)\boldsymbol{v} \tag{3.28}$$

where λ is a relaxation parameter and if it remains between 0 and 2, the convergence of the POCS procedure is assured [46].

The projection given in (3.28) is performed pixel by pixel involving the block defined by the causal mask $\boldsymbol{v}$ in the image $\bar{\boldsymbol{x}}$. Block size is equal to the support size of the inverse filter $\boldsymbol{w}$.

Once we obtain the corrected image $\bar{\boldsymbol{x}}$, we get the new estimate $\boldsymbol{x}$ by the equation

$$\boldsymbol{x} = \bar{\boldsymbol{x}} + \boldsymbol{h} * \boldsymbol{y}\,. \tag{3.29}$$

This scheme can be easily extended to the case of multi-level error-diffusion in which the quantizer is not binary. In this case, the image $\boldsymbol{u}$ is quantized to K gray levels by error-diffusion coding, and we want to obtain full gray-scale image. Here,

$$\begin{array}{ccccc} \boldsymbol{A}\,(s) & \leq & \mathbf{u}(s) & \leq & \boldsymbol{B}\,(s) \\ \boldsymbol{A}\,(s) & \leq & \sum_{k\in F_v} \boldsymbol{v}\,(k,s)\bar{\boldsymbol{x}}\,(k) & \leq & \boldsymbol{B}\,(s) \end{array} \tag{3.30}$$

where the matrices $\boldsymbol{A}$ and $\boldsymbol{B}$ define the quantizer bounds corresponding to the sample $\boldsymbol{u}\,(s)$. For the binary quantizer, $\boldsymbol{A}\,(s) = \boldsymbol{u}_{low}(s) = 0$, and $\boldsymbol{B}\,(s) = \boldsymbol{u}_{high}(s) = 128 - \epsilon$ for the output 0, and $\boldsymbol{A}\,(s) = \boldsymbol{u}_{low}(s) = 128$, and $\boldsymbol{B}\,(s) =$

$\boldsymbol{u}_{high}(s) = 255$ for the output 255. For a multi-level uniform quantizer, $\boldsymbol{u}_{low}(s)$ and $\boldsymbol{u}_{high}(s)$ are determined according to the quantizer bounds. Depending on the error-diffusion encoding type, i.e., either binary or multilevel encoding, the matrices $\boldsymbol{A}$ and $\boldsymbol{B}$ are determined from the halftoned image beforehand. Inherently, $\boldsymbol{A}(s) \leq \boldsymbol{B}(s)$ at every pixel s. If the sample $\boldsymbol{u}(s)$ does not satisfy the bounds in (3.30) then the current iterate $\bar{\boldsymbol{x}}_p$ is updated so that the next iterate $\bar{\boldsymbol{x}}_{p+1}$ satisfies it using Equation (3.28). In the multi-level case, δ_q is chosen as follows

$$\text{if} \quad \sum_k \boldsymbol{v}(k,s)\bar{\boldsymbol{x}}_p(k) < \boldsymbol{u}_{low}(s) \Longrightarrow \delta_q = \boldsymbol{u}_{low}(s). \tag{3.31}$$

$$\text{if} \quad \sum_k \boldsymbol{v}(k,s)\bar{\boldsymbol{x}}_p(k) > \boldsymbol{u}_{high}(s) \Longrightarrow \delta_q = \boldsymbol{u}_{high}(s). \tag{3.32}$$

Once $\bar{\boldsymbol{x}}_{p+1}$ is determined the corresponding image $\boldsymbol{x}_{p+1}$ is determined using Equation (3.29).

Since there are many solutions to the restoration problem, one has to use as much information as possible to find the original image.

3.2.2 Frequency-Domain Projection

An important property of most natural images is smoothness compared to artificial images. This information can be imposed into the restoration process in the form of lowpass filtering.

Therefore, the frequency-domain projection consists of bandlimiting the observed signal in some way. The simplest approach is lowpass filtering the image in order to remove the high-frequency components of the image, which contain mostly halftoning noise. It should be noted that error-diffusion coding deliberately forces the halftoning error to high-frequency components to which the human visual system is less sensitive. Simple lowpass filtering can be carried out by Gaussian lowpass filtering, or halfband lowpass filtering [33]. Another lowpass filtering approach, is based on singular value decomposition(SVD) [36].

In this thesis, for the frequency-domain projection, we use either a simple Gaussian lowpass filter, or a lowpass filter with a specific passband region.

The passbands of the lowpass filters we use are $[-\pi/2, \ \pi/2] \times [-\pi/2, \ \pi/2]$, $[-2\pi/3, \ 2\pi/3] \times [-2\pi/3, \ 2\pi/3]$, or $[-3\pi/4, \ 3\pi/4] \times [-3\pi/4, \ 3\pi/4]$.

3.2.3 Space-Scale Domain Projection

The edges in an image produce local WT extrema in the space-scale domain [48]. It is proved that the wavelet extrema information correspond to convex sets in $\mathcal{L}_2^2$ which is the set of square summable images [47–49]. Therefore, the edge information can be used in the reconstruction algorithm by properly defining a set corresponding to the significant local extrema in the wavelet domain. Let the set $\boldsymbol{C}_3$, contain all the images having the same significant WT local extrema as the original image. It is well-known that the wavelet domain extrema information correspond to the edges of the original image. The key idea is to estimate the edges of the original image from the halftoned image by selecting the significant WT extrema of the halftoned image, and the restored image is forced to have the same extrema in the wavelet space-scale domain. This provides the sharpness to the restored image by protecting the significant high frequency components of the image, whereas a simple lowpass filtering characterized by set $\boldsymbol{C}_2$ will smooth out all of the sharp edges of the original image. The projection onto this set can be carried out as described in [37], which is a wavelet-based single step inverse halftoning method. Important high frequency information describing the signal, particularly information in edge regions, are retained by choosing the WT extrema locations selectively from each subband resulting from the wavelet decomposition of the halftoned image. Wavelet space-scale method of Xiong, Orchard, and Ramchandran [37] is not an orthogonal projection onto a convex set due to cross-scale correlation operation which will be explained next. However, we can incorporate their method as an initial step in our iterative restoration method.

We briefly review the wavelet-based inverse halftoning method of [37]. The block diagram is given in Figure 3.4. First, a one scale discrete dyadic wavelet decomposition of the halftoned image is performed. The lowpass wavelet image S_1y, a horizontal highpass image $W_1^H y$, and a vertical highpass image $W_1^V y$, all of the same size as the input $\boldsymbol{y}$ are formed. The noise in highpass wavelet images are suppressed by a simple Gaussian lowpass filter. The remaining significant extrema are used in the edge information.

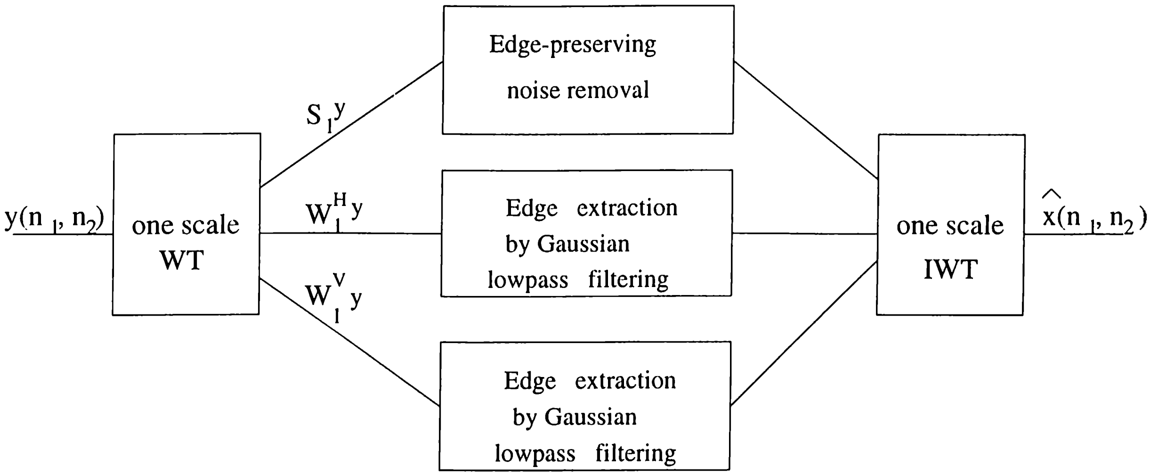
y(n 1, n2)
one scale WT
S1y
W1H y
W1V y
Edge-preserving noise removal
Edge extraction by Gaussian lowpass filtering
Edge extraction by Gaussian lowpass filtering
one scale IWT
^x(n 1, n2)

Figure 3.4: Block diagram of the wavelet-based inverse halftoning scheme in [37].

For the edge-preserving noise removal from the lowpass wavelet image S_1y, the idea in [50] is employed by this scheme. Edges can be located effectively based on the direct spatial correlation of the wavelet transform at several adjacent scales [50]. By directly multiplying cross-scale highpass wavelet coefficients at scales 2 and 3, two edge maps, one vertical and one horizontal, are generated as $E^{\circ}(n_1, n_2) = W_2^{\circ}y(n_1, n_2)\ W_3^{\circ}y(n_1, n_2)$, $(\circ \in \{H, V\})$. Edge extraction is done by thresholding the sum of the two edge maps $E(n_1, n_2) = E^H(n_1, n_2) + E^V(n_1, n_2)$. The pixel values where the overall edge map is higher than the threshold are identified as edge pixel, while the remaining are identified as background noise. The highpass wavelet images $W_2^H y$, and $W_2^V y$ are set to zero at pixel locations corresponding to background regions. Then, the lowpass wavelet image S_1y is reconstructed from S_2y, and the modified $W_2^H y$ and $W_2^V y$ images. Finally, as shown in Figure 3.4, the contone image estimate is obtained through the reconstruction by an inverse wavelet transform.

3.3 Simulation Results

The simulations are carried out using 8 bits/pixel Lena and Peppers images of size 512 × 512 to test the performance of our POCS based inverse halftoning method. For the space-domain projection, we use our spatial projection explained in Section 3.2.1, for the frequency projection, we use either Gaussian lowpass filtering (GLPF) or lowpass filtering (LPF) with various passbands, and for the space-scale projection, we use wavelet-based method in [37]. For the space-domain projection, the block size, i.e. the size of the inverse filter mask $\boldsymbol{v}$, is set to 50 × 51. We compare the results of our proposed method with inverse halftoning methods in [33,36,37].

The Peak-Signal-to-Noise-Ratio (PSNR) between two $N \times N$ images $\boldsymbol{x}$ and $\hat{\boldsymbol{x}}$ is defined as

$$\mathrm{PSNR} = 10 \log \frac{255^2}{\frac{1}{N^2} \sum_{n_1=0}^{N-1} \sum_{n_2=0}^{N-1} [\boldsymbol{x}\,(n_1, n_2) - \hat{\boldsymbol{x}}\,(n_1, n_2)]^2} \tag{3.33}$$

We will compare the PSNR's between the resulting estimates for the contone image and the original contone image.

3.3.1 Restoration of Grayscale Images

In the first group of simulations, we use space-domain and frequency-domain projections. We use the simple Gaussian lowpass filter $g(n_1, n_2) = k\ e^{-\frac{n_1^2+n_2^2}{2\sigma^2}}$, for $-3 \leq n_1, n_2 \leq 3$, where k is a scaling factor used to make the DC gain of the filter unity. The σ^2 controls the bandwidth of the lowpass filter. Using a larger σ results in a more blurred image because the passband of the lowpass filter is narrow, while using a smaller σ results in a more grainy-looking image because the passband is wider. Therefore, we vary the σ value during the alternating projections. We start with a higher σ value and decrease it in the following set of iterations. We also use lowpass filters with passbands of $[-\pi/2,\ \pi/2]\times[-\pi/2,\ \pi/2]$, $[-2\pi/3,\ 2\pi/3]\times[-2\pi/3,\ 2\pi/3]$, or $[-3\pi/4,\ 3\pi/4]\times[-3\pi/4,\ 3\pi/4]$. The first estimate of the contone image, $\boldsymbol{x}_1$ is obtained by lowpass filtering the input halftone image, $\boldsymbol{x}_0$ with $g(n_1, n_2)$. Then we perform our spatial projection. After that, we again use lowpass filtering, and go on in an alternating fashion.

The original 512 × 512 8 bits/pixel Peppers image is shown in Figure 3.6. The Peppers image halftoned to 1 bit/pixel by error diffusion method is shown in Figure 3.7. The first estimate $\boldsymbol{x}_1$, which is the Gaussian filtered halftone image is shown in Figure 3.8. In large magnification, the halftoning patterns are observed, and the image quality is low. The results for successive projections are shown in Table 3.1. The first column shows iteration numbers by the type of projection. The PSNR between the halftoned 1 bit Peppers image and the original 8 bits Peppers image is 6.92 dB.

We stop the iterations when we can not obtain any further improvement in the PSNR value. The resulting PSNR value is 29.21 dB. Compared to lowpass filtering, 0.8 dB improvement is achieved after spatial projections. The resulting estimate image is given in Figure 3.9. The image quality is improved, and much of the halftoning noise existing in the first estimate is removed. A zoomed section from the dark gray pepper in the right is given for both the result of the first iteration and the result for the last iteration in Figure 3.10. The noise is removed as can be observed from this section of the peppers. Sequential Gaussian filtering, and lowpass filtering without any space-domain corrections can not achieve this PSNR value, and smooths out the image without retaining its detail information.

For the spatial projections, we make several iterations on the image successively. In other words, we perform a multi-pass spatial projection with varying relaxation parameters at each pass. The performance of the proposed POCS based inverse halftoning method is not very sensitive to the relaxation parameter λ, and the number of spatial projections. To verify this observation, we carried out simulations. In Table 3.2, we do two spatial projections instead of four as in Table 3.1, with varying relaxation parameters between 1 and 0.1. Resulting PSNR value of the restored image is 29.11 dB which is slightly less than the PSNR obtained in the previous simulation study. The restored image quality after three set of iterations is good and much of the halftoning noise is removed while the sharpness of the image is not affected.

We carried out another simulation study to check whether using relaxation parameter in the range $0 \leq \lambda \leq 2$ instead of $0 \leq \lambda \leq 1$ affects the results of the POCS method. The results are shown in Table 3.3 where the PSNR achieved is 29.19 dB after the third frequency projection. The image quality is similar to the ones obtained in the previous two simulations. Similar results can be obtained for other images as well. We conclude that the values of the relaxation parameter λ, and the number of spatial iterations can be chosen arbitrarily, and the specific choices do not constitute a problem for this method.

Similar simulations for the 512×512 1 bit/pixel error diffused Lena image is carried out, and the results are given Table 3.4, and Table 3.5, respectively. The PSNR between the halftoned 1 bit Lena image and the original 8 bits/pixel Lena image is 6.70 dB. The estimate after three set of iterations (after S3-2) has an improvement of 0.5 dB over the first estimate after the first frequency projection (after F1) in both simulations. The original Lena image is given in Figure 3.11, its halftoned version in Figure 3.12. The initial estimate, the final estimate having a PSNR of 31.17 dB in Table 3.5, and the estimate having a PSNR of 31.23 dB in Table 3.4 are given in Figure 3.13, Figure 3.14, and Figure 3.15, respectively. The resulting image is quite sharp, and visually pleasing. The details of the Lena image are retained while the halftoning noise is removed. This can be observed in the feathers around the hat, and the eye region. The zoomed sections from the shoulder region is given in Figure 3.16. The removal of the halftoning noise is again observed.

We compare our results with those in [36] where a similar POCS based inverse halftoning method is proposed assuming the error diffusion kernel is known. The PSNR comparisons are given in Table 3.6 for the Lena image, since only the PSNR values for Lena image are given in [36]. Their space-domain projection is different from ours. For the frequency-domain projection, they use SVD, or GLPF with a varying σ as the bandlimitation. The PSNR achieved by the proposed method is about 0.8 dB higher than the ones in [36].

Apart from the binary error diffusion coding, we carried out simulation studies for an image quantized to $K = 4$ levels, i.e. 2 bits instead of 1 bit, by error diffusion. The 2 bit error-diffused Peppers image is shown in Figure 3.17. The PSNR between the halftoned 2 bit Peppers image and the original 8 bits/pixel Peppers image is 18.18 dB. We use our method tailored for the multi-level case as explained in Section 3.2.1. When we start with a Gaussian lowpass filter with a narrow passband and then use a lowpass filter with a wider passband, and perform the spatial projections in between, the results are given in Table 3.7. The first estimate Peppers image, i.e. after Gaussian filtering, is shown in Figure 3.18. The final estimate obtained after two set of iterations is given Figure 3.19. The PSNR improvement is more than 1 dB with our POCS based method after two set of iterations.

Lena image error-diffused to 2 bits/pixel is shown in Figure 3.20. The PSNR between the halftoned 2 bit Lena image and the original 8 bits/pixel Lena image is 17.29 dB. Using our method for the multilevel error diffusion case, we obtain the results in Table 3.8. The Gaussian filtered version of the halftoned Lena image is shown in Figure 3.21, and the the result of the two set of iterations in Table 3.8 is shown in Figure 3.22. We want to emphasize the details around the feathers of the hat from the first estimate which is the Gaussian lowpass filtered version of the halftone image, and the estimate after two set of iterations. The latter is sharper than the former, and the details of feather are recovered more faithfully. Also, the eye region is a good example in recovery of the details from the original image by our spatial projection. The iris of the eye, and the eyelashes can be easily observed as result of our inverse halftoning method. Starting with a halfband filter, i.e. the passband PB=$[-\pi/2, \pi/2] \times [-\pi/2, \pi/2]$, we carrried out another simulation study which is shown in Table 3.9. The PSNR obtained in this case is 32.91 dB which is higher than the previous study. The final continuous tone image is shown in Figure 3.23. Without the smoothing effect of the Gaussian lowpass filtering, although this image has a higher PSNR value, it has some ringing artifacts which can be more easily observed in uniform intensity regions. However, as in the previous study, the quality of our restoration method can be verified by the recovery of the details around the feathers and the eye.

In the next group of simulation studies, we use wavelet-based space-scale domain projection in [37] as shown in Figure 3.5. The results are given in Table 3.10 for the Lena image. Even after a single set of iteration, that is by applying our space-domain projections following the wavelet-based projection in [37], our space-domain projections achieve more than 0.6 dB improvement. The resulting image is shown in Figure 3.24. We change relaxation parameter

λ to see whether we can get further improvement. Another set of relaxation parameters gives the results in Table 3.11. As can be observed, the result is approximately the same as the previous one.

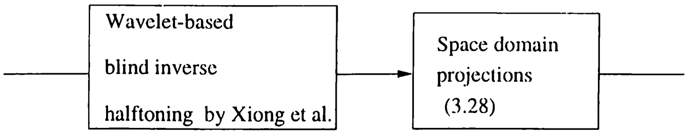

Figure 3.5: Inverse halftoning using the method in [37] with our method.

Similar results are obtained for the Peppers image where the PSNR values at each iteration are given in Table 3.12. The table shows that our proposed space-domain projection achieves 0.5 dB improvement after the space-scale projection. The resulting image after one set of iteration is given in Figure 3.26.

We also use frequency-domain projection together with space-scale domain projection and a set of space-domain projections as shown in Table 3.13. The resulting image shown in Figure 3.25 has a PSNR improvement of 0.7 dB.

Comparison of the POCS based method with other existing methods are given in Table 3.14 for the Lena and Peppers images. Method in [33] consists of spatial and frequency-domain projections as disccussed in Chapter 1. The method in [37] is the single space-scale projection as discussed in Section 3.2.3. Our method results in a higher PSNR than the other two methods in [33, 37] for both of the Lena and Peppers images.

We also test the performance of the proposed inverse halftoning method on images which are not error diffused by Floyd-Steinberg's method for which the spatial projection is developed. We do inverse halftoning on the images error diffused adaptively as described in Chapter 2. The simulation results are summarized in Table 3.15 for the Lena image which is error diffused by QR-RLS adaptation to binary form. The corresponding halftone image results in a visually pleasing binary image as shown in Figure 3.27. The initial estimate and the image with PSNR 30.79 dB restored by our POCS based inverse halftoning method are shown in Figure 3.28, and Figure 3.29, respectively. Although our spatial projection method is developed for inverse halftoning of images error diffused by Floyd-Steinberg's method, it provides improvement in the restoration of a contone image from an image error diffused adaptively.

3.3.2 Simulation Studies for Color Images

We also consider the restoration of halftoned color images. The spatial projection we present in Section 3.2.1 for the multilevel halftoning case is suitable for color images where each color pixel takes values from the color palette of limited size such as 8, 16, or more. By using the constraint in (3.20) for each color pixel, we find the two closest colors from the palette, i.e. the current color vector is between these two color vectors with the metric being the distance between the vectors. After that, we project each color vector to the closest color by simply scaling its each color component red, Green, and Blue. The original color Peppers image, and its halftoned version to 4 bits/pixel are shown in Figure 2.17 and Figure 2.19 respectively. The iterations are summarized in Table 3.16. We use both Gaussian lowpass filter and lowpass filters with passbands $[-\pi/2, \pi/2] \times [-\pi/2, \pi/2]$ and $[-3\pi/4, 3\pi/4] \times [-3\pi/4, 3\pi/4]$. The distances between the neighboring colors in the palette are very large since the palette contains only 16 color levels for thousands of colors existing in the original Peppers image. Therefore, the spatial projection after one pass does not make any improvement, and the number of corrected color pixels remains very low which does not contribute to the result. The image after the first iteration, and the final restored image are given in Figure 3.30, and Figure 3.31 respectively. The resulting image shows improvement with respect to the halftoned image. The continuous tones on the peppers are successfully restored, the color impulses are almost totally removed although the PSNR improvement seems very low. This is because the edge regions of the halftoned image are smeared to each other on both of the peppers in the front. These edges can not be restored as in the original image. The palette size of 16 is very low to allow faithful restoration of this image because the halftoned color image is disturbed very much in these edge regions. If the halftoning is done with more number of bits for each color pixel, this artifact would not be seen.

The same simulations are also done for the Minnesota color image whose original and halftoned version to 4 bits/pixel by error diffusion are shown in Figures 2.27 and 2.29 respectively. The iterations are given in Table 3.17. There is about 0.5 dB improvement on the average of PSNR's of each color component compared to the initial estimate. The image after the first iteration, and the final restored image are given in Figure 3.34, and Figure 3.35, respectively. The sky region is restored in a pleasing manner by providing the smooth transitions, and eliminating the color impulses. However, the small details of the buildings, and lights are not restored well.

As a second method to color image inverse halftoning, we do inverse halftoning only on the luminance component of the color image as discussed throughout this Chapter. Then the inverse halftoned image is obtained together with the lowpass filtered versions of the chrominance components. The color Peppers image after the first iteration, and the final restored image are given in Figure 3.32, and Figure 3.33, respectively. The iteration results are shown in Table 3.18. The chrominance components are lowpass filtered with a halfband lowpass filter. Similar to the results of the color inverse halftoning done on color components red, green, blue, the continuous tones are recovered, color impulses are eliminated although the PSNR improvement is negligible. The low PSNR is mostly due to the edge regions that can not be recovered as in the continuous tone original image. The restoration from only the luminance component does not give satisfactory results as it does in restoration of grayscale images. This result is expected since forward color error diffusion is performed simultaneously with red, green, and blue color components of the image. Particularly, the quantization operation in error diffusion system is performed in RGB color space, rather than the color space with one luminance component and two chrominance components.

The results of the same simulations for color inverse halftoning with restoring the luminance component for the Minnesota image is given in Table 3.19. Images obtained after the first set of iteration and the final iteration are shown in Figure 3.36, and Figure 3.37 respectively. Similarly, the smooth transitions in the sky are restored whereas some details are lost.

We can not compare our results for the inverse halftoning of color images with any other method, because such a study for color images does not exist in the literature.

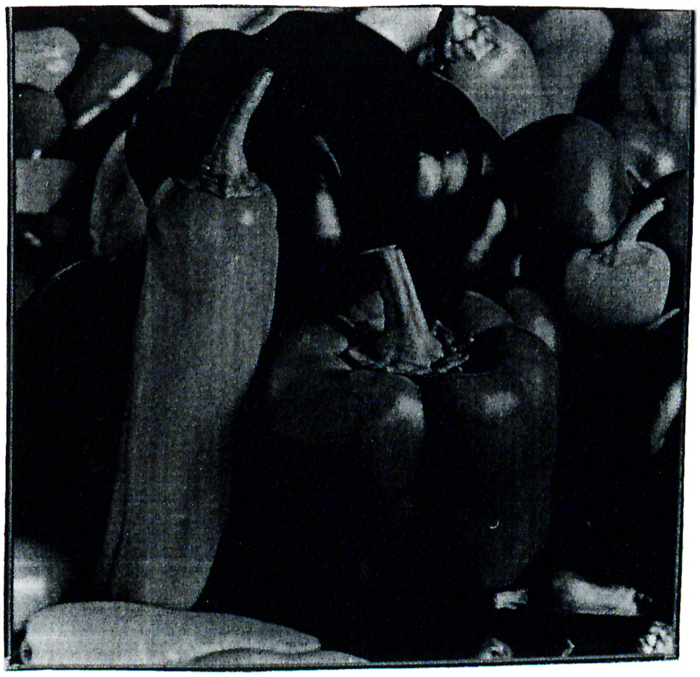

Figure 3.6: Original Peppers Image.

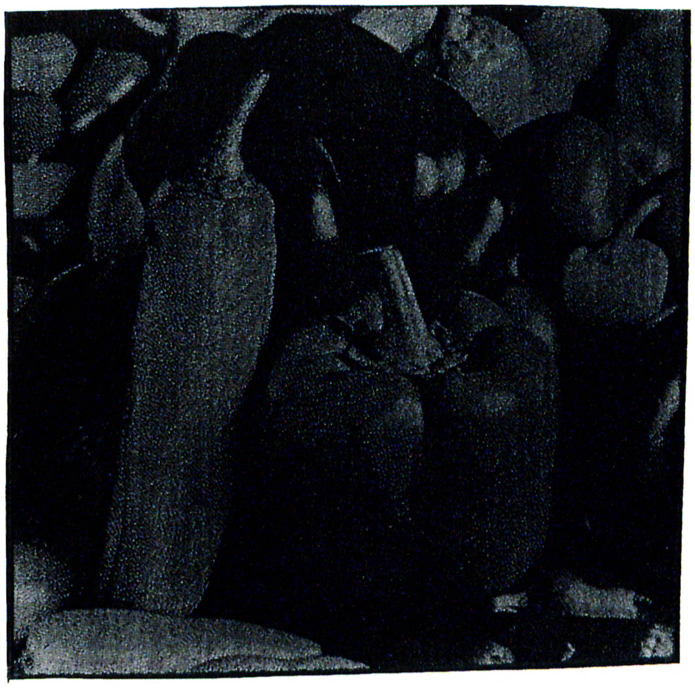

Figure 3.7: Peppers Image error diffused to 1 bit/pixel by Floyd-Steingberg's Method.

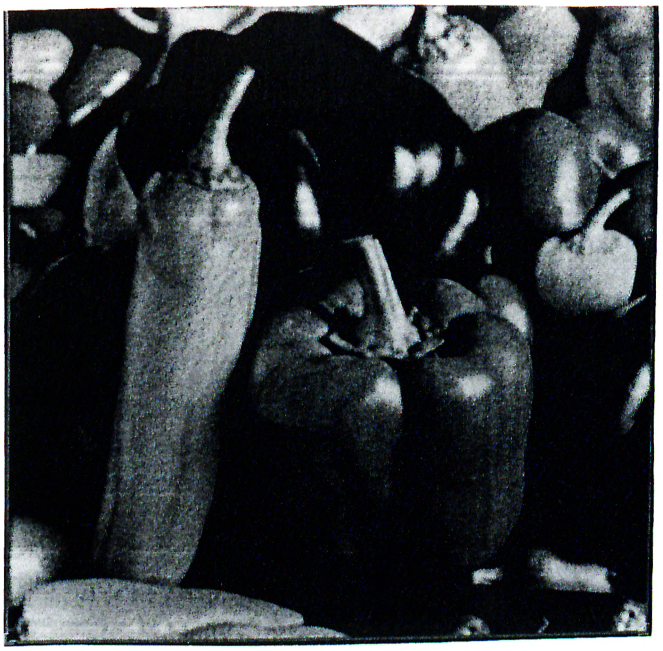

Figure 3.8: Result of the first iteration in Table 3.1.

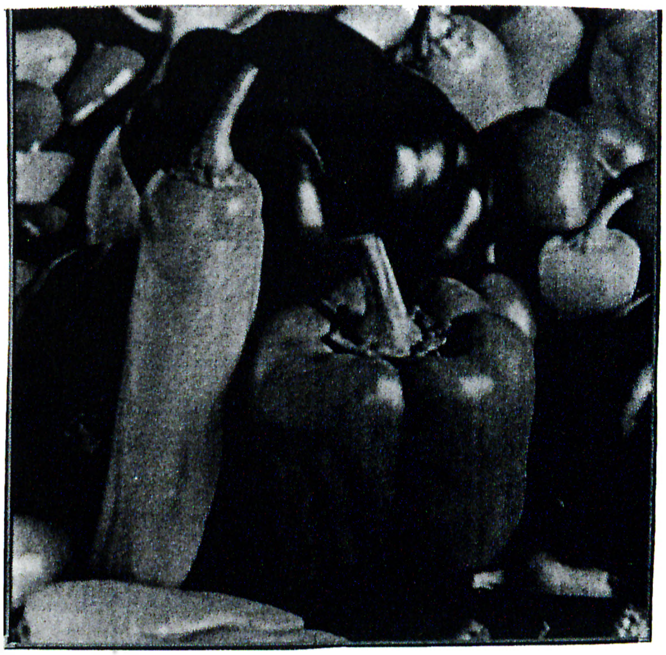

Figure 3.9: Result of three set of iterations in Table 3.1.

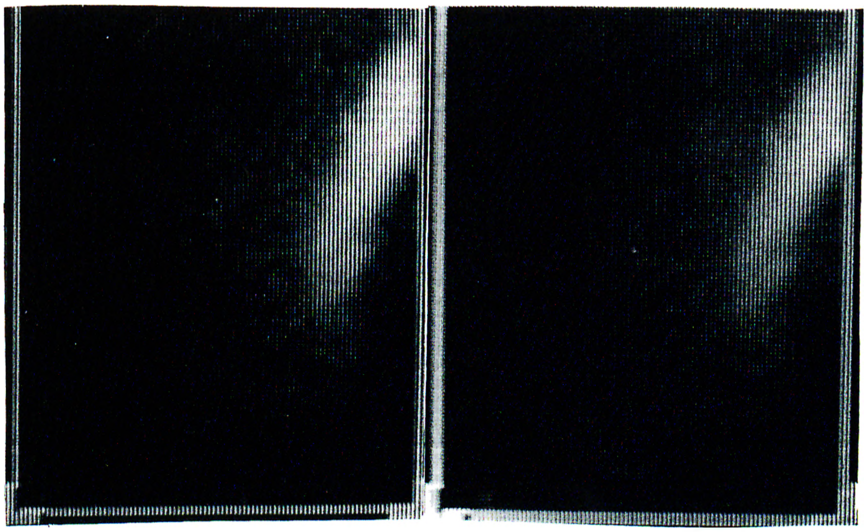

Figure 3.10: Zoomed sections from the first and last estimates in Table 3.1.

Iteration	Type	PSNR
F1	GLPF ($\sigma^2 = 1.5$)	28.47
S1-1	Spatial ($\lambda = 1$)	28.25
S1-2	Spatial ($\lambda = 0.5$)	28.78
S1-3	Spatial ($\lambda = 0.1$)	28.59
S1-4	Spatial ($\lambda = 1$)	28.86
F2	GLPF ($\sigma^2 = 0.5$)	28.75
S2-1	Spatial ($\lambda = 1$)	28.72
S2-2	Spatial ($\lambda = 0.5$)	28.98
S2-3	Spatial ($\lambda = 0.1$)	28.90
S2-4	Spatial ($\lambda = 1$)	29.06
F3	LPF (PB=$3\pi/4$)	29.16
S3-1	Spatial ($\lambda = 1$)	28.74
S3-2	Spatial ($\lambda = 0.5$)	29.21
S3-3	Spatial ($\lambda = 0.1$)	28.93
S3-4	Spatial ($\lambda = 1$)	29.21

Table 3.1: The PSNR values after each iteration for the halftoned 1 bit Peppers image. F (S) letter in the first column corresponds to the Frequency (Space) projection. (e.g. S1-2 means 2^{nd} iteration in the 1^{st} spatial projection) Type denotes the type of the projection.

Iteration	Type	PSNR
F1	GLPF ($\sigma^2 = 1.5$)	28.47
S1-1	Spatial ($\lambda = 1$)	28.25
S1-2	Spatial ($\lambda = 0.5$)	28.78
F2	GLPF ($\sigma^2 = 0.5$)	28.66
S2-1	Spatial ($\lambda = 1$)	28.52
S2-2	Spatial ($\lambda = 0.5$)	28.93
F3	LPF (PB=$3\pi/4$)	28.97
S3-1	Spatial ($\lambda = 1$)	28.45
S3-2	Spatial ($\lambda = 0.5$)	29.11

Table 3.2: The PSNR values after each iteration for the halftoned 1 bit Peppers image. F (S) letter in the first column corresponds to the Frequency (Space) projection. (e.g. S1-2 means 2^{nd} iteration in the 1^{st} spatial projection) Type denotes the type of the projection.

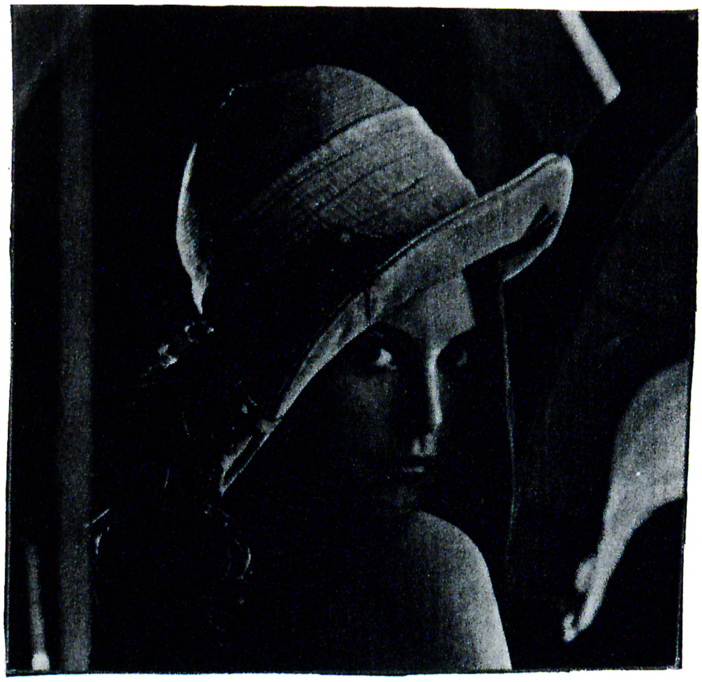

Figure 3.11: Original Lena Image.

Iteration	Type	PSNR
F1	GLPF ($\sigma^2 = 1.5$)	28.47
S1-1	Spatial ($\lambda = 2$)	28.25
S1-2	Spatial ($\lambda = 1$)	28.80
S1-3	Spatial ($\lambda = 0.5$)	28.54
S1-4	Spatial ($\lambda = 1.5$)	28.88
F2	GLPF ($\sigma^2 = 0.5$)	28.85
S2-1	Spatial ($\lambda = 2$)	28.70
S2-2	Spatial ($\lambda = 1$)	29.05
S2-3	Spatial ($\lambda = 0.5$)	28.86
S2-4	Spatial ($\lambda = 1.5$)	29.10
F3	LPF (PB=$3\pi/4$)	29.19
S3-1	Spatial ($\lambda = 2$)	28.62
S3-2	Spatial ($\lambda = 1$)	29.17
S3-3	Spatial ($\lambda = 0.5$)	28.70
S3-4	Spatial ($\lambda = 1.5$)	29.13

Table 3.3: The PSNR values after each iteration for the halftoned 1 bit Peppers image. F (S) letter in the first column corresponds to the Frequency (Space) projection. (e.g. S1-2 means 2^{nd} iteration in the 1^{st} spatial projection) Type denotes the type of the projection.

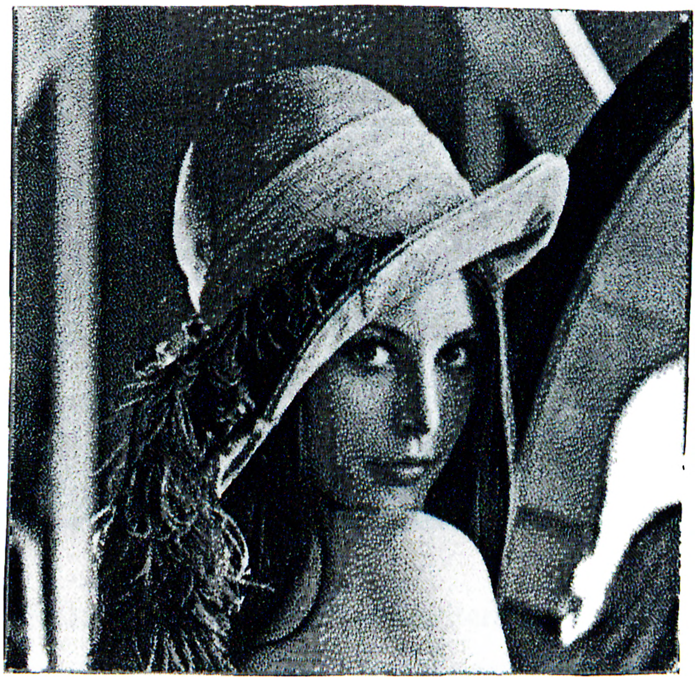

Figure 3.12: Lena Image error diffused to 1 bit/pixel by Floyd-Steingberg's Method.

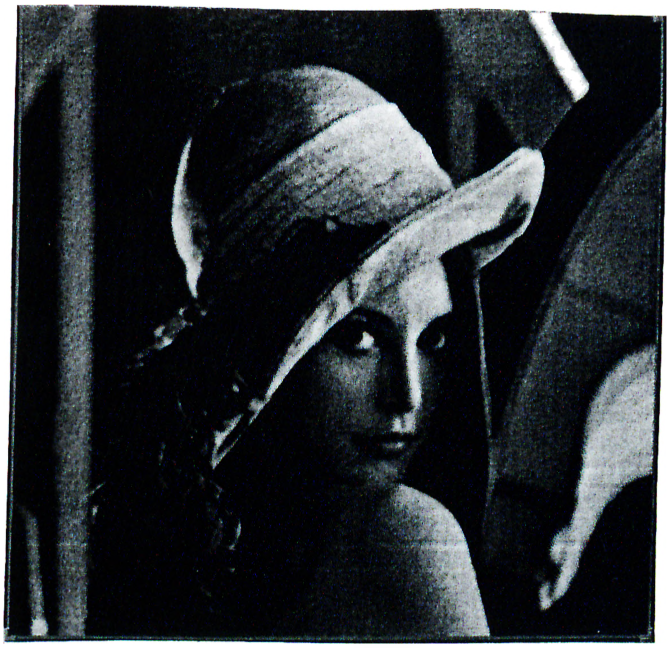

Figure 3.13: Result of the first iteration in Table 3.4.

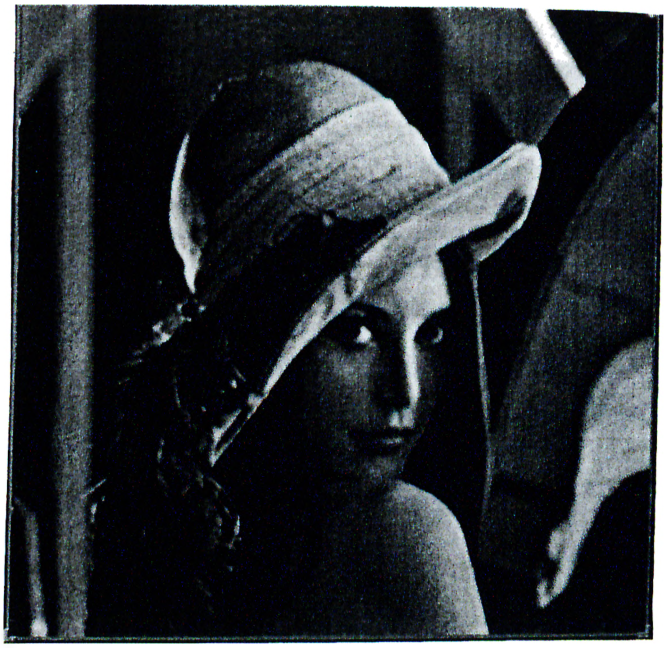

Figure 3.14: Result of three set of iterations in Table 3.4.

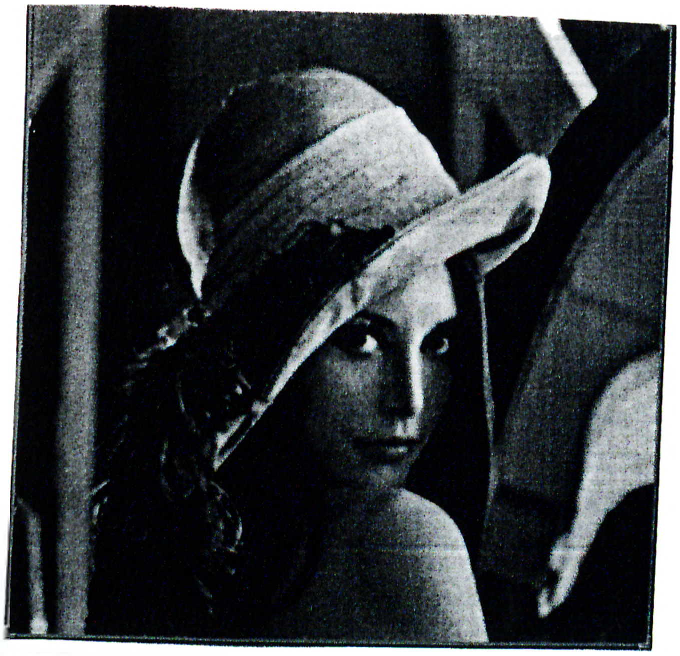

Figure 3.15: Result of three set of iterations in Table 3.5.

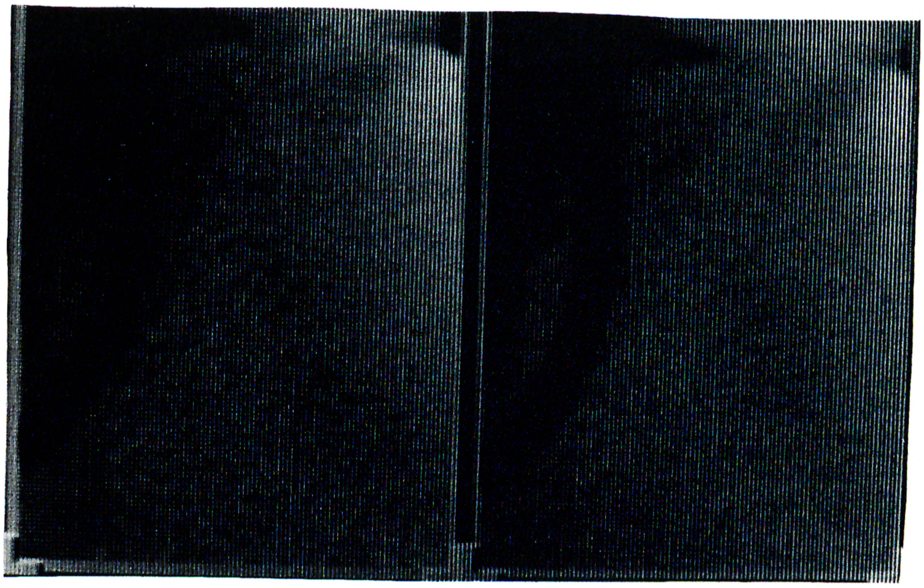

Figure 3.16: Zoomed sections from the first and last estimates in Table 3.4.

Iteration	Type	PSNR
F1	GLPF ($\sigma^2 = 1.5$)	30.71
S1-1	Spatial ($\lambda = 1$)	30.34
S1-2	Spatial ($\lambda = 0.5$)	30.99
S1-3	Spatial ($\lambda = 0.1$)	30.64
S1-4	Spatial ($\lambda = 1$)	31.02
F2	GLPF ($\sigma^2 = 0.5$)	30.79
S2-1	Spatial ($\lambda = 1$)	30.72
S2-2	Spatial ($\lambda = 0.5$)	31.05
S2-3	Spatial ($\lambda = 0.1$)	30.87
S2-4	Spatial ($\lambda = 1$)	31.08
F3	LPF (PB=$3\pi/4$)	31.21
S3-1	Spatial ($\lambda = 1$)	30.59
S3-2	Spatial ($\lambda = 0.5$)	31.23
S3-3	Spatial ($\lambda = 0.1$)	30.82
S3-4	Spatial ($\lambda = 1$)	31.17

Table 3.4: The PSNR values after each iteration for the halftoned 1 bit Lena image. F (S) letter in the first column corresponds to the Frequency (Space) projection. (e.g. S1-2 means 2^{nd} iteration in the 1^{st} spatial projection) Type denotes the type of the projection.

Iteration	Type	PSNR
F1	GLPF ($\sigma^2 = 1.5$)	30.71
S1-1	Spatial ($\lambda = 1$)	30.34
S1-2	Spatial ($\lambda = 0.5$)	30.99
F2	GLPF ($\sigma^2 = 0.5$)	30.70
S2-1	Spatial($\lambda = 1$)	30.47
S2-2	Spatial ($\lambda = 0.5$)	31.04
F3	LPF (PB=$3\pi/4$)	31.03
S3-1	Spatial ($\lambda = 1$)	30.27
S3-2	Spatial ($\lambda = 0.5$)	31.17

Table 3.5: The PSNR values after each iteration for the halftoned 1 bit Lena image. F (S) letter in the first column corresponds to the Frequency (Space) projection. (e.g. S1-2 means 2^{nd} iteration in the 1^{st} spatial projection) Type denotes the type of the projection.

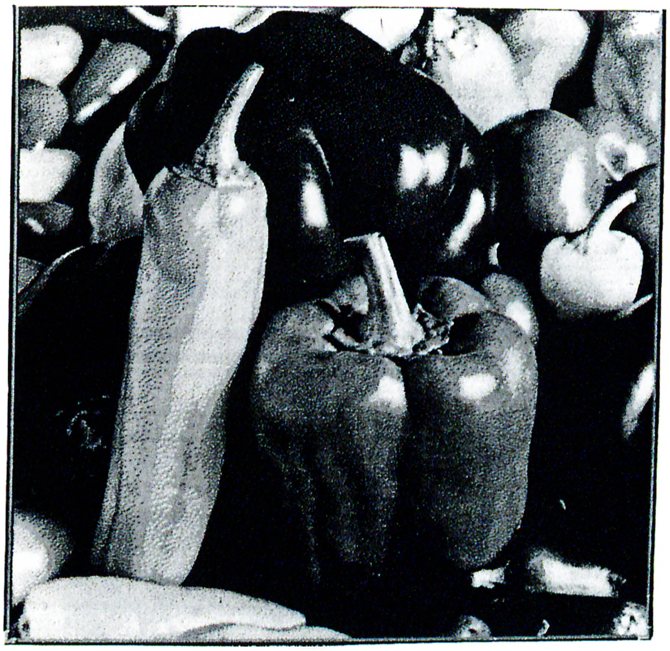

Figure 3.17: Peppers Image error diffused to 2 bits/pixel by Floyd-Steingberg's Method.

Method in [36] (GLPF)	Method in [36] (SVD)	Proposed Method (GLPF, LPF)
29.4	30.4	31.23

Table 3.6: Comparison of inverse halftoning methods in [36], and our method for the Lena Image. The (GLPF, LPF, SVD) denotes the type of frequency-domain projection

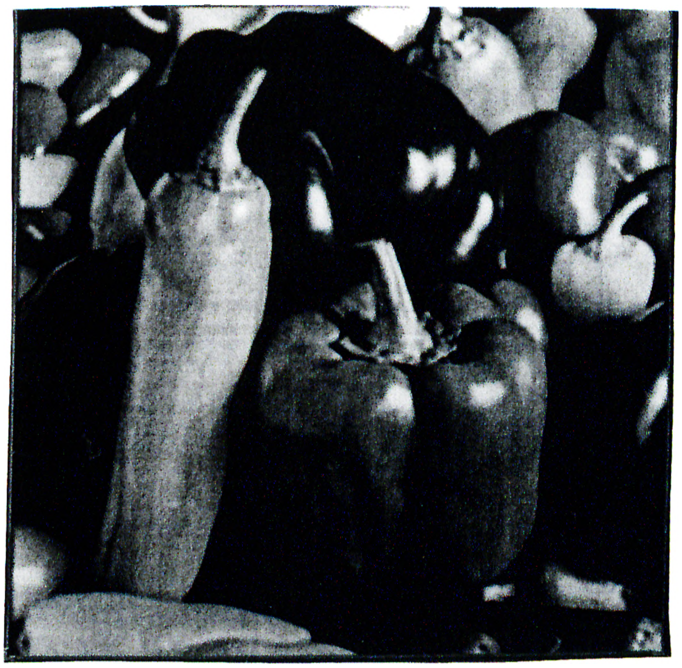

Figure 3.18: Result of the first iteration in Table 3.7.

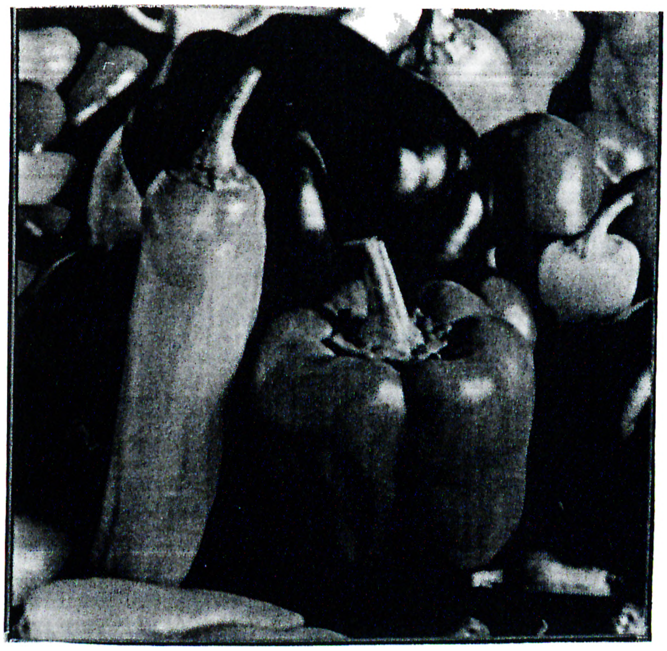

Figure 3.19: Result of two set of iterations in Table 3.7.

Iteration	Type	PSNR
F1	GLPF ($\sigma^2 = 1.5$)	30.39
S1-1	Spatial ($\lambda = 1$)	30.23
S1-2	Spatial ($\lambda = 0.5$)	31.03
S1-3	Spatial ($\lambda = 0.1$)	30.70
S1-4	Spatial $\lambda = 1$)	31.24
F2	LPF(PB=$3\pi/4$)	31.26
S2-1	Spatial($\lambda = 1$)	30.54
S2-2	Spatial ($\lambda = 0.5$)	31.38
S2-3	Spatial ($\lambda = 0.1$)	30.88
S2-4	Spatial ($\lambda = 1$)	31.42

Table 3.7: The PSNR values after each iteration for the halftoned 2 bit Peppers image. F (S) letter in the first column corresponds to the Frequency (Space) projection. (e.g. S1-2 means 2^{nd} iteration in the 1^{st} spatial projection) Type denotes the type of the projection.

Iteration	Type	PSNR
F1	GLPF ($\sigma^2 = 1.5$)	31.27
S1-1	Spatial ($\lambda = 1$)	31.13
S1-2	Spatial ($\lambda = 0.5$)	32.02
S1-3	Spatial ($\lambda = 0.1$)	31.53
S1-4	Spatial $\lambda = 1$)	32.23
F2	LPF(PB=$3\pi/4$)	32.25
S2-1	Spatial($\lambda = 1$)	31.30
S2-2	Spatial ($\lambda = 0.5$)	32.44
S2-3	Spatial ($\lambda = 0.1$)	31.67
S2-4	Spatial ($\lambda = 1$)	32.51

Table 3.8: The PSNR values after each iteration for the halftoned 2 bit Lena image. F (S) letter in the first column corresponds to the Frequency (Space) projection. (e.g. S1-2 means 2^{nd} iteration in the 1^{st} spatial projection) Type denotes the type of the projection.

Iteration	Type	PSNR
F1	LPF (PB=$\pi/2$)	32.64
S1-1	Spatial ($\lambda = 1$)	32.15
S1-2	Spatial ($\lambda = 0.5$)	32.64
F2	LPF(PB:$3\pi/4$)	32.70
S2-1	Spatial($\lambda = 1$)	31.67
S2-2	Spatial ($\lambda = 0.5$)	32.73
F3	GLPF ($\sigma^2 = 0.25$)	32.87
S3-1	Spatial($\lambda = 1$)	31.98
S3-2	Spatial ($\lambda = 0.5$)	32.91

Table 3.9: The PSNR values after each iteration for the halftoned 2 bit Lena image. F (S) letter in the first column corresponds to the Frequency (Space) projection. (e.g. S1-2 means 2^{nd} iteration in the 1^{st} spatial projection) Type denotes the type of the projection.

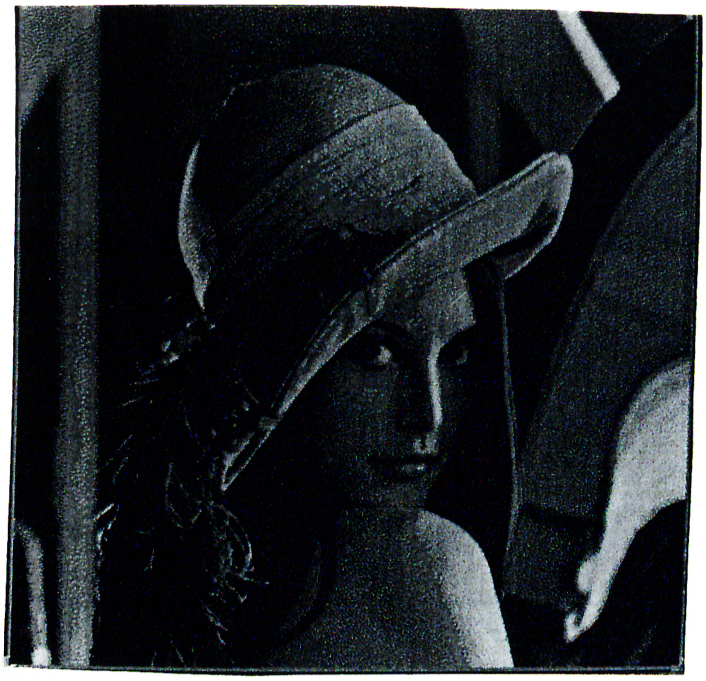

Figure 3.20: Lena Image error diffused to 2 bits/pixel by Floyd-Steingberg's Method.

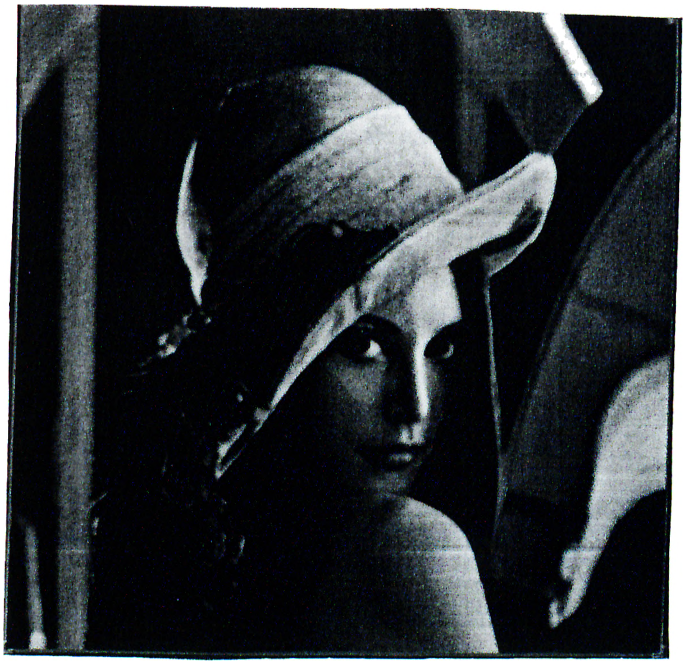

Figure 3.21: Result of the first iteration in Table 3.8.

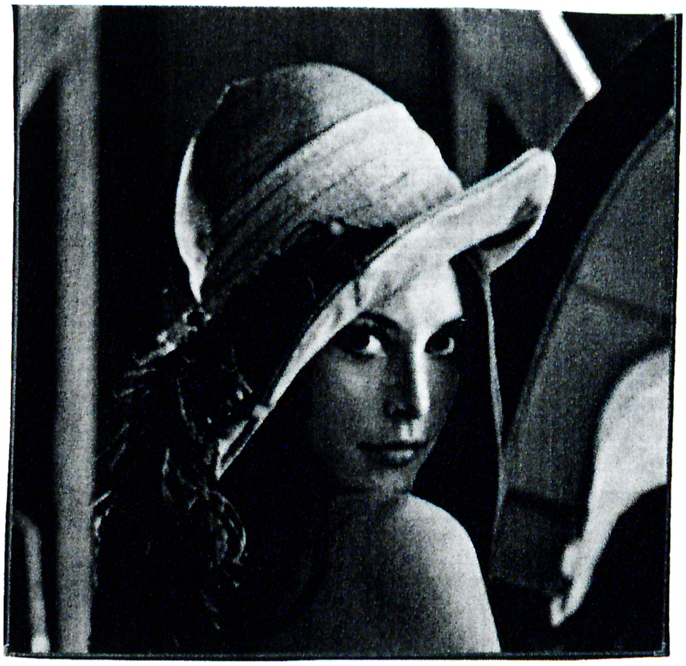

Figure 3.22: Result of two set of iterations in Table 3.8.

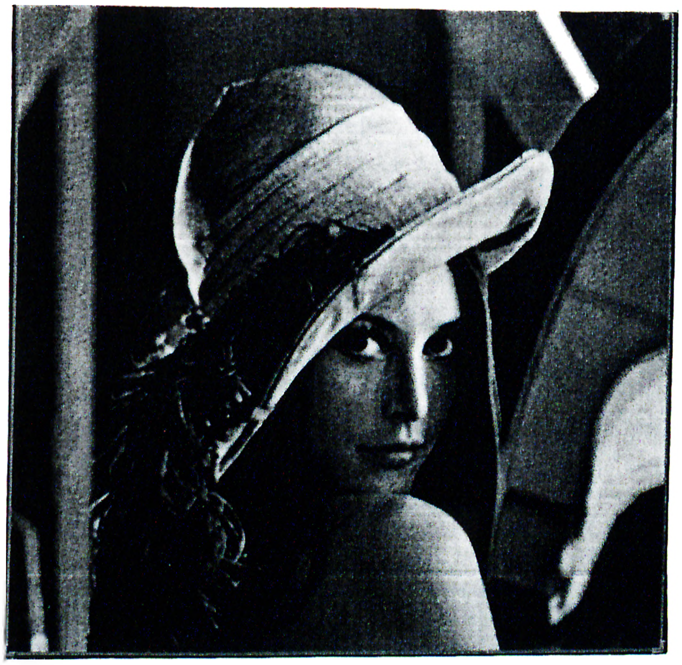

Figure 3.23: Result of three set of iterations in Table 3.9.

Iteration	Type	PSNR
SS-1	Wavelet	31.47
S1-1	Spatial ($\lambda = 1$)	30.36
S1-2	Spatial ($\lambda = 0.5$)	31.90
S1-3	Spatial ($\lambda = 0.1$)	31.02
S1-4	Spatial ($\lambda = 1$)	32.11

Table 3.10: The PSNR values after each iteration for the Lena image. SS (S) letter in the first column corresponds to the Space-Scale (Space) projection. (e.g. S1-2 means 2^{nd} iteration in the 1^{st} spatial projection) Type denotes the type of the projection.

Iteration	Type	PSNR
SS-1	Wavelet	31.47
S1-1	Spatial ($\lambda = 1$)	30.36
S1-2	Spatial ($\lambda = 0.5$)	31.90
S1-3	Spatial ($\lambda = 0.4$)	30.77
S1-4	Spatial ($\lambda = 0.1$)	32.09

Table 3.11: The PSNR values after each iteration for the Lena image. SS (S) letter in the first column corresponds to the Space-Scale (Space) projection. (e.g. S1-2 means 2^{nd} iteration in the 1^{st} spatial projection) Type denotes the type of the projection.

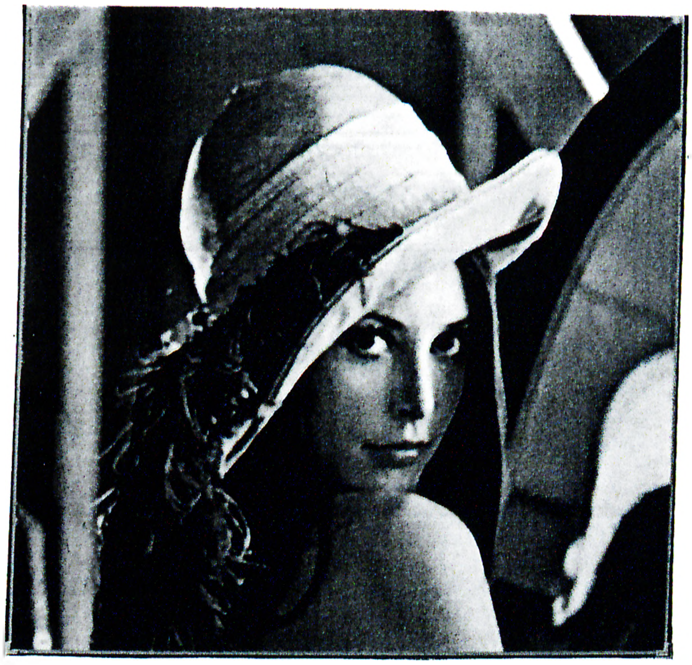

Figure 3.24: Result of the one set of iteration in Table 3.10.

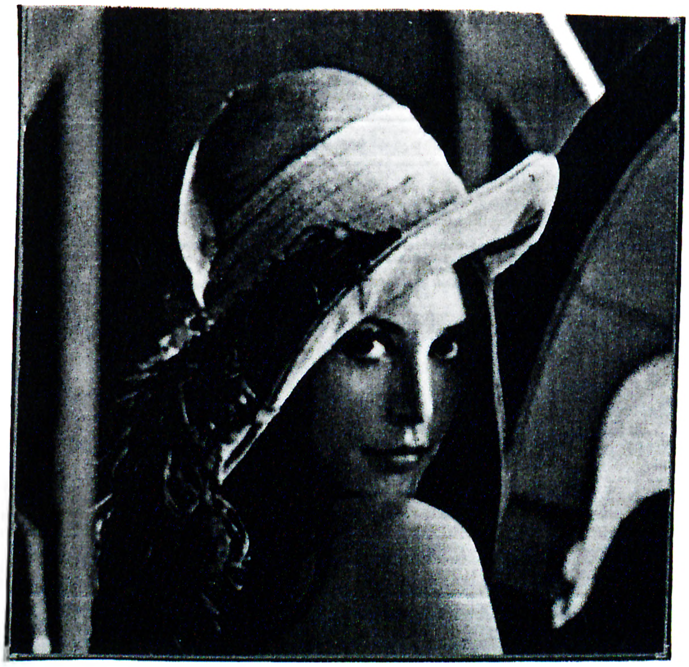

Figure 3.25: Result of the two sets of iterations in Table. 3.13.

Iteration	Type	PSNR
SS-1	Wavelet	30.40
S1-1	Spatial ($\lambda = 1$)	29.46
S1-2	Spatial ($\lambda = 0.5$)	30.76
S1-3	Spatial ($\lambda = 0.1$)	30.07
S1-4	Spatial ($\lambda = 1$)	30.90

Table 3.12: The PSNR values after each iteration for the Peppers image. SS (S) letter in the first column corresponds to the Space-Scale (Space) projection. (e.g. S1-2 means 2^{nd} iteration in the 1^{st} spatial projection) Type denotes the type of the projection.

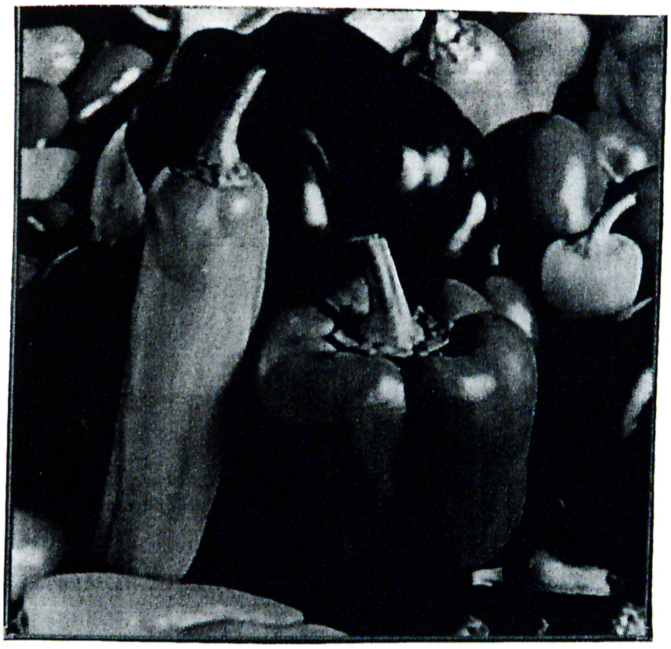

Figure 3.26: Result of the one set of iteration in Table 3.12.

Iteration	Type	PSNR
SS-1	Wavelet	31.47
S1-1	Spatial ($\lambda = 1$)	30.36
S1-2	Spatial ($\lambda = 0.5$)	31.90
S1-3	Spatial ($\lambda = 0.4$)	30.77
S1-4	Spatial ($\lambda = 0.1$)	32.10
F1	GLPF ($\sigma^2 = 0.25$)	32.09
S2-1	Spatial ($\lambda = 1$)	31.25
S2-2	Spatial ($\lambda = 0.5$)	32.17

Table 3.13: The PSNR values after each iteration for the Lena image. SS (S) letter in the first column corresponds to the Space-Scale (Space) projection. (e.g. S1-2 means 2^{nd} iteration in the 1^{st} spatial projection) Type denotes the type of the projection.

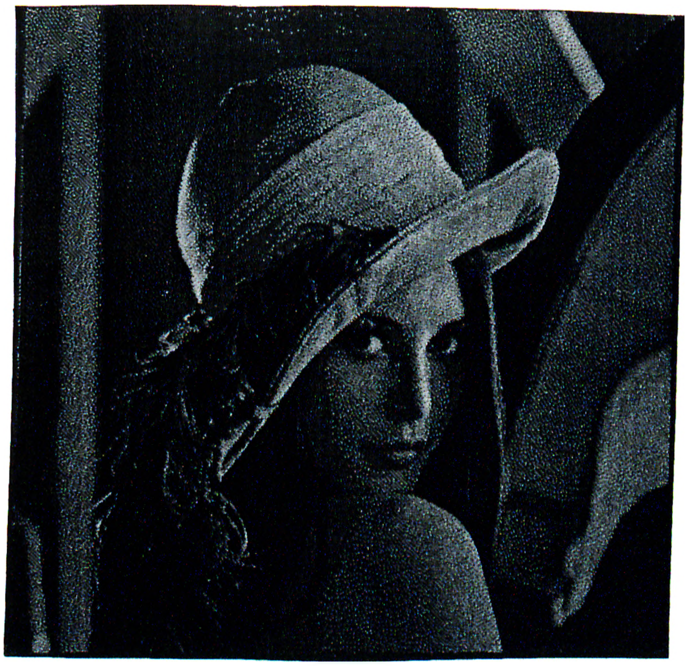

Figure 3.27: Lena Image error diffused to 1 bit/pixel by QR-RLS adaptation.

	Method in [33]	Method in [37]	Proposed Method
Lena (PSNR)	32.00	31.67	32.17
Peppers (PSNR)	30.30	30.69	30.90

Table 3.14: Comparison of inverse halftoning methods. All methods assume the error diffusion kernel is known.

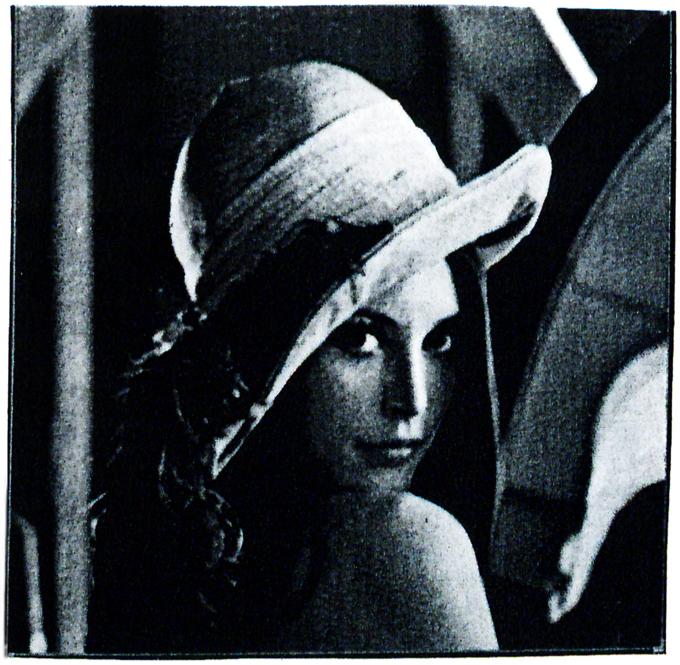

Figure 3.28: Result of the first iteration in Table 3.15.

Iteration	Type	PSNR
F1	GLPF ($\sigma^2 = 1.5$)	30.44
S1-1	Spatial ($\lambda = 1$)	29.88
S1-2	Spatial ($\lambda = 0.5$)	30.51
S1-3	Spatial ($\lambda = 0.1$)	30.26
S1-4	Spatial ($\lambda = 1$)	30.56
F2	GLPF ($\sigma^2 = 0.5$)	30.46
S2-1	Spatial ($\lambda = 1$)	30.34
S2-2	Spatial ($\lambda = 0.5$)	30.63
S2-3	Spatial ($\lambda = 0.1$)	30.47
S2-4	Spatial ($\lambda = 1$)	30.62
F3	LPF (PB=$2\pi/3$)	30.21
S3-1	Spatial ($\lambda = 1$)	30.79
S3-2	Spatial ($\lambda = 0.5$)	30.47
S3-3	Spatial ($\lambda = 0.1$)	30.67
S3-4	Spatial ($\lambda = 1$)	30.55

Table 3.15: The PSNR values after each iteration for the Lena image error diffused with QR-RLS adaptation to 1 bit/pixel. F (S) letter in the first column corresponds to the Frequency (Space) projection. (e.g. S1-2 means 2^{nd} iteration in the 1^{st} spatial projection) Type denotes the type of the projection.

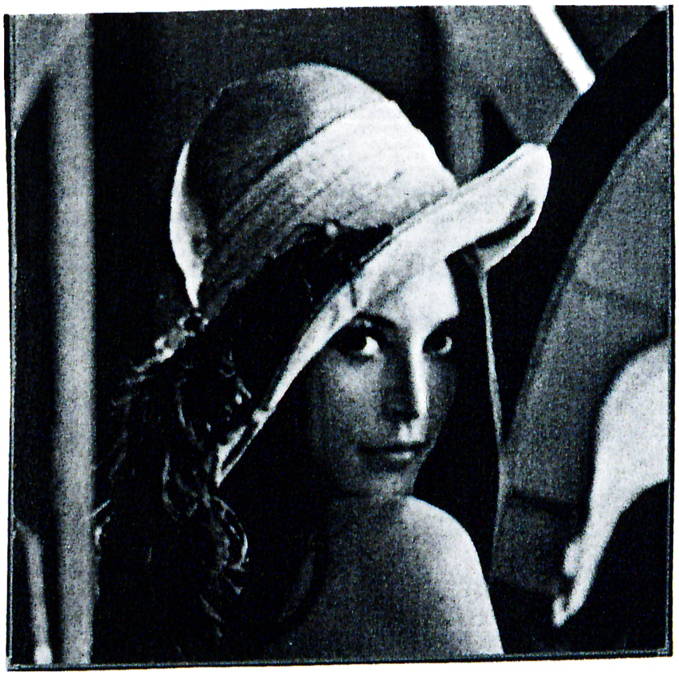

Figure 3.29: Result of three set of iterations in Table 3.15.

Iteration	Type	PSNR (Red)	PSNR (Green)	PSNR (Blue)
F1	LPF (PB=$\pi/2$)	20.70	21.90	24.68
S1-1	Spatial ($\lambda = 1$)	20.57	21.78	24.52
S1-2	Spatial ($\lambda = 0.5$)	20.57	21.78	24.52
F2	GLPF($\sigma^2 = 0.5$)	20.83	22.01	24.97
S2-1	Spatial($\lambda = 1$)	20.82	22.01	24.94
S2-2	Spatial ($\lambda = 0.5$)	20.81	22.01	24.92
F3	LPF (PB=$3\pi/4$)	20.78	21.99	24.99
S3-1	Spatial($\lambda = 1$)	20.43	21.69	24.43
S3-2	Spatial ($\lambda = 0.5$)	20.43	21.69	24.43

Table 3.16: The PSNR values after each iteration for the color Peppers image error diffused to 4 bits/pixel. F (S) letter in the first column corresponds to the Frequency (Space) projection. (e.g. S1-2 means 2nd iteration in the 1st spatial projection) Type denotes the type of the projection.

Iteration	Type	PSNR (Red)	PSNR (Green)	PSNR (Blue)
F1	LPF (PB=$\pi/2$)	19.53	20.03	20.51
S1-1	Spatial ($\lambda = 1$)	19.82	20.50	20.87
S1-2	Spatial ($\lambda = 0.5$)	19.82	20.50	20.87
F2	GLPF($\sigma^2 = 0.5$)	19.99	20.47	20.86
S2-1	Spatial($\lambda = 1$)	19.97	20.52	20.90
S2-2	Spatial ($\lambda = 0.5$)	19.96	20.52	20.90

Table 3.17: The PSNR values after each iteration for the color Minnesota image error diffused to 4 bits/pixel. F (S) letter in the first column corresponds to the Frequency (Space) projection. (e.g. S1-2 means 2nd iteration in the 1st spatial projection) Type denotes the type of the projection.

Iteration	Type	PSNR (Y)
F1	LPF (PB=$\pi/2$)	23.95
S1-1	Spatial ($\lambda = 1$)	23.89
S1-2	Spatial ($\lambda = 0.5$)	23.86
F2	GLPF($\sigma^2 = 0.5$)	23.99
S2-1	Spatial($\lambda = 1$)	23.94
S2-2	Spatial ($\lambda = 0.5$)	23.92
F3	LPF (PB:$3\pi/4$)	23.94

Table 3.18: The PSNR values after each iteration for the luminance component (Y) of the color Peppers image halftoned to 4 bits/pixel. F (S) letter in the first column corresponds to the Frequency (Space) projection. (e.g. S1-2 means 2^{nd} iteration in the 1^{st} spatial projection) Type denotes the type of the projection.

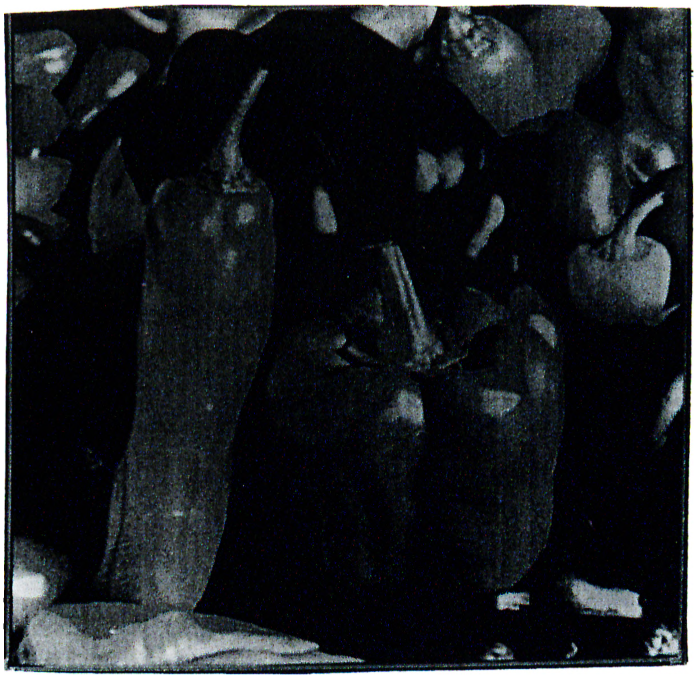

Figure 3.30: Result of the first iteration in Table 3.16.

Iteration	Type	PSNR (Y)
F1	LPF (PB=$\pi/2$)	20.14
S1-1	Spatial ($\lambda = 1$)	20.11
S1-2	Spatial ($\lambda = 0.5$)	20.06
F2	GLPF($\sigma^2 = 0.5$)	20.17
S2-1	Spatial($\lambda = 1$)	20.18
S2-2	Spatial ($\lambda = 0.5$)	20.15
F3	LPF (PB:$3\pi/4$)	20.16

Table 3.19: The PSNR values after each iteration for the luminance component (Y) of the color Minnesota image error diffused to 4 bits/pixel. F (S) letter in the first column corresponds to the Frequency (Space) projection. (e.g. S1-2 means 2^{nd} iteration in the 1^{st} spatial projection) Type denotes the type of the projection.

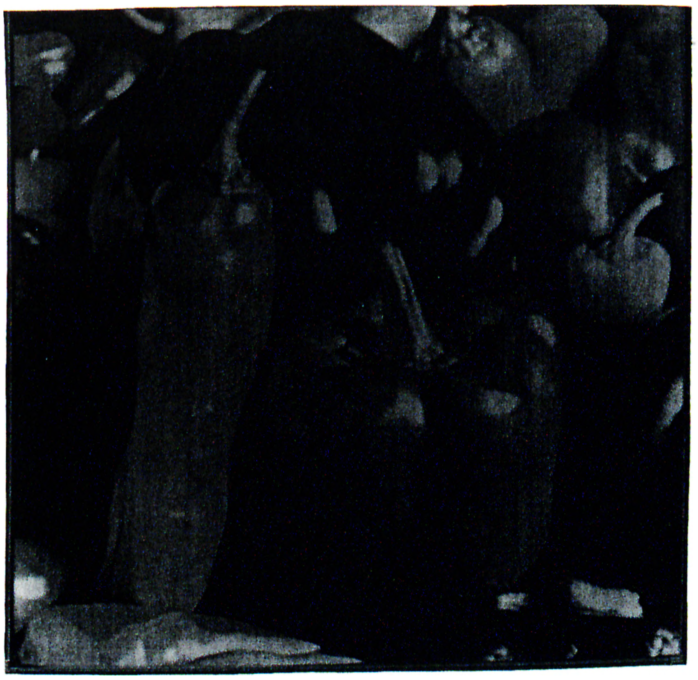

Figure 3.31: Result of two set of iterations in Table 3.16.

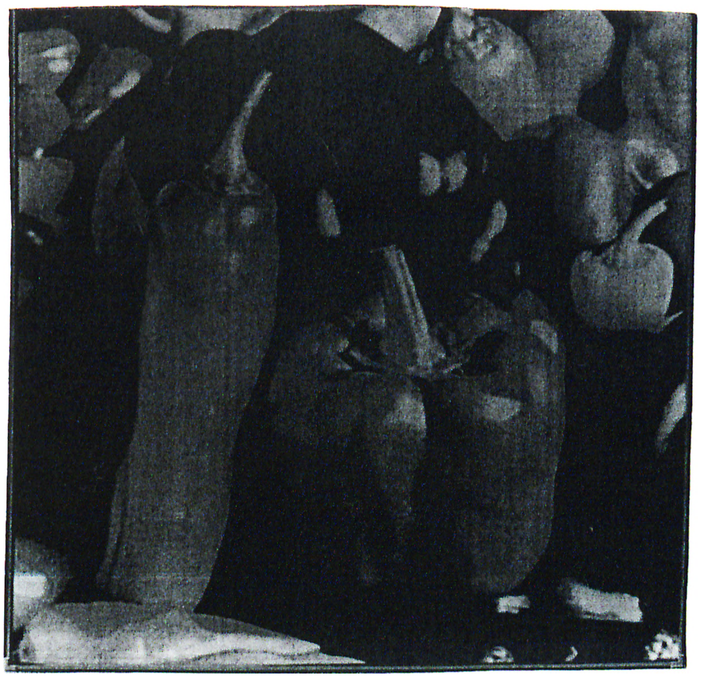

Figure 3.32: Result of the first iteration in Table 3.18.

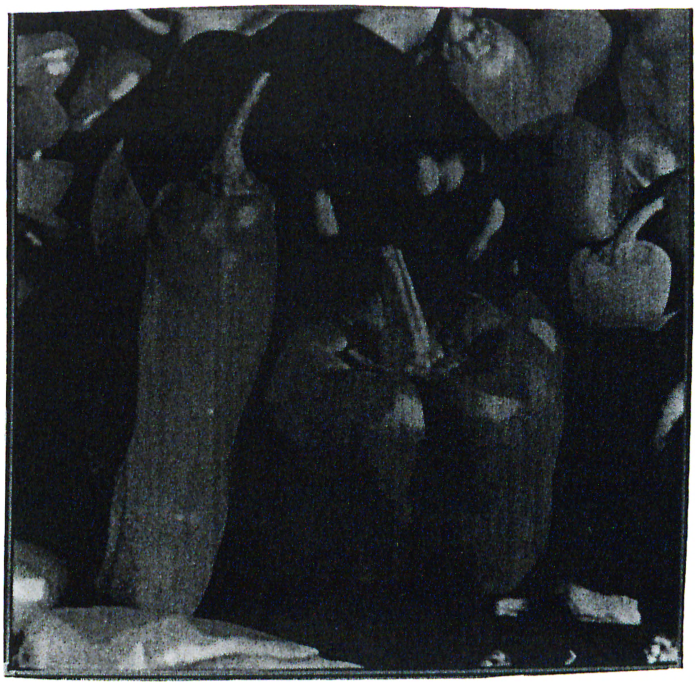

Figure 3.33: Result of two set of iterations in Table 3.18.

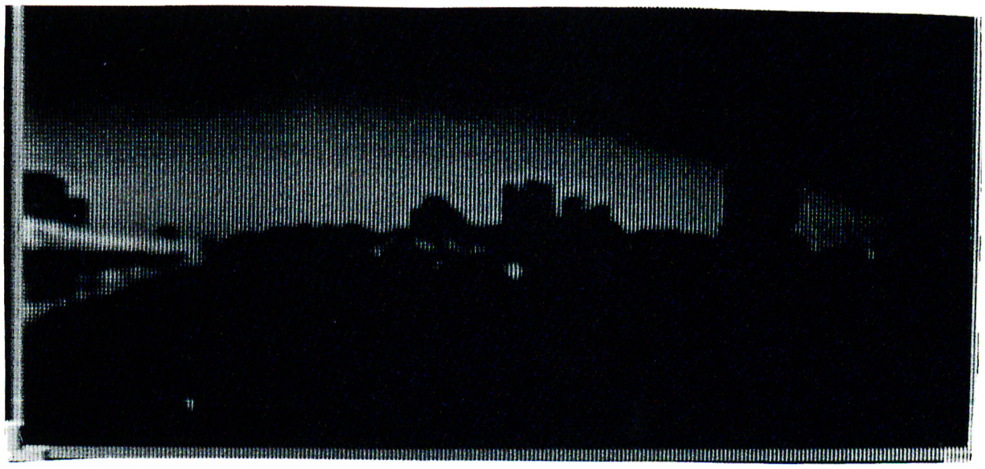

Figure 3.34: Result of the first iteration in Table 3.17.

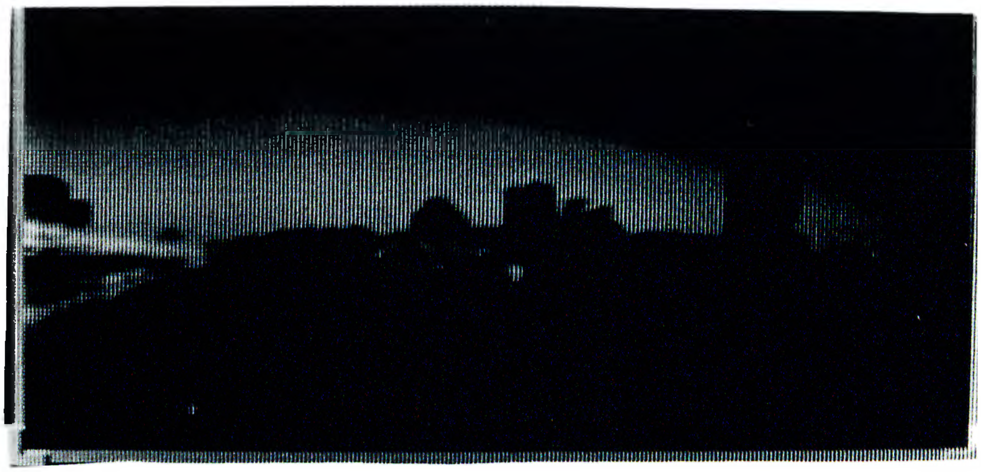

Figure 3.35: Result of two set of iterations in Table 3.17.

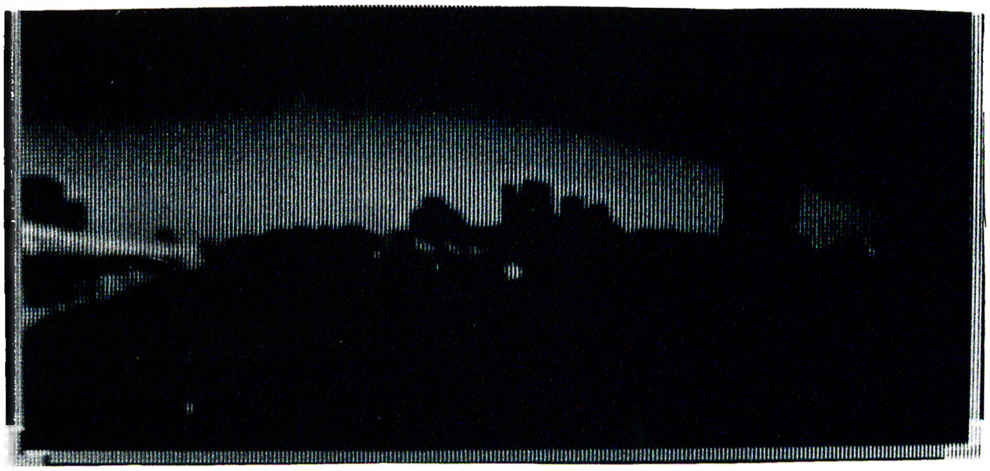

Figure 3.36: Result of the first set of iteration in Table 3.19.

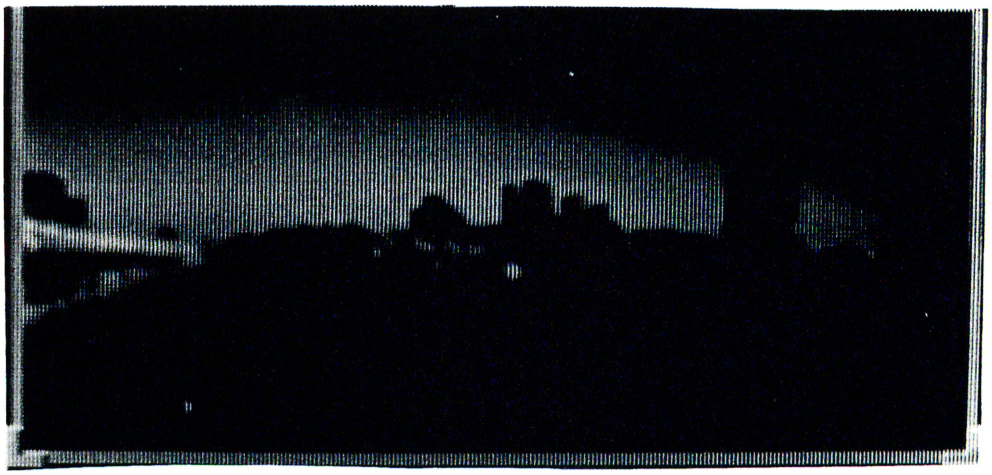

Figure 3.37: Result of two set of iterations in Table 3.19.

Chapter 4

CONCLUSIONS AND FUTURE WORK

In this thesis, novel methods for halftoning of color images, and inverse halftoning of both grayscale and color images are presented.

In the first part of the thesis, a new adaptive error diffusion method for color images is introduced. Representing a natural image which contains thousands or millions of colors on a printing or a display device that allows only a limited number of bits for each pixel, causes a large reduction in the number of colors of images. This reduction results into a highly degraded image quality when direct quantization is used. As a solution to this problem, error diffusion method is widely used. The proposed adaptive error diffusion method employs a rotation based RLS adaptation for the prediction problem in the update of the error diffusion filter coefficients. This high quality prediction achieved by the QR-RLS algorithm results in high quality output images. Furthermore, a diagonal scanning strategy is used to take advantage of the human visual system properties, which exploits the relative insensitivity of the human visual system to diagonal orientations. Both scalar and vector implementations of the proposed method is developed. The scalar implementation processes each color component (red, green, and blue) of the color image separately whereas the vector implementation uses all three color components in the prediction of each color component.

The performance of the proposed method is empirically compared with Floyd-Steinberg's [7] deterministic error diffusion method, and error diffusion with LMS adaptation [8, 13]. The resulting image quality of the proposed error diffusion with QR-RLS adaptation highly outperforms these methods. The contouring effect which is a problem of direct quantization, is almost totally eliminated, and the smooth transitions in slowly varying color regions are truly reproduced even with a very limited number of colors in the palette such as 16. Color impulses which occur in Floyd-Steinberg's error diffusion method, are greatly eliminated. To quantify this superior performance, we compare the error power spectra of the three methods. The new adaptive error diffusion method gives the flattest response with the least energy, implying that it produces the whitest error spectrum which is the least disturbing for the eye among the three algorithms. This gain in visual quality is achieved at the expense of higher computational complexity of the QR-RLS adaptation than deterministic and LMS adaptation methods.

In the second part of the thesis, a new inverse halftoning method, to restore a continuous tone image from the given halftoned image, is introduced. With the assumptions that the halftoning is performed with error diffusion, and the error diffusion filter kernel is known a priori, a new space-domain projection is introduced. frequency-domain, and space-scale domain projections are used alternately with the proposed space-domain projection in the context of the method of POCS.

The performance of the new method is compared with those of the state-of-the-art inverse halftoning methods in the literature based on their PSNR's. Two of these methods employ spatial and frequency-domain projections alternately which are different from ours. Third method employs a single space-scale domain projection in the wavelet domain. The new POCS based inverse halftoning method achieves greater PSNR's than those other three algorithms. The resulting images are good quality images in which the halftoning artifacts are removed. During the removal of the halftoning noise which is inherently concentrated in high-frequency regions, the proposed inverse halftoning method retains the important high-frequency information such as the edges of the image, so the details of the image are not smoothed out. Our method outperforms other state-of-the-art inverse halftoning techniques both in terms of visual quality and PSNR.

The new space-domain projection is extended for the multi-level error diffusion encoding, and the restoration of color images. Inverse halftoning of color images are carried out in two ways. In the first case, the projections are performed separately on red, green, and blue components of the color image. In the second case, the luminance component of the color image is restored as in the grayscale restoration, and the two lowpass filtered chrominance components are added to it. Both methods resulted in reasonable quality restored color output images, although the number of colors in the palette of the initial halftone color image is very low. Our study on inverse halftoning of color images can be considered as a first attempt on this topic in the literature.

A possible future research direction for the halftoning of color images is the faster implementation of the proposed error diffusion with QR-RLS adaptation for use with real-time video on frame buffer displays.

A possible future research direction for the inverse halftoning of color images is to define a vectorized space-domain projection for a color pixel instead of projecting its color components separately for each pixel, and also, to introduce a new space-scale domain projection for color images using the color edge information, that is to retain the useful high-frequency edge information from each subband considering the color edge characteristics.

APPENDIX A

CONVEXITY OF THE SETS USED IN SET THEORETIC INVERSE HALFTONING

Let the set $\boldsymbol{C}_{1,s}$ be the set of images, $\boldsymbol{x}$ producing the pixel $\boldsymbol{y}\,(s)$ after error diffusion, and the set $\boldsymbol{C}_1 = \bigcap \boldsymbol{C}_{1,s}$ is the set of images, $\boldsymbol{x}$, producing the halftoned image $\boldsymbol{y}$. Let $\boldsymbol{a}$ and $\boldsymbol{b}$ be contone images in $\boldsymbol{C}_1$ whose range is in [0,255], and $\boldsymbol{a}$ and $\boldsymbol{b}$ produce a specific error diffused or simply the quantized image $\boldsymbol{c}$. For the binary quantization, the samples $\boldsymbol{c}\,(s)$ take values 0 or 255 by the hard quantizer operation:

$$\begin{aligned} \text{if } \ \boldsymbol{a}\,(s) < 128 \quad &\Longrightarrow \boldsymbol{c}\,(s) \ = \ \mathbf{0} \\ \text{if } \ \boldsymbol{a}\,(s) \geq 128 \quad &\Longrightarrow \boldsymbol{c}\,(s) \ = \ \mathbf{255}\,. \end{aligned}$$

Let α in $0 \leq \alpha \leq 1$ be a real number. If $\boldsymbol{a}$ and $\boldsymbol{b}$ are quantized to $\boldsymbol{c}$ by error diffusion, then the image $(\alpha\boldsymbol{a} + (1-\alpha)\boldsymbol{b})$ is also quantized to $\boldsymbol{c}$. That is

$$\begin{aligned} &\text{if } \ 0 \leq \boldsymbol{a}\,(s),\ \boldsymbol{b}\,(s) < 128 \quad \Longrightarrow 0 \leq (\alpha\boldsymbol{a}\,(s) + (1-\alpha)\boldsymbol{b}\,(s)) < 128, \\ &\text{then } \ \boldsymbol{c}\,(s) = 0, \end{aligned}$$

$$\begin{aligned}&\text{if } 128 \leq \boldsymbol{a}(s),\ \boldsymbol{b}(s) \leq 255 \quad \Longrightarrow 128 \leq (\alpha \boldsymbol{a}(s) + (1-\alpha)\boldsymbol{b}(s)) \leq 255,\\ &\text{then } \ \boldsymbol{c}(s) = 255,\end{aligned}$$

for all the indices s. Therefore, $\boldsymbol{c}$ also belong to $\boldsymbol{C}_1$. The same holds for the multilevel quantizer case. This completes the proof of the convexity of the set $\boldsymbol{C}_1$.

Let the set $\boldsymbol{C}_2$ contain all band-limited contone images as

$$\boldsymbol{C}_2 = \{\boldsymbol{a} \in \mathcal{L}_1^2 \mid (\forall \boldsymbol{\nu} \in \mathcal{R})\mathcal{F}[\boldsymbol{a}](\boldsymbol{\nu}) = \boldsymbol{0} \quad \text{if } |\boldsymbol{\nu}| > \boldsymbol{D}\} \qquad \text{(A.1)}$$

where $\mathcal{F}[\boldsymbol{a}]$ denotes the Fourier transform of $\boldsymbol{a}$. Let $\boldsymbol{a}$, and $\boldsymbol{b}$ be in $\boldsymbol{C}_2$. Then the linear combination of bandlimited signals; $(\alpha\mathcal{F}[\boldsymbol{a}](\boldsymbol{\nu}) + (1-\alpha)\mathcal{F}[\boldsymbol{b}](\boldsymbol{\nu}))$ is still in $\boldsymbol{C}_2$, since $\alpha\mathcal{F}[\boldsymbol{a}](\boldsymbol{\nu}) = \boldsymbol{0}$ for $|\boldsymbol{\nu}| > \boldsymbol{D}$, and $(1-\alpha)\mathcal{F}[\boldsymbol{b}](\boldsymbol{\nu}) = \boldsymbol{0}$ for $|\boldsymbol{\nu}| > \boldsymbol{D}$. That is, the convexity imposes a weighted averaging constraint which only affects the amplitude. This completes the proof of the convexity of the set $\boldsymbol{C}_2$.

Let the set $\boldsymbol{C}_3$ contain all the images having the same WT local extrema in the space-scale domain. The convexity of the set $\boldsymbol{C}_3$ can be proved similarly as in convexity of the set $\boldsymbol{C}_2$ consisting of all the bandlimited signals. Let the Fourier transforms of the signals $\boldsymbol{a}$ and $\boldsymbol{b}$ be $\mathcal{F}[\boldsymbol{a}]$ and $\mathcal{F}[\boldsymbol{b}]$ respectively which have the same local extrema points, i.e they both belong to the same set $\boldsymbol{C}_3$. The signal $\alpha\mathcal{F}[\boldsymbol{a}](\boldsymbol{\nu})$ has the same local extrema as the signal $\mathcal{F}[\boldsymbol{a}](\boldsymbol{\nu})$, and similarly, the signal $(1-\alpha)\mathcal{F}[\boldsymbol{b}](\boldsymbol{\nu})$ has the same local extrema as the signal $\mathcal{F}[\boldsymbol{b}](\boldsymbol{\nu})$, since only scaling is performed on the amplitude of the signal. Therefore, the resulting signal $\mathcal{F}[\mathbf{c}](\boldsymbol{\nu}) = \alpha\mathcal{F}[\boldsymbol{a}](\boldsymbol{\nu}) + (1-\alpha)\mathcal{F}[\boldsymbol{b}](\boldsymbol{\nu})$ produce the same local extrema, and belong to the set $\boldsymbol{C}_3$. This completes the proof of the convexity of the set $\boldsymbol{C}_3$.

Bibliography

[1] G. Sharma and H.J. Trussell. Digital color imaging. *IEEE Trans. Image Process.*, 6(7):901–932, 1997.

[2] J.C. Stoffel and J.F. Moreland. A survey of electronic techniques for pictorial image reproduction. *IEEE Trans. Communications*, COM-29(12):1898–1925, 1981.

[3] L.G. Roberts. Picture coding using pseudo-random noise. *IRE Trans. Inform. Theory*, 8(2):145–154, 1962.

[4] J.A.C. Yule. *Principles of Color Reproduction.* John Wiley & Sons, 1967.

[5] R. Ulichney. *Digital Halftoning.* The MIT Press, MIT, MA., 1987.

[6] J. Sullivan, L. Ray, and R. Miller. Design of minimum visual modulation halftone patterns. *IEEE Trans. Syst., Man. Cybernetics*, 21(1):33–38, 1991.

[7] R.W. Floyd and L. Steinberg. An adaptive algorithm for spatial grayscale. volume 17, pages 75–77, 1976.

[8] L. Akarun, Y. Yardımcı, and A.E. Çetin. Adaptive methods for dithering color images. *IEEE Trans. Image Process.*, 6(7):950–955, 1997.

[9] I.H. Witten and M. Neal. Using peano curves for bilevel display of contionuous tone images. *IEEE Comp. Graph. & Appl.*, (5):47–52, 1982.

[10] T. Asano. Digital halftoning algorithm based on random space-filling curve. In *Proc. IEEE Int. Conf. on Image Processing*, pages 545–548, 1996.

[11] T.N. Pappas. Model-based halftoning of color images. *IEEE Trans. Image Process.*, 6(7):1014–1024, 1997.

[12] J. Sullivan, R. Miller, and G. Pios. Image halftoning using a visual model in error diffusion. *J. Opt. Soc. Am. A*, 10(8):1714–1724, 1993.

[13] P.W. Wong. Adaptive error diffusion and its application in multiresolution rendering. *IEEE Trans. Image Process.*, 5(7):1184–1196, 1996.

[14] B. Widrow and S.D. Stearns. *Adaptive Signal Processing.* Prentice Hall, New Jersey, 1985.

[15] D. Anastassiou. Error diffusion coding for A/D conversion. *IEEE Trans. Circuits and Syst.*, 36(9):1175–1186, 1989.

[16] B.L. Shoop and E.K. Ressler. Optimal error diffusion for digital halftoning using an optical neural network. In *Proc. IEEE Int. Conf. on Image Processing*, pages 1036–1040, 1994.

[17] A. Makur and A. Kumar. Iterative error diffusion halftoning using a zero phase error filter . In *Proc. IEEE Int. Conf. on Image Processing*, pages 795–798, 1997.

[18] B.W. Kolpatzik and C.A. Bouman. Optimized error diffusion for high-quality image display. *J. Electronic Imag.*, 1(3):277–292, 1992.

[19] L. Akarun, D. Özdemir, and E. Apaydın. Fuzzy error diffusion of color images. In *Proc. IEEE Int. Conf. on Image Processing*, pages 46–49, 1997.

[20] R.Eschbach and K.T. Knox. Error-diffusion algorithm with edge enhancement. *J. Opt. Soc. Am. A*, 8(12):1844–1850, 1991.

[21] T.N. Pappas. Least-squares model-based halftoning. *Proc. SPIE,Human Vision, Visual Processing, and Digital Display III*, 1666:165–176, 1992.

[22] C.F. Hall and E.L. Hall. A nonlinear model for the spatial characteristics of the human visual system. *IEEE Trans. Syst., Man. Cybernetics*, 7(3):162–170, 1977.

[23] J.L. Mannos and D.J. Sakrison. The effects of a visual fidelity criterion on the encoding of images. *IEEE Trans. Information Theory*, 20(4):525–536, 1974.

[24] A. Zakhor, S. Lin, and F. Eskafi. A new class of B/W halftoning algorithms. *IEEE Trans. Image Process.*, 2(4):499–508, 1993.

[25] J.B. Mulligan and A.J. Ahumada. Principled halftoning based on human vision models. *Proc. SPIE,Human Vision, Visual Processing, and Digital Display III*, 1666(3):109–121, 1992.

[26] N. Kobayashi and H. Saito. Halftoning technique using genetic algorithm. In *Proc. IEEE Int. Conf. Acoust. Speech Signal Process.*, pages 108–104, 1994.

[27] T. Mitsa and K.J. Parker. Digital halftoning using a blue-noise mask . In *Proc. IEEE Int. Conf. Acoust. Speech Signal Process.*, pages 2809–2802, 1991.

[28] M.T. Orchard and C.A. Bouman. Color quantization of images. *IEEE Trans. Signal Process.*, 39(12):2677–2690, 1991.

[29] L. Akarun, O. Yalçın, and D. Özdemir. Joint quantization and dithering of color images. In *Proc. IEEE Int. Conf. on Image Processing*, pages 557–560, 1996.

[30] P. Scheunders and S. De Backer. Joint quantization and error diffusion of color images using competitive learning. In *Proc. IEEE Int. Conf. on Image Processing*, pages 811–814, 1997.

[31] E. Peli. Multiresolution, error-convergence halftone algorithm. *J. Opt. Soc. Am. A*, 8(4):625–636, 1991.

[32] I. Katsavounidis and C.C.J. Kuo. A multiscale error diffusion technique for digital halftoning. *IEEE Trans. Image Process.*, 6(3):483–490, 1997.

[33] P.W. Wong. Inverse halftoning and kernel estimation for error diffusion. *IEEE Trans. Image Process.*, 4(4):486–498, 1995.

[34] R.L. Stevenson. Inverse halftoning via map estimation. *IEEE Trans. Image Process.*, 6(4):574–583, 1997.

[35] M. Analoui and J. Allebach. New results on reconstruction of continous-tone from halftone. In *Proc. IEEE Int. Conf. Acoust. Speech Signal Process.*, pages 313–316, 1992.

[36] S. Hein and A. Zakhor. Halftone to continous-tone conversion of error-diffusion coded images. *IEEE Trans. Image Process.*, 4(2):208–215, 1995.

[37] Z. Xiong, M.T. Orchard, and K. Ramchandran. Inverse halftoning using wavelets. In *Proc. IEEE Int. Conf. on Image Processing*, pages 569–572, 1996.

[38] J. Luo, R. de Queiroz, and Z. Fan. A robust technique for image descreening based on the wavelet transform. *IEEE Trans. Signal Process.*, 46(4):1179–1184, 1998.

[39] M.Y. Ting and E.A. Riskin. Error-diffused image compression using a binary-to-gray-scale decoder and predictive pruned tree-structured vector quantization. *IEEE Trans. Image Process.*, 3(6):854–858, 1994.

[40] J.R. Jarvis, C.N. Judice, and W.H. Ninke. A survey of techniques for the display of continous tone pictures on bilevel displays. *Comput. Graph., Image Proc.*, 5:13–40, 1976.

[41] J.S. Lim. *Two-dimensional Signal and Image Processing.* Prentice Hall, New Jersey, 1990.

[42] J.M. Cioffi and T. Kailath. Fast, recursive-least squares tranversal filters for adaptive filtering. *IEEE Trans. Acoust., Speech, and Signal Process.*, 32(4):304–337, 1984.

[43] B. Yang and J.F. Bohme. Rotation-based RLS algorithms: unified derivations, numerical properties, and parallel implementations. *IEEE Trans. Signal Process.*, 40(5):1151–1167, 1992.

[44] P. Heckbert. Color image quantization for frame buffer display. *Comput. Graph.*, 16(7):297–307, 1982.

[45] M.H. Hayes. *Statistical Digital Signal Processing and Modeling.* John Wiley & Sons, 1996.

[46] P.L. Combettes. The foundations of set theoretic estimation. *Proc. IEEE*, 81(2):182–208, 1993.

[47] A.E. Çetin and R. Ansari. Signal recovery from wavelet transform maxima. *IEEE Trans. Signal Process.*, 42(1):194–196, 1994.

[48] S. Mallat and S. Zhong. Characterization of signals from multiscale edges. *IEEE Trans. Pattern Analysis, and Machine Intelligence*, 14(7):710–732, 1992.

[49] A.H. Tewfik and H. Zou. Completeness of arbitrarily sampled discrete time wavelet transforms. *IEEE Trans. Signal Process.*, 43(11):2570–2581, 1995.

[50] Y. Xu, J.B. Weaver, D.M. Healy Jr., and J. Lu. Wavelet transform domain filters: a spatially selective noise filtration technique. *IEEE Trans. Image Process.*, 3(6):747–758, 1994.